School of Chemical and Petroleum Engineering

The development of the novel electrode materials for electrochemical energy storage applications

YU LIU

This thesis is presented for the Degree of
Doctor of Philosophy
of
Curtin University

May 2018

Declaration

To the best of my knowledge and belief this thesis contains no material previously published by any other person except where due acknowledgment has been made.

This thesis contains no material which has been accepted for the award of any other degree or diploma in any university.

Signature: .....

Date: 08/05/2018

Acknowledgements

The three and half years I have spent at Curtin University have given me source of the most precious experiences in my life. I believe that I must be blessed to be a member of such a great group and make so many friends here. I would like to acknowledge a number of people who were accompanying me through the whole journey here.

Firstly, I would like to express my sincere gratitude to my supervisor Professor Zongping Shao for the continuous support of my PhD study and related research, for his patience, motivation, and immense knowledge. His guidance helped me in all the time of research and writing of this thesis. I could not have imagined having a better advisor and mentor for my Ph.D study.

Furthermore, I am especially grateful to my co-supervisor Professor Moses Tade, for his guidance, understanding and insight over the years. I learned a lot from him, not only in science, but also in life. I would like to thank Associate Professor Martin Saunders and Dr Aaron Dodd from University of Western Australia and Elaine Miller for their help on transmission electron microscopy and scanning electron microscopy. I would also like to thank Dr. Jean-Pierre Veder for his help on XPS and NEXFS analysis. Furthermore, a special note should also be made to Dr Matthew Rowles and Ms Veronica Avery for their generous support on XRD.

In particular, I would like to thank the members in our group, Dr Wei Wang, for his endless encouragement, collaboration, and friendship. Thanks to Dr Chao Su, Mr Xiaomin Xu, Mr Yijun Zhong Mr Paulo Sérgio Barros Julião, and other members for providing me excellent research environment and helpful comments. I am also thankful to Chi Zhang, Ping Liang, Jian Kang, Xiaochen Guo, Shambhu Singh Rathore, Huayang Zhang, Andrew Chan, Anja Werner, Roshanak Doroushi, Yu Long, Guanliang Zhou and Melina Miralles.

Last but not least, I am grateful to my parents and my sister, who have provided me through moral and emotional support in my life. My sincere thanks also go to my wife, who supports me spiritually throughout writing this thesis and my life in general. Without you, it would have been very difficult for me to get to this memorable moment of being a PhD. I am also grateful to my other family members and friends who have supported me along the way.

Abstract

With rapid growth of the world's population and continuous expansion in global economy, a fast increase in the application of energy-based appliances has been envisioned, which ultimately will lead to a quick increase in the energy consumption rate. Supercapacitors are one of the most important electrochemical energy storage devices which possess some highly attractive properties such as ultrahigh power density (up to ≈10 000 W kg^{-1}), short charging times (in the order of tens of seconds), and long lifetime over repeated charge–discharge cycles (>100 000 cycles). Supercapacitors have many potential applications, such as frequency regulation in smart grids and power sources for hybrid electric vehicles. Owing to the limited device space for these applications, the development of electrode materials with high volumetric energy density is imperative. Perovskite oxides generally have larger tap density, due to the dense and non-porous material structures. In addition, perovskite oxides also possess higher oxygen vacancy concentration and excellent oxygen ion mobility. Higher volumetric specific capacity can be obtained through oxygen-anion intercalation mechanism by selecting appropriate perovskite oxides. Metal-air batteries are highly attractive electrochemical energy storage devices that may fill the gap between the renewable energy (e.g., wind and solar power) and the state-of-the-art energy infrastructure, and possibly also be considered as the main power source for electrified transportation. Such electrochemical devices normally involve an oxygen reduction reaction (ORR) over their positive electrode; unfortunately, the sluggish ORR kinetics at room temperature significantly limit their efficiency and performance, and thus have become a major obstacle towards their practical applications.

In this thesis, a series of perovskite oxides and spinal oxides were chosen for the study in supercapacitors. Hierarchically porous bio-carbon microspheres were used as an exceedingly active and stable ORR electrocatalysts. To investigate the performance and the energy storage mechanism of the synthesized materials, X-ray diffraction (XRD), X-ray photoelectron spectroscopy (XPS), scanning electron microscopy (SEM), transmission electron microscopy (TEM), cyclic voltammetry (CV) and electrochemical impedance spectroscopy (EIS) and other characterization methods were used. The specific contents of this thesis were introduced as follows:

Firstly, to get some useful guidelines for future materials development, we comparatively studied $SrCoO_{3-\delta}$ (SC), $Ba_{0.5}Sr_{0.5}Co_{0.8}Fe_{0.2}O_{3-\delta}$ (BSCF), and Co_3O_4 as electrodes in supercapacitors with aqueous alkaline electrolyte. The effect of interaction between the electrode materials with the alkaline solution was focused on the structure and specific surface area of the electrode material, and ultimately the electrochemical performance was emphasized. Both BSCF and SC were found to experience cation leaching in alkaline solution, resulting in an increase in the specific surface area of the material, but overleaching caused the damage of perovskite structure of BSCF. Secondly, reduced $PrBaMn_2O_{6-\delta}$ possessing a layered double perovskite structure, exhibited ultrahigh capacitance and could function as an excellent oxygen anion-intercalation-type electrode material for supercapacitors. Formation of the layered double perovskite structure, as facilitated by hydrogen treatment, is shown to significantly enhance the capacitance, with the resulting r-PBM material demonstrating a very high gravimetric capacitance of 1034.8 F g^{-1} and an excellent volumetric capacitance of approximately 2535.3 F cm^{-3} at a current density of 1 A g^{-1}. Thirdly, spinel-type $NiCo_2O_4$ and $NiCo_2S_4$ polyhedron architectures with sizes of 500–600 nm and rich mesopores with diameters of 1–2 nm were prepared facilely by the molecular design of Ni and Co into polyhedron-shaped zeolitic imidazolate frameworks as solid precursors. Both as-prepared NCO and NCS nanostructures exhibited excellent pseudocapacitance and stability as electrodes in supercapacitors. In particular, the exchange of O^{2-} in the lattice of NCO with S^{2-} obviously improves the electrochemical performance. Finally, renewable natural date pulp was used as the carbon precursor, and a facile hydrothermal carbonization method with *in situ* formed cobalt as a template was employed for the synthesis of such spherical bio-carbons. Remarkably, the catalysts yielded competitive catalytic activity (a small Tafel slope of 53 mV dec^{-1}) and superb durability and methanol tolerance compared to the benchmark Pt/C catalyst in an alkaline electrolyte. Even under harsh acidic conditions, the catalysts still delivered a satisfactory catalytic performance and excellent stability, indicating their extensive applicability.

List of Publications

1. **Yu Liu**, Jim Dinh, Moses O. Tade, Zongping shao, Design of Perovskite Oxides as Anion-Intercalation-Type Electrodes for Supercapacitors: Cation Leaching Effect, *ACS Applied Materials & Interfaces*, 8 (2016) 23774-23783.

2. **Yu Liu**, Zhenbin Wang, Yijun Zhong, Wei Zhou, Moses O.Tade, Zongping Shao, Molecular design of mesoporous $NiCo_2O_4$ and $NiCo_2S_4$ with submicron-polyhedron architectures for efficient pseudocapacitive energy storage, *Advanced Functional Materials*, 1701229 (2017) 1-10.

3. **Yu Liu**, Zhenbin Wang, Jean-Pierre Veder, Zongping Shao, Highly defective layered double perovskite oxide for efficient energy storage through reversible pseudocapacitive oxygen anion intercalation, *Advanced Energy Materials*, (2018) 1702604.

4. Liang Zhu, **Yu Liu**, Chao Su, Wei Zhou, Meilin Liu, Zongping Shao, Perovskite $SrCo_{0.9}Nb_{0.1}O_{3-\delta}$ as an Anion-intercalated electrode material for supercapacitors with ultrahigh volumetric energy density, *Angewandte Chemie International Edition*, 55 (2016) 9576-9579.

5. Wei Wang, **Yu Liu**, Jifa Qu, Yubo Chen, Zongping Shao, Nitrogen-doped TiO_2 microspheres with hierarchical micro/nanostructures and rich dual-phase junctions for enhanced photocatalytic activity, *RSC Advances*, 6 (2016) 40923-40931.
6. Wei Wang, **Yu Liu**, Jifa Qu, Yubo Chen, Moses O. Tade, Zongping Shao, Synthesis of hierarchical TiO_2–C_3N_4 hybrid microspheres with enhanced photocatalytic and photovoltaic activities by maximizing the synergistic effect, *ChemPhotoChem*, 1 (2017) 35-45.
7. Chao Su, Xiaomin Xu, Yubo Chen, **Yu Liu**, Moses O. Tade, Zongping Shao, A top-down strategy for the synthesis of mesoporous $Ba_{0.5}Sr_{0.5}Co_{0.8}Fe_{0.2}O_{3-\delta}$ as a cathode precursor for buffer layer-free deposition on stabilized zirconia electrolyte with a superior electrochemical performance, *Journal of Power Sources*, 274 (2015) 1024-1033.
8. Xuyin Jiang, Shiyong Chu, Yubo Chen, Yijun Zhong, **Yu Liu**, Zongping Shao, $LiNi_{0.29}Co_{0.33}Mn_{0.38}O_2$ polyhedrons with reduced cation mixing as a high-performance cathode material for Li-ion batteries synthesized via a combined co-

precipitation and molten salt heating technique, *Journal of Alloys and Compounds*, 691 (2017) 206-214.

9. Chao Su †, **Yu Liu** †, († Equal Contribution) Zongping Shao, Direct conversion of natural dates-pulp to hierarchically porous bio-carbon microspheres as efficient and stable metal-free oxygen-reduction electrocatalysts, *under review*.
10. **Yu Liu**, Chen Wang, Shaobin Wang, Zongping Shao, Core shell Co@carbon spheres with different degree of oxidation in the application of lithium ion batteries and phenol degradation, *in preparation*.
11. **Yu Liu**, Zongping Shao, C_3N_4@net $NiCo_2O_4$ as the anode in the lithium ion batteries, *in preparation*.
12. **Yu Liu**, Zongping Shao, Co_3O_4 particle @ biological active graphite derived from dates pulp: A Highly Efficient and stable anode material For Li-batteries applications, *in preparation*.

Awards

Best Paper Award, WACSA, Perth, Australia, 2017

Contents

Chapter 1 Introduction

1.1 Background

With the rapid development of science and technology in the past century, our modern life of various fields have undergone unbelievable changes. Although these changes exert a positive and significant effect on our life, they have led to a lot of consumption of fossil energy immediately or indirectly. These fossil energies, which are of essential resources of human life, will be used up in the next centuries. Moreover, the slather use of energy, especially the traditional fossil energy resources, put an enormous amount of carbon dioxide into the atmosphere. Such CO_2 emission can bring and accelerate the appearance of many environmental problems. Thus, Energy crisis and environmental pollution are considered to be the primary challenges that hinder the sustainable development of economy of human society at present. Due to the serious problems caused by traditional energy, much attention has been focused on developing clean and renewable energy.

Energy storage is an important technology for the realization of renewable energy storage and transportation. For new and clean energy, the intermittency of solar, wind and tidal energy is their main disadvantage. And these energy have been conditioned by geography and the natural environment. Therefore, it needs to be matched with the appropriate energy storage system to achieve the goal of enhancing the continuous electrical supply. While a nuclear reactor can provide a constant source of energy, it is also accompanied by relevant radioactive waste disposal problems. Meanwhile, geothermal energy is geographically limited. Thus, these energy sources require the transfer of energy storage media. For traditional energy, due to the Carnot cycle, the energy conversion efficiency of traditional diesel locomotives is affected, the energy conversion efficiency of fossil fuel resources is relatively lower. However, electric engine with high energy conversion efficiency and "zero" emission of pollutants and other salient advantages, has become a worldwide technology competing for development. Electrochemical storage is considered the most promising way to provide a stable and reliable energy storage system. Therefore, the development of power cells and battery materials is a key factor in achieving efficient energy storage.

A capacitor is defined as a passive electrical component with two terminals in which electrical energy can be stored in an electric field.[1-5] Capacitance can be applied to

describe the effect of a capacitor. Because capacitance are present between any two electrical conductors of a circuit in a very close contact, the particular design of a capacitor lies in the supply and improvement of this effect so that it can be applied in a range of practical fields.[6-8] Therefore, size, shape, location of conductors in close proximity, as well as the intervening dielectric material should be considered carefully.[9] Practical capacitors differ greatly in terms of the fabrication and physical form. However, there are some commonly-used capacitor categories. Generally speaking, a majority of capacitors have at least two electrical conductors, which are characterized by metallic plates or surfaces isolated by a dielectric medium. The types of a conductor can be diverse, such as a foil, thin film, sintered bead of metal, or an electrolyte. The dielectric with no conductivity functions as a tool to enhance the charge capacity of the capacitor. Glass, paper, ceramic, mica, plastic film as well as oxide layers are widely-used materials as dielectrics. In various pervasive electrical devices, capacitors are frequently applied as parts of electrical circuits. In comparison (**Figure 1.1**), lithium ion batteries (LIBs) have relatively large energy density, but it cannot provide a lot of energy in a short time due to its longer charging time.[10, 11] Thus, this shortcoming makes it impossible to meet the requirements of some high-energy pulse areas. In addition, LIBs generally only maintain hundreds of charge-discharge cycles, and most of the batteries capacitance will drop sharply because of frequent reaction with high-power pulse current.[12] Fuel cells can also provide high energy densities, but low power density, poor large pulse current charge and discharge performance, and expensive cost restrict the practical application of fuel cells.[13-15] Therefore, the development of a device which can have a high power density as traditional capacitor and high energy density as battery is a basic requirement for future energy applications.

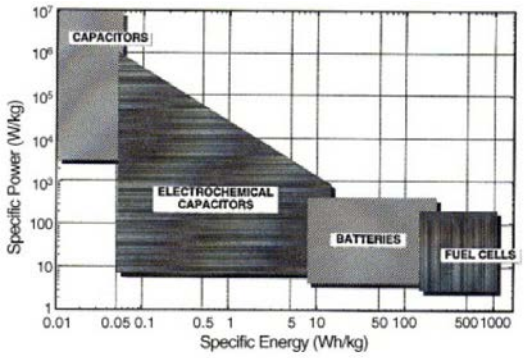

Figure 1.1 Ragone plot of various energy storage devices.[16] (Reproduced with permission. 2006, ELSEVIER)

Supercapacitor is commonly known as an electrochemical energy storage device as well as a capacitor with high capacity, which has rather higher capacitance values but relatively lower voltage limits than other capacitors, thus, the gap present between rechargeable batteries and electrolytic capacitors can be narrowed.[17-19] In terms of storage, a range from 10 to 100 times more energy per unit volume or mass can be stored compared with electrolytic capacitors; in terms of speed, they can obtain and transfer charge more quickly than batteries; in terms of recycle, more charge and discharge cycles can be tolerated in comparison with rechargeable batteries. Instead of long-term compact energy storage, fast charge and discharge cycles are required in the applications of supercapacitors.[20] With regard to cars, buses, trains, cranes and elevators, supercapacitors play roles in regenerative braking, short-term energy storage or burst-mode power delivery. Two main forms of capacitive behaviours explain how supercapacitors store energy, that is, the electrical double layer capacitance (EDLC) ascribed to the pure electrostatic charge accumulated at the electrode interface, as well as the pseudo-capacitance traced to reversible and rapid surface redox reactions occurring at characteristic potentials.[21] Although they coexist in supercapacitors, these two mechanisms are better and more convenient to be discussed separately.

The lithium-air batteries, abbreviated to LABs, are proved to be a type of metal-air electrochemical cell that involves battery chemistry.[22-24] In LABs, a current flow is induced by lithium oxidation at the anode as well as oxygen reduction at the cathode. In comparison with LIBs with closed systems, LABs have won great applauses in recent years due to their distinctive half-open system. In such a system, oxygen derived from ambient air is utilized and thus decreases the mass and volume of the air electrode required and enhances the energy density. Metal-air batteries have different working

mechanisms from LIBs, in which metal dissolution and deposition occurs on the negative (or metal) electrode, while oxygen reduction reaction (ORR) and oxygen evolution reaction (OER) takes place on the positive (or air) electrode.[25, 26] Among diverse energy storage systems, LABs, due to their exceptional theoretical energy densities, are one of emerging technologies with great potential.

1.2 Research objectives

The primary aim of this thesis is to introduce new electrode materials of supercapacitors and lithium-based batteries. The oxygen intercalation mechanism of perovskite oxide electrode in supercapacitors, the surface Faradic redox mechanism of spinal oxide electrode in supercapacitors and the oxygen reduction reaction of carbon and oxide hybrid lithium air battery electrode are also investigated. The specific goals of this study are listed as follows.

a. Summarizing the current research status of surface faradic redox type supercapacitor, oxygen ion intercalation type supercapacitor and oxygen reduction reaction of the electrodes in lithium-air batteries.
b. Investigating the interaction between the electrode materials and the alkaline solution and its effect on the electrode performance, including capacity and cycling stability. Selective leaching of certain compositional element(s) from the perovskite oxides into the alkaline aqueous solution under the supercapacitor's operation condition was also demonstrated.
c. Exploring the structural properties of a double perovskite oxide $PrBaMn_2O_{6-\delta}$ with a reducing treatment under hydrogen atmosphere and using it as the electrode of oxygen intercalation type supercapacitor.
d. Synthesizing mesoporous polyhedron-structured $NiCo_2O_4$ and $NiCo_2S_4$ nanoparticles by molecular design of Ni and Co bimetallic ZIFs as solid precursors. Investigating the electrochemical properties of these two samples as electrodes of supercapacitor.
e. Fabricating a hierarchically porous heteroatom dopant free carbon microspheres and investigating its application as an electrocatalyst for oxygen reduction reaction under both alkaline and acidic conditions.

1.3 Thesis organization

Seven chapters are included in this thesis, including introduction and thesis outline, recent literature review, results and discussions as well as conclusions and future perspectives.

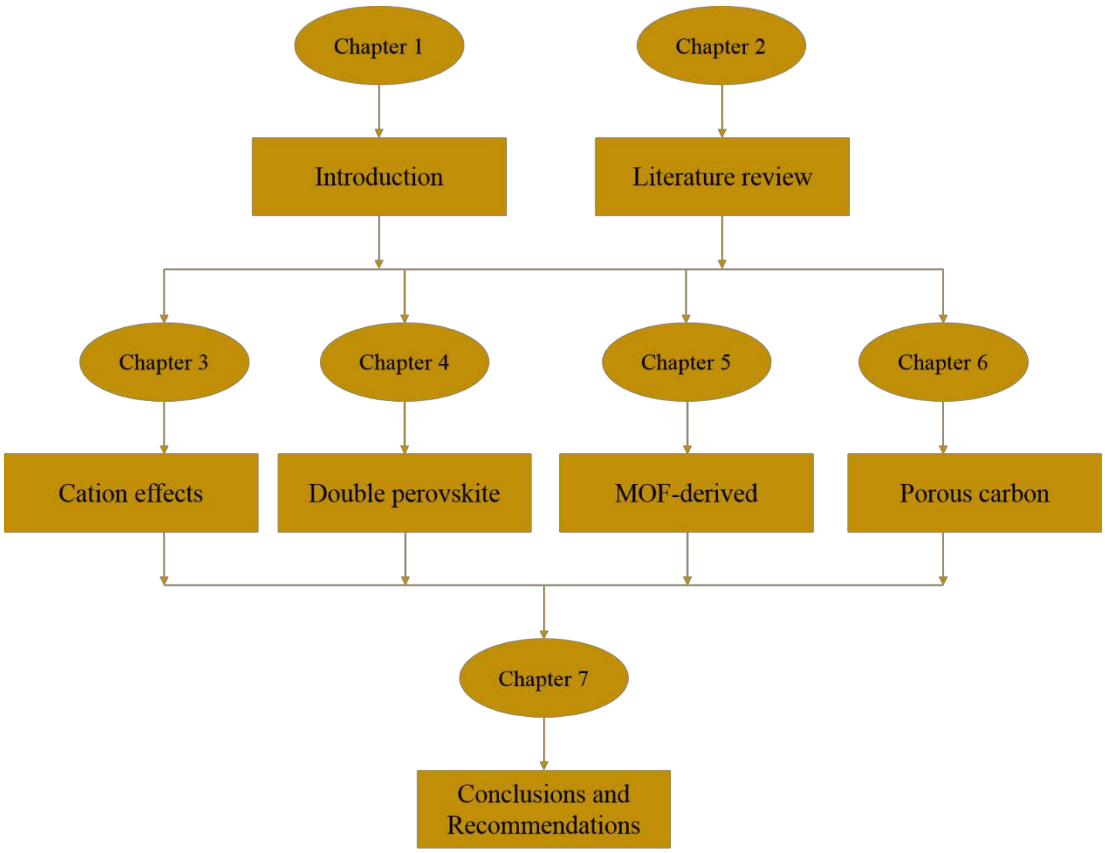

Figure 1.2 Schematic of thesis structure and organization

Chapter 1: Introduction

This chapter briefly introduces the background of supercapacitors and electrode reactions of lithium-air batteries, along with the reasons for doing this research. Research objectives as well as structural organization are also included in this chapter.

Chapter 2: Literature Review

The comprehensive summary of latest development of supercapacitors is outlined on the basis of superiorities and challenges faced by new energy storage technologies. The principles, merits and demerits, together with critical problems brought by various supercapacitors are discussed in detail. In addition, the oxygen reduction reaction of electrode in lithium-air batteries is also reviewed.

Chapter 3 Design of Perovskite Oxides as Anion-Intercalation-Type Electrodes for Supercapacitors: Cation Leaching Effect

In this chapter, $SrCoO_{3-\delta}$ (SC), $Ba_{0.5}Sr_{0.5}Co_{0.8}Fe_{0.2}O_{3-\delta}$ (BSCF), as well as Co_3O_4 functioning as electrodes in supercapacitors with aqueous alkaline electrolyte were comparatively investigated in order to acquire insightful ideas for future development. Structure, along with specific surface area of electrode materials, determined interaction effects present between electrode materials and alkaline solutions. Meanwhile, we also underlined the electrochemical performance.

Chapter 4 Highly defective layered double perovskite oxide for efficient energy storage via reversible pseudocapacitive oxygen-anion intercalation

It is reported that reduced $PrBaMn_2O_{6-\delta}$ (r-PBM), possessing a layered double perovskite structure, exhibits ultrahigh capacitance and functions as an excellent oxygen anion-intercalation-type electrode material for supercapacitors. Formation of the layered double perovskite structure, as facilitated by hydrogen treatment, is shown to significantly enhance the capacitance, with the resulting r-PBM material demonstrating a very high gravimetric capacitance

Chapter 5 Molecular Design of Mesoporous $NiCo_2O_4$ and $NiCo_2S_4$ with Sub-Micrometer-Polyhedron Architectures for Efficient Pseudocapacitive Energy Storage

Spinel-type $NiCo_2O_4$ (NCO) and $NiCo_2S_4$ (NCS) polyhedron architectures with sizes of 500-600 nm and rich mesopores with diameters of 1-2 nm are prepared facilely by the molecular design of Ni and Co into polyhedron-shaped zeolitic imidazolate frameworks (ZIFs) as solid precursors. Both as-prepared NCO and NCS nanostructures exhibit excellent pseudocapacitance and stability as electrodes in supercapacitors.

Chapter 6 Direct Conversion of Natural Date Pulp to Hierarchically Porous Bio-Carbon Microspheres as Efficient and Stable Oxygen-Reduction Electrocatalysts

In this chapter, renewable natural date pulp was used as the carbon precursor to successfully prepare the hierarchically porous bio-carbon microspheres (PBCS) via a facile hydrothermal carbonization method. The PBCS delivers competitive ORR catalytic activity in both alkaline conditions and harsh acidic conditions, implying an extensive applicability.

Chapter 7 Conclusions and perspectives

Meaningful outcomes in each chapter are summarized in this chapter and constructive suggestions are also provided.

1.4 Reference

[1] W. Gu, G. Yushin, WIREs Energy Environ., 3 (2014) 424-473.

[2] J. Minase, T.F. Lu, B. Cazzolato, S. Grainger, Precis. Eng., 34 (2010) 692-700.

[3] K. Naoi, Fuel Cells, 10 (2010) 825-833.

[4] J. Yoo, J. Kim, Y.S. Kim, J. Power Sources, 284 (2015) 466-480.

[5] Y. Zhang, H. Feng, X. Wu, L. Wang, A. Zhang, T. Xia, H. Dong, X. Li, L. Zhang, Int. J. Hydrogen Energy, 34 (2009) 4889-4899.

[6] A. Nishino, J. Power Sources, 60 (1996) 137-147.

[7] A.G. Pandolfo, A.F. Hollenkamp, J. Power Sources, 157 (2006) 11-27.

[8] G.A. Snook, P. Kao, A.S. Best, J. Power Sources, 196 (2011) 1-12.

[9] N. Devillers, S. Jemei, M.-C. Péra, D. Bienaimé, F. Gustin, J. Power Sources, 246 (2014) 596-608.

[10] C. Liu, Z. Yu, D. Neff, A. Zhamu, B.Z. Jang, Nano Lett., 10 (2010) 4863-4868.

[11] P. Sharma, T.S. Bhatti, Energy Convers. Manage., 51 (2010) 2901-2912.

[12] J.M. Tarascon, M. Armand, Nature, 414 (2001) 359.

[13] V. Mehta, J.S. Cooper, J. Power Sources, 114 (2003) 32-53.

[14] S.J. Peighambardoust, S. Rowshanzamir, M. Amjadi, Int. J. Hydrogen Energy, 35 (2010) 9349-9384.

[15] B.C.H. Steele, A. Heinzel, Nature, 414 (2001) 345.

[16] A.G. Pandolfo, A.F. Hollenkamp, Journal of Power Sources, 157 (2006) 11-27.

[17] A. Kuperman, I. Aharon, Renewable Sustainable Energy Rev., 15 (2011) 981-992.

[18] D.P. Dubal, O. Ayyad, V. Ruiz, P. Gomez-Romero, Chem. Soc. Rev., 44 (2015) 1777-1790.

[19] M. Winter, R.J. Brodd, Chem. Rev., 104 (2004) 4245-4270.

[20] G. Wang, L. Zhang, J. Zhang, Chem. Soc. Rev., 41 (2012) 797-828.

[21] C. Largeot, C. Portet, J. Chmiola, P.-L. Taberna, Y. Gogotsi, P. Simon, J. Am. Chem. Soc., 130 (2008) 2730-2731.

[22] J. Xiao, D. Mei, X. Li, W. Xu, D. Wang, G.L. Graff, W.D. Bennett, Z. Nie, L.V. Saraf, I.A. Aksay, J. Liu, J.-G. Zhang, Nano Lett., 11 (2011) 5071-5078.

[23] H.-G. Jung, J. Hassoun, J.-B. Park, Y.-K. Sun, B. Scrosati, Nat. Chem., 4 (2012) 579.

[24] G. Girishkumar, B. McCloskey, A.C. Luntz, S. Swanson, W. Wilcke, J. Phys. Chem. Lett., 1 (2010) 2193-2203.

[25] C.C.L. McCrory, S. Jung, J.C. Peters, T.F. Jaramillo, J. Am. Chem. Soc., 135 (2013) 16977-16987.

[26] Y. Liang, Y. Li, H. Wang, J. Zhou, J. Wang, T. Regier, H. Dai, Nat. Mater., 10 (2011) 780.

Chapter 2. Literature review

2.1 Introduction

Nowadays, two major frontiers persist among the energy challenges faced by the present world, namely, producing electricity from sustainable energy resources instead of fuels, and altering transportation on the ground ignited by internal combustion engines (ICEs) to electric vehicles (EV) propelled by electricity. Seeking sustainable energy sources tends to be one of the primary directions to promote the energy development. If sustainable energy is used to produce electricity, then appropriate technologies to store energy, such as batteries or supercapacitors, are thus in great demand. In recent years, researchers have made great progress in the rapid development of technologies to successfully produce energy from renewable sources, such as wind turbines, solar cell or geothermal power.[1-5] However, the development of storage devices still cannot keep up with the current development of sustainable energy. Hence, one of the severe challenges faced by modern electrochemistry is the development of energy extended life cycle storage devices with long-term stability to store sustainable energy, while satisfying environmental constraints. Due to its non-renewable characteristic, a rapid decrease in the use of fossil fuel energy resources as energy providers (especially in the transportation sector) is a necessity in modern society. Therefore, a consensus that an increasing emphasis should be given to EVs is reached among political leaders, economic pioneers, scientists and a large number of car manufacturers. Fuel cells (FCs) are likely to provide the highest energy density.[6-8] Nevertheless, the FC technology does not seem to be mature enough to be practically implemented in EVs owing to operation issues attached to electrocatalysis in direct FCs, along with a few serious problems in hydrogen storage for H_2/O_2 FCs.[9, 10]

Our portable devices, such as smart phones, laptops, computers or mini cameras, can keep working throughout the whole daytime supported by high performance batteries from the fact that they have high energy density. However, it still takes a considerable amount of time to charge a battery from zero to 100%. In 1990, Sony Company created lithium-ion batteries (LIBs) and much of the pioneering work was carried by Whittingham, Scrosati and Armand.[11] Plenty of publications have detailedly reported their categorization as well as characterization.[12-16] In the early stages, researchers attempted to apply metal Li as anode to develop and study rechargeable Li batteries.

However, the early 1990s witnessed the appearance of some nearly commercially-used products of secondary Li (metal) batteries.[17] In the initial research and development of Li-ion batteries, it was obvious to conclude that transition metal oxides as well as sulphides can be utilized as superb reversible materials for the cathode of rechargeable Li batteries.[18-24] At a second stage, the Li-ion battery technology evolution was mainly attributed to that of the graphite, rather than Li metal itself, which was introduced not only as the anode, but also as a cathode material in the lithiated transition metal oxide form ($LiMO_2$) rendering lithium in the cell.[25-29] This evolution improved significantly these rechargeable batteries providing higher energy density and consequently capturing the market.[30, 31]

It is not until recently that electrochemical capacitors (ECs) have received widespread concerns from researchers and extensive efforts have been made to develop high-performance Li-ion and other sophisticated secondary batteries with nanomaterials or organic redox couples.[32-34] In the process of charge and discharge, LIBs deliver and uptake power slowly. Because of this, it is of great necessity to develop energy storage systems with both high speed and high power in various applications and ECs can satisfy these conditions. Known as supercapacitors, ECs are employed for the purpose of fast power delivery and recharging. **Figure 2.1** displays the plot of specific energy and charging time demonstrated by an electric double layer capacitor (EDLC) and a high rate LIB[35]. From this plot, it can clearly be seen that an optimal LIB for high power shows constant energy density when the discharge time exceeds 10 minutes. However, this energy falls when the timescale is shortened. The reason for this may be that a range of resistive losses results in a consequent sluggish electron and ion transport occurrence in a battery cell.[36] Heat can thus be generated due to these resistive losses, especially at high rates, and severe safety issues like thermal runaway may be triggered accordingly.[37, 38] In addition, commercialized EDLCs provide constant energy densities all the time but they exhibit low storage energy capacities. A timeframe ranging from 10 s to 10 min is optimal for the outstanding performance exhibited by EDLCs and LIBs and also suitable for those pseudocapacitive materials.[35]

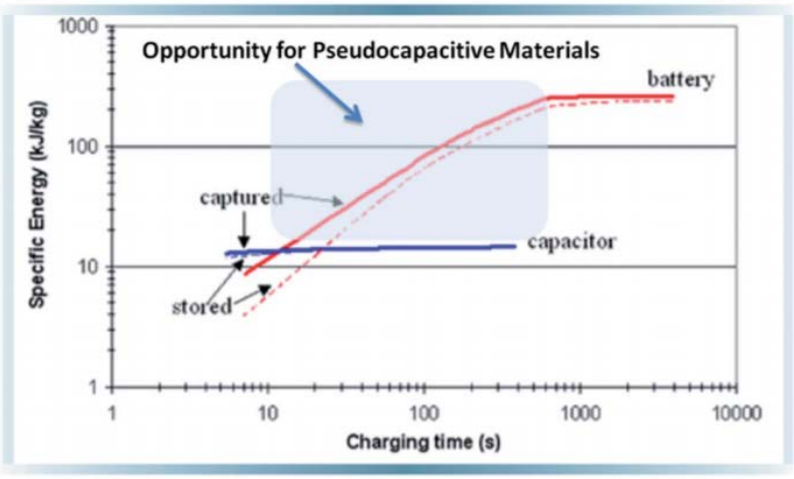

Figure 2.1 Energy vs. charging time for an EDLC and a lithium-ion battery. The region between ~10 s and 10 minutes represents the time domain where high-rate pseudocapacitive materials could offer higher energy and power densities comparatively with lithium-ion batteries and EDLCs.[35] (Reproduced with permission. 2014, RSC)

On the other hand, to cope with energy and environmental problems, the technology of lithium-air batteries (LABs) is regarded as a promising future technology at present.[39-43] Extensive efforts have been made to investigate advanced LABs and remarkable achievements have been gained in this realm. Despite the great potential exhibited by LABs in the applications of efficient energy storage, many limitations need to be addressed before the full implementation can take place. In this regard, advanced cathodes are therefore required to enable the reversible electrochemical reactions between Li and O_2.[44, 45] The current deficiency in the full cognition of some mechanisms highlights the great emphasis that should be given to the understanding and clarification of fundamental reaction mechanisms of LABs in order to guide our future research.

2.2 The development of supercapacitors

2.2.1 The concept of supercapacitors

The supercapacitor is a device for power storage which was developed in the 1970s and 1980s. The name of “supercapacitor” comes from its propriety to deliver a vast amount of energy in a relatively short period of time, that is to say, it can generate high power density to supply periods of high energy demand.[46-48] Being ten times larger

than that of the secondary batteries, high power density is the most noticeable feature of a supercapacitor.[49, 50]

ECs can be categorized into different types according to their various charge storage mechanisms and used active materials. EDLCs tend to be one of the most frequently used devices at the moment which employ high surface area active materials based on carbon.[51-53] Rapid and reversible reactions on the surface or near the surface to store charge happen in pseudocapacitors or redox supercapacitors, which are a second group of ECs.[54-56] The common active materials for pseudocapacitors are likely to be transition metal oxides and polymers conducted by electricity.[57, 58] Hybrid capacitors, the latest type of EC, integrate a capacitive or pseudocapacitive electrode with a battery electrode, exhibiting mutual benefits from both the capacitor and the battery.[59, 60]

First proposed in 1957, an electrochemical capacitor was then made into a patent by Becker, in which carbon with a high specific surface area (SSA) was employed as an electrode in combination with a coated metallic current collector in a solution of sulphuric acid.[61] In 1971, a Japanese company called NEC and an American company named SOHIO joint developed aqueous-electrolyte capacitors in order to save power. This development could be regarded as the first generation of electrochemical capacitor utilized in commercial devices.[62] Subsequently, Conway and Craig made a significant contribution to the development of higher specific capacitance and lower internal resistance supercapacitors[63] from 1975 to 1981 through the usage of RuO_2 as an electrode. Since then, the direction of electrode materials development in supercapacitors shifted from carbon-based materials featured by high specific surface area to metal oxides and hybrid materials. Meanwhile, further research is also invigorated by various novel applications in public and private transportation vehicles (such as cars, trucks, trams, trains and buses), portable electronics, the production of renewable energy and even aerospace systems.[64]

2.2.2 Electric double-layer capacitor

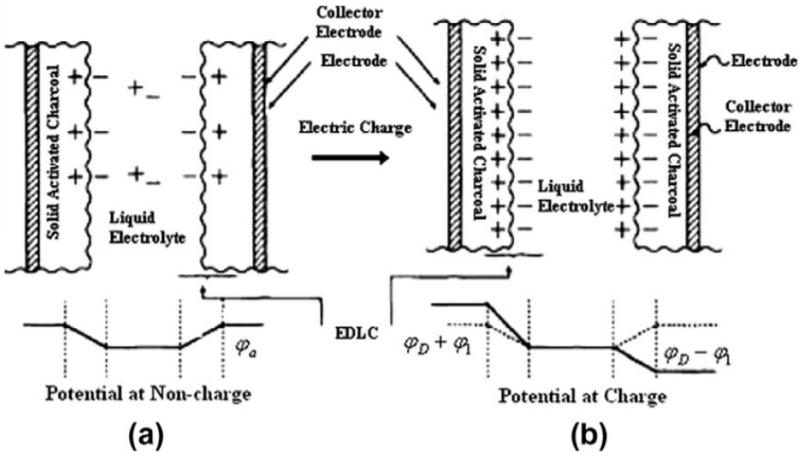

Figure 2.2 EDLC charge storage mechanism[46] (Reproduced with permission. 2010, ELSEVIER)

As electrochemical capacitors, electric double-layer capacitors (EDLCs) can store charge electrostatically in the process of reversible adsorption of electrolyte ions onto active materials, which are stable in an electrochemical condition and possess high accessible SSA. The 19th century witnessed the introduction and modelling of the EDLC concept by von Helmholtz, who studied the opposite charges distributed at the interface of colloidal particles.[65] **Figure 2.2** displays a schematic diagram of an electrical double layer capacitor.[46] In the Helmholtz double layer model (which is similar to two-plate conventional capacitor models), the formation of two layers of opposite charge occurs in the interface between the electrode and the electrolyte, which is an atomic distance. This interface of electrode/electrolyte emerges the charge separation on polarization, generating the double layer capacitance C, which was described by Helmholtz in 1853.

$$\mathrm{C} = \frac{\varepsilon_r \varepsilon_0 A}{d} \quad \text{or} \quad {}^{C}/_{A} = \frac{\varepsilon_r \varepsilon_0}{d} \tag{2.1}$$

in which ε_r represents the dielectric constant of the electrolyte, ε_0 symbolizes the vacuum dielectric, d refers to the double layer effective thickness (charge separation distance) and A means the surface area of the electrode.

Considering that the ions are homogeneously distributed in the electrolyte liquid mean and that they are forced through thermal motion, Gouy and Chapman further modified this simple model of Helmholtz EDLC. However, this new model overestimated the

capacitance of EDLC.[66, 67] The capacitance exhibited by two separated arrays of charges follows an inverse trend with their separation distance; therefore a rather large capacitance value is likely to appear when point charge ions are close to the surface of the electrode. Later, a combination of Helmholtz model and Gouy-Chapman model was put forward by Stern for the precise recognition of ion distributions in two regions, namely, the compact layer or Stern layer and the diffuse layer. Ions (normally hydrated) are adsorbed by the electrode in the compact layer and thus the name of compact layer is proposed. Moreover, specifically adsorbed ions (which in most conditions are anions regardless of the electrode charge features) and non-specifically adsorbed counter ions constitute the compact layer. Two categories of adsorbed ions can be distinguished, such as the inner Helmholtz plane (IHP) and the outer Helmholtz plane (OHP).[66] On the other hand, the diffuse layer region is defined by the Gouy-Chapman model. The EDLC (Cdl) capacitance is composed of the capacitances of the two regions: the capacitance from the diffusion region (Cdiff) and the capacitance from the Stern type of compact double layer (CH).Therefore, the following equation can be used to describe Cdl.[68]

$$\frac{1}{C_{dl}} = \frac{1}{C_H} + \frac{1}{C_{diff}} \tag{2.2}$$

Some of the factors that play decisive roles in the behaviour of EDLC at the surface of a planar electrode, are the electrolyte ion categories, the electrical field across the electrode, the solvent for the dissolution of electrolyte ions and the chemical affinity between the electrode surface and the adsorbed ions.[69, 70] The EDLC displays a more complex behaviour at the electrode's pore surface than at an infinite planar one because of the porous nature of the high SSA electrode.[71] Another reason is that a variety of parameters can affect the ion transportation dramatically in a rather isolated system, such as space limit inside the pores, rough mass transfer path, the ohmic resistance linked to the electrolyte, as well as the pore surface's wetting behaviour exhibited by the electrolyte.

The capacitance of the double layer is between 5 and 20 μF cm^{-2} depending on what electrolyte is utilized. Although higher specific capacitances can be obtained in water-phase acidic or alkaline solutions comparatively to in organic ones, extensive applications of organic electrolytes are welcome due to their greater tolerance of operation voltage (as high as 2.7 V in symmetric systems). According to the following

equation 2.3, a proportional relationship between the stored energy and the voltage (V) squared can be seen. This is why a voltage (V) with a three-fold enhancement leads to approximately an improvement of an order of magnitude in the stored energy (E) at a constant capacitance.[72]

$$\mathrm{E} = \frac{CV^2}{2} \tag{2.3}$$

Since charge is stored electrostatically, no Faradic (redox) reaction is observed at the electrodes of EDLC, as displayed in **Figure 2.2**. From the perspective of electrochemistry, a supercapacitor electrode should be regarded as a blocking electrode. This dominant difference derived from batteries implies that the electrochemical kinetics present no limitation through polarization resistance. Additionally, energy capture and delivery are very quick in this surface storage mechanism and thus superior power performance is demonstrated. The swelling among the active material presented by batteries in the cycles of charge and discharge is eliminated by the lack of Faradic reactions. Batteries usually can sustain only a few thousand cycles at most but EDLCs are able to survive millions of cycles. Consequently, the electrolyte solvent is not included in the charge storage mechanism, which is different from LIBs in which it results in the interphase between solid and electrolyte with the employment of graphite anodes or high-potential cathodes. This does not restrict the selection of solvents, and electrolytes featured by excellent power performances at low temperatures (down to -40 °C) could be fabricated for EDLCs. However, these devices are in shortage of energy density due to the electrostatic surface charging mechanism, which clarifies the reason behind the growing attention on the improvement of energy performance and expansion of temperature limits range that cannot be tolerated by batteries in the present research of EDLC.[46, 67, 70]

EDLCs normally have different carbon-type electrodes with high SSA, including active carbon, carbide-derived carbon, carbon nanotube and graphene. The process of charging and discharging can be indicated by the following equation:[73]

$$\text{Positive electrode: } E_s + A^- \leftrightarrow E_s^+ || A^- + e^- \tag{2.4}$$

$$\text{Negative electrode: } E_s + C^+ + e^- \leftrightarrow E_s^- || C^+ \tag{2.5}$$

$$\text{Overall: } E_s + E_s + A^- + C^+ \leftrightarrow E_s^+ || A^- + E_s^- || C^+ \tag{2.6}$$

Es and || represent the surface layer of carbon electrode and double electric layer, respectively. C+ and A- symbolize the cation and anion in the electrolyte solution, correspondingly. The improvement of EDLC is mainly through the increase in the SSA and electrical conductivity of carbon materials. In this way, the contact area between electrolyte and electrode can be increased, which potentially leads to more active sites for the absorption of ions on the carbon electrode surface and improves both ionic and electronic mobility rates.

2.2.3 Pseudocapacitor

Pseudo-capacitive behaviour is known to describe rapid and reversible redox reactions in the active materials surface of some supercapacitors. A new type of electrochemical capacitance was discovered in RuO_2 in 1971 and termed as pseudocapacitance due to the reactions of Faradaic charge transfer.[74, 75] Generally speaking, a variety of transition metal (Ru, Mn, Zn, W, and Ni) oxides as well as conducting polymer (polypyrrole and polyaniline) materials have been utilized as pseudocapacitor electrodes.[76] The specific pseudo-capacitances are severely higher compared with those of the carbon materials with double layer charge storage, arousing strong attention in these systems. However, due to the application of redox reactions, pseudocapacitors, similar to batteries, usually lack stability in the cycling process.[66, 72]

Due to its excellent specific capacitance, perfect pseudocapacitive behaviour and good reversible property, amorphous hydrated ruthenium oxide tends to be one of the most desirable candidates to be applied as an electrochemical capacitor electrode.[77] Extensive studies have been done on ruthenium oxide (RuO_2) due to its conductivity and three different oxidation states within 1.2 V. In the past 30 years, scientific research has been focused on the pseudo-capacitive behaviour of RuO_2 presented in the acidic solutions, which can be illustrated as a rapid and reversible electron transfer (accompanied by the adsorption of protons on the RuO_2 particles surface). The equation 2.7 describes this electronic transfer in which the oxidation states of Ru can alter from (ii) up to (iv):[35]

$$RuO_2 + xH^+ + xe^- \leftrightarrow RuO_{2-x}(OH)_x \quad (2.7)$$

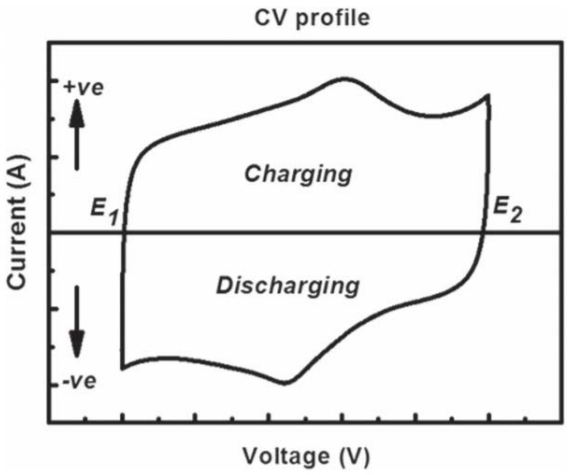

Figure 2.3 The CV shape of RuO_2 electrode.[78] (Reproduced with permission. 2016, IOP Publishing)

A Faradaic reaction of charge transfer can occur on the thin film electrode of RuO_2 due to the lack of protons in the electrolyte. Although the charge storage process presents the typical Faradaic nature, the cyclic voltammogram (CV) of the capacitor exhibits a rectangular shape (**Figure 2.3**). Distinctive electrochemical characteristics of pseudocapacitive processes were demonstrated while low gravimetric capacitance values (where only 4-7% of the Ru^{4+} atoms took part in the redox reaction) were reported previously.[79] A remarkable specific capacitance of 760 F g^{-1} (single electrode) was achieved for this material made by the sol-gel technique. Moreover, a recent modelling study has shown that electrode materials possessing both double layer and reversible redox processes can enhance the energy density of a device. The bulk material with a single crystal did not display a rectangular CV and this testifies the necessity for a porous and hydrated oxide. The following investigations enhanced the capacitance to more than 700 F g^{-1} through the identification of the significance of structural water (specifically, $RuO_2 \cdot nH_2O$ where n = 0.5) as well as a porous and nanoscale architecture.[80]

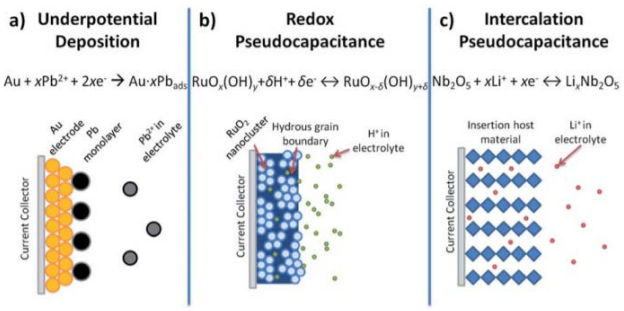

Figure 2.4 Different types of reversible redox mechanisms that give rise to pseudocapacitance: (a) underpotential deposition, (b) redox pseudocapacitance, and (c) intercalation pseudocapacitance.[35] (Reproduced with permission. 2014, RSC)

Some Faradaic mechanisms (pseudocapacitance) identified by Conway are likely to cause capacitive electrochemical characteristics as demonstrated in **Figure 2.4**, that is, underpotential deposition, redox pseudocapacitance (as in RuO_2), and intercalation pseudocapacitance.[35, 81] The underpotential deposition happens when an adsorbed monolayer is formed by metal ions at the surface of a different metal well above their redox potential. Lead on the surface of a gold electrode is one typical example of underpotential deposition.[82] Accompanied by transfer of Faradaic charge, redox pseudocapacitance happens when the adsorption of ions occurs electrochemically near the surface or onto the surface of a material. In a concomitant Faradaic charge-transfer without alteration in crystallographic phase, the intercalation pseudocapacitance can occur while ions intercalate into the layers or tunnels of redox active materials. Diverse physical processes, along with distinct types of materials result in the occurrence of the above three mechanisms. Electrochemical features are similar in some aspects because the potential and charge extent have a relationship. The extent of charge is influenced by the processes of adsorption and desorption that happen within the material's inner surface or at the interface between the electrode and the electrolyte.

$$E \sim E^0 - \frac{RT}{nF} \ln\left(\frac{X}{1-X}\right) \tag{2.8}$$

In equation 2.8[83], E represents potential (V), R symbolizes the ideal gas constant (8.314 J mol^{-1} K^{-1}), T refers to temperature (K), n means electrons number, F is the Faraday constant (96,485 C mol^{-1}), and X represents fractional coverage extent of the

inner or surface. In equation 2.9, the definition of a capacitance (C; F g^{-1}) may be in regions in which the plot of *E* vs. *X* presents a linear relationship:

$$\mathrm{C} = (\frac{nF}{m})\frac{X}{E} \tag{2.9}$$

In equation 2.9, *m* represents the molecular weight of the active material. Due to the not entirely linear plot of *E* vs. *X*, the capacitance is sometimes inconstant and thus pseudocapacitance is used to describe it. In spite of the relationship that illustrates the thermodynamic basis for pesudocapacitance, the kinetic behaviour of materials determines their applications in energy storage. This can be traced back to the fact that solid-state diffusion does not prevent reactions at the surface, or restricted by the surface, which can thus demonstrate high rate capability. This is a significant disparity between transition metal oxides with and without pseudocapacitive behaviours. Those with no pseudocapacitance are employed in rechargeable batteries, in which bulk solid state is used to store charge and eventually enhance energy densities. However, the solid state diffusion between the cathode and anode materials confines the power capability of these devices.[84]

2.2.4 Electrochemical properties of pseudocapacitance

As mentioned earlier, a range of processes can affect the pseudocapacitance. From an electrochemical perspective, pseudocapacitance can lead to particular features which will be depicted in this section. The storage of pseudocapacitive energy can be described based on its response to (a) a voltage sweep, as in a cyclic voltammetry; (b) a constant current, as in a galvanostatic cycling and (c) an alternating current, as in an impedance spectroscopy.[85-87]

The time range of a cyclic voltammetry experiment depends on the sweep rate (v, mV s^{-1}). Whether the redox reaction is controlled by diffusion or surface (therefore being capacitive) determines the current response to an implemented sweep rate. The current response changes with $v^{1/2}$ in a redox reaction which is restricted by semi-infinite linear diffusion, but the current is in direct variation with v in a capacitive process. Consequently, the current at a special potential can be illustrated by the general relationship below for any material (equation 2.10).[88]

$$i(V) = k_1 v^{1/2} + k_2 v \tag{2.10}$$

Separating the diffusion and capacitive currents enables the determination of k_1 and k_2 values at each potential. This mathematical method should be treated carefully because the mechanism is not established by the current relationships, therefore, it should be accompanied by other characterization approaches.[89-92] The performance of innovative nanostructured materials can be evaluated by this technique.

2.2.5 The development of electrode materials in supercapacitors

In general, the electrode supercapacitor materials can be divided into three categories, which are (1) carbon-based materials with high SSA; (2) conductive polymers; and (3) transition metal oxides.[93-95] The depictions of different systems will be discussed in detail in the following parts.

Carbon materials are regarded as promising electrode materials for industrial applications due to their rich sources, competitive prices, facile processing, benignancy, large specific surface area, excellent electronic conductivity, long-termed chemical stability and a wide range of operation temperatures.[96] Generally, charges are primarily stored by carbon materials in an electrochemical double-layered capacitor which is formed at the electrode/electrolyte interface instead of in the bulk of capacitive materials. Hence, the surface area near the electrolyte ions predominantly determines the capacitance. Specific surface area, shapes and structures of pores, distribution of pore sizes, surface functionality as well as electrical conductivity play essential roles in the electrochemical performance.[66, 96] Extensive investigations have been carried out using different carbon-based materials in the applications of electrode materials for ECs, such as activated carbons (ACs),[97, 98] graphites,[99, 100] carbon nanofibers,[101, 102] carbon aerogels (CAGs),[103, 104] carbon nanotubes (CNTs),[105, 106] and nanosized carbon. Their approachability, facile processing, no poisonousness, relatively low cost, good chemical stability, and wide range of operation temperatures are some of the reasons that justify the existence of such vast and well developed literature. In this aspect, various methods have been utilized to improve their specific surface area or adjust the distribution of pore sizes, resulting in substantial enhancement of power, energy and operation parameters of ECs.

As electrode materials, ACs are widely employed because they generally have large surface areas, medium costs and good electrical features. ACs are normally produced from the physical and/or chemical activation of different categories of carbonaceous

materials, such as wood, fruit, bamboo and pitch. With oxidizing gases like steam, air and CO_2, physical activation generally means that carbon precursors are treated by high temperature ranging from 700 to 1200 ^oC. Chemical activation, however, is often processed at lower temperatures (from 400 to 700 ^oC) in the presence of activating chemical reagents such as phosphoric acid, sodium hydroxide, potassium hydroxide, and zinc chloride. On the basis of various activation approaches and different carbon precursors, ACs (featured by unique physicochemical properties with surface area of 3000 $m^2\ g^{-1}$) have been generated and their electrochemical characteristics have also been massively investigated.[107-109] A one-pot pyrolysis, combined with the carbonization of red cedar precursor, was applied to produce a biochar material with distinctive hierarchically porous microstructures. The gravimetric capacitance increased dramatically to nearly 115 F g^{-1} by activating electrodes with diluted HNO_3 at room temperature, which is comparable to those of advanced carbon materials.[110] In addition, sugarcane bagasse carbon electrodes have specific capacitances ranging from 92 to 340 F g^{-1}.[111]

Particular and excellent electronic, optical, mechanical and chemical property characteristics, together with the large surface area, enable CNTs to be extensively applied as an excellent supercapacitor material. In addition, CNTs are cheap, stable and available. Electrodes on the basis of CNTs have already established a relatively mature market production. Just like other electrode materials, graphene sheets thick in one atom are superior to CNTs with a two-dimensional (2D) planar geometry and render more advantages than CNTs.[112] Electrodes on the basis of entangled multi-walled CNTs (MWCNTs) in free-standing mats with H_2SO_4 electrolyte have been utilized to fabricate a supercapacitor with a 102 F g^{-1} specific capacitance, a >8 kW kg^{-1} power density as well as a ~1 Wh kg^{-1}energy density.[113]. More recently, a specific capacitance as high as 180 F g^{-1} has been obtained with the usage of a random single-walled CNT (SWNCNT) network as the electrode in KOH electrolyte.[114]

Graphene, known as a 2D carbon monolayer, consists of sp^2-hybridized carbons. Materials based on graphene are promising candidates to be applied in supercapacitors and other devices for energy storage as a result of their desirable properties, namely, highly adjustable surface area, excellent chemical stability, good electrical conductivity and outstanding mechanical behaviour.[115-117] The gravimetric capacitance of a hybrid type film is 233 F g^{-1} and its volumetric capacitance is 135 F

cm^{-3}.[118] Increasing the current density from 10 to 100 A g^{-1}, it witnessed a specific capacitance of 1046 F g^{-1} and a maintenance of 96% of capacitance, which indicates an outstanding retention ability.[119] Moreover, the active surface area of the electrode is significantly improved by a nanowire-based structure, which also increases the interfacial area and curtails the paths of ionic diffusion. A specific capacitance of 740 F g^{-1} (or 581 F cm^{-3}) was obtained when the current density was 0.5 A g^{-1}. After 1000 cycles of charge and discharge, 87% of the specific capacitance was retained at 10 A g^{-1}current density.[120]

Activated carbon fibers (ACFs), carbon onions and carbon aerogels (CAGs) are other carbon structures that have been investigated as well in the applications of supercapacitors. In general, high specific area, along with excellent electrical conductivity, are criteria for ideal materials as supercapacitor electrodes. With specific surface areas as high as 3000 m^2 g^{-1}, ACFs usually have decent controllable pore size distribution.[121] They are typically generated from carbonizing fibrous carbon precursors followed by the processes of activation. Recently, it has been reported that a high capacitance of 371 F g^{-1} is achieved utilizing a KOH electrolyte solution. The problem of long term stability, however, may be caused by surface functional groups as well as high specific surface area.[122] Additionally, the production of ACF is much more expensive than that of the AC. CAGs stand as another intriguing material type for supercapacitor electrodes from the fact that they are ultralight, not dependent on binding substances and highly porous (containing mesopores in majority).

Various advantages enable the application of conducting polymers as suitable supercapacitor materials, such as the environmental friendliness, low cost, high voltage window, excellent conductivity in a doped condition, good storage capacity, porosity, or reversibility, as well as tuneable redox activity via chemical modification. Capacitance behaviours presented by conducting polymers occur via the redox process. The transfer of ions to the backbone of the polymer happens during the oxidation and the release of ions from the backbone to the electrolyte takes place in the reduction process. These redox reactions will occur in the entire bulk and not just the surface of the conducting polymer.[123] The reactions of charge and discharge are highly reversible due to no occurrence of structural changes such as phase alterations.[93] A composite material with polypyrrole, carbon fibres grown by vapour and carbon thick in 5-10 nm was fabricated by Kim et al. through in situ chemical polymerization and

specific capacitances of 588 and 550 F g^{-1} were achieved respectively at potential scan rates of 30 and 200 mV s^{-1}.[124] Polypyrrole electrodes polymerized by pulse were utilized by Desu et al. in the electrochemical supercapacitor with high energy density. These structures exhibited an extremely high specific capacitance of 400 F g^{-1} and an exceptionally high energy density of 250 Wh kg^{-1} beyond expectation.[125] A facile one-pot approach with no template was employed to synthesize large arrays of polyaniline (PANI) nanowires in vertical alignment, which exhibited specific capacitances as high as 950 $F \cdot g^{-1}$ and 780 $F \cdot g^{-1}$ when charge/discharge current density was as large as 40 A g^{-1} respectively.[126]

The storage of pseudocapacitive charge can be achieved by different transition metal oxides in aqueous electrolytes. Factors such as material structure, hydration traits as well as the electrolyte determine the behaviours of these materials. Aqueous and non-aqueous pseudocapacitive materials differ greatly in the effects of structural and surface-bound water due to having a large "inner surface" accessible to ion adsorption caused by structural water, as in $RuO_2 \cdot nH_2O$.[127] Meanwhile, the structural water may facilitate ions to diffuse into the inner surface. To be applied in supercapacitors, metal oxides should meet the following requirements: (1) decent electrical conductivity, (2) two or more oxidation states can be presented by the metal that exists mutually in a continuously wide range without phase alterations, which involves the irreversible change of a 3D structure, and (3) the intercalation of protons can be conducted freely into the oxide lattice during reduction (and out of the lattice during oxidation), allowing easy interconversion between O_2 and OH^-.[35] Up to now, these studied metal oxides include ruthenium oxide, cobalt oxide, manganese oxide, nickel oxide and vanadium oxide. Extensive studies have been conducted regarding RuOx due to its highly reversible redox reactions, excellent proton conductivity, desirable thermal stability, remarkable specific capacitance, broad potential window, good rate capability, metallic conductivity and three different oxidation states available in a voltage window of 1.2 V.[128-130] With respect to RuO_2 electrodes, only 10% of the accumulated charge can be generated by the double-layer charging, paralleling with which the mechanism of redox pseudocapacitance can happen. Distinct reactions are involved in the pseudocapacitive behaviours of RuO_2 in acidic and alkaline solutions, demonstrating various sensitivities towards crystallinity. However, the changes of RuO_2 valency state in an alkaline environment are rather different. When the

composite of carbon and ruthenium is charged, the RuO_2 in the composite electrode is suggested to be oxidized to RuO_4^{2-}, RuO_4^-, and RuO_4, and when discharged, the compounds with these high valency states are reduced to RuO_2. The carbon/RuO_2 composite materials enjoy the advantages of both pseudocapacitors and double electric layer capacitors, benefiting from the application of the Ru metal and the typically lower cost of supercapacitors based on RuO_2.[35] A novel graphene foam was synthesized by Ozkan et al., which was covered conformally by RuO_2 nanoparticles and anchored CNTs. Outstanding gravimetric and per-area capacitive performance (specific capacitance: 502.78 F g^{-1}, areal capacitance: 1.11 F cm^{-2}) were demonstrated by supercapacitors on the basis of this material, which eventually results in a particularly high power density of 128.01 kW kg^{-1} and energy density of 39.28 Wh kg^{-1}.[131] A RuO_2/MWCNT composite has been prepared by Yan et al.[132] and it displayed a specific capacitance value of 494 F g^{-1} at the CV scan rate of 50 mV s^{-1}. This material was also fabricated by Liu and co-workers where a maximum specific capacitance value of approximately 803 ± 72 F $g^{-1}$was obtained[133]. The facile sonication method was utilized to prepare a carbon/$RuO_x(OH)_y$ composite in a coconut shell with a 250 F g^{-1} specific capacitance value.[134]. In addition, a chemical method was applied to obtain a polyaniline/Nafion/hydrous RuO_2 composite which reported a specific capacitance of 475 F g^{-1}.[135]

Mn oxide is more desirable than Ru oxide to be practically applied as an electrode material of supercapacitors due to its relatively lower cost. Generally, in an aqueous electrolyte, the storage of pseudocapacitive charge of MnO_2 happens via Mn redox between the oxidation states of +4 and +3 in the bulk or at the surface:

$$\mathrm{Mn}O_2 + xA^+ + xe^- \leftrightarrow A_xMnO_2 \qquad (2.11)$$

In the equation 2.11, *A* symbolizes a generic alkali metal cation. From a theoretical perspective and assuming the potential window of 0.9 V, the 1-electron redox reaction corresponds to 1233 F g^{-1} (1110 C g^{-1}) when x = 1. However, the main defects of pseudocapacitors based on Mn oxides tend to bring poor rate performances and low electrical conductivities. To deal with these inherent demerits of Mn oxide electrodes, more attentions should be given to the novel pseudocapacitors with higher conductivity equipped with metal oxides and well developed pore structures. Wang et al.[136] have obtained an α-MnO_2 electrode with a surface area of 284 m^2 g^{-1} and this

work showed that the 3D MnO_2 electrode material presented a specific capacitance of 200 F g^{-1}. Additionally, MnO_2 electrode with amorphous nanostructure has been successfully prepared by adding $KMnO_4$ into ethylene glycol in the ambient conditions, which shows great stability as high as 1200 cycles at a capacitance of 250 F g^{-1}.[76]. A method of exfoliation and reassembling has been adopted to prepare 2D nanosheets of MnO_2, achieving a specific capacitance of nearly 140-160 F g^{-1} and a cyclic stability of ~93-99% with 1000 cycles.[137] Unlike RuO_2, poor conductivity is its major drawback. Besides, in the processes of charge and discharge, only surface atoms are involved, which eventually lowers its utilization. Some efforts, mainly by combining this material with CNTs, have so far been made to overcome this problem.[138] Through the optimization of CNT synthesis parameters and MnO_2 electrodeposition processes, a nanostructured composite electrode was prepared by R. Amade et al., which was characterized by dense and long CNTs in vertical alignment with high SSA and a thin layer of MnO_2. A much higher specific capacitance of 642 F g^{-1} than that of activated carbon/MnO_2 composite electrodes was achieved at a scan rate of 10 mV s^{-1}, which may be primarily due to the presence of large surface area and good conductivity of CNT.[139, 140]

Cobalt oxide (Co_3O_4) has been regarded as a promising alternative to be the electrode material of supercapacitors due to its large surface area, good conductivity, outstanding reversible redox behaviours, stable performance, and excellent tolerance to corrosion. Chemical coating Co_3O_4 thin films onto copper substrates achieved a specific capacitance of 118 F g^{-1} for a Co_3O_4 electrode.[141] Nickel oxide is also a candidate material for supercapacitors given the fact that it possesses many advantages such as facile synthesis, environmental benignancy, low cost and relatively good theoretical specific capacitance of 3750 F g^{-1} [142-145]. It is suggested that crystallinity strongly determines the electrochemical surface reactivity of NiO and the preparation process affects its electrochemical behaviour dramatically.[146] For instance, prepared by a chemical process, NiO featured by a cubic structure exhibited a maximum specific capacitance of 167 F g^{-1}. However, porous NiO synthesized by a sol-gel method displayed a specific capacitance of 200-250 F g^{-1}, which achieved 696 F g^{-1} after being annealed at 250 ^{o}C.[147, 148] The major drawbacks of NiO-based materials as supercapacitor electrode are likely to be their relatively poor cycle performance and strong resistivity.

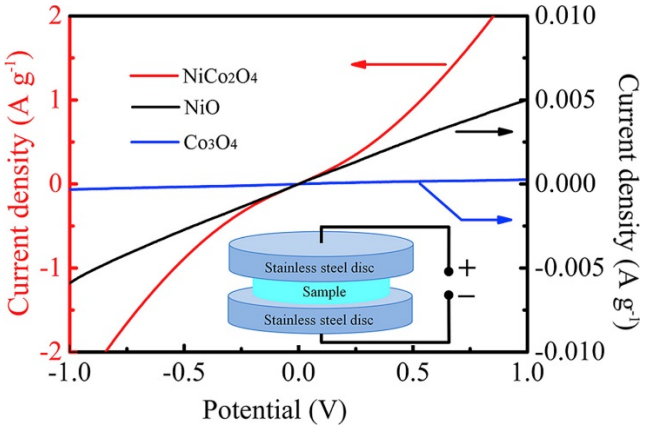

Figure 2.5 I–V curves of the $NiCo_2O_4$, NiO and Co_3O_4 samples.[149] (Reproduced with permission. 2014, ELSEVIER)

The spinel crystal structure in the general formula of AB_2O_4 is essential for supercapacitor. 3D diffusion pathways are offered by this robust crystalline framework. Various spinel compounds have already been studied for electrochemical capacitors, such as Mn_3O_4,[150] Fe_3O_4,[151] and Co_3O_4,[152] together with a mixture of transition metal spinels like $MnFe_2O_4$ and $NiCo_2O_4$.[153, 154] Distinctive pseudocapacitive properties including mainly rectangular CVs are exhibited by Mn_3O_4, Fe_3O_4, and $MnFe_2O_4$. Exceptionally high capacitance values are presented by $NiCo_2O_4$ even at relatively short charge/discharge time, which may be due to the excellent electronic conductivity of approximately 62 S cm^{-1} presented by discharged material and the utilization of cobalt and nickel redox behaviours. The sequence of electrical conductivity of $NiCo_2O_4$, NiO, and Co_3O_4 can be inferred from **Figure 2.5**, and many studies have proved that the resistance of $NiCo_2O_4$ is indeed lower than that of NiO and Co_3O_4. Redox reactions provided by $NiCo_2O_4$ are believed to offer superior results to those by monometallic oxides of Co_3O_4 and NiO. In addition, rich redox reactions can be rendered by various oxidation states and multiple nanostructures so that more charges can be stored by the spinel type $NiCo_2O_4$. Last but not least, in addition to the accessibility of nickel and cobalt on earth, $NiCo_2O_4$ is widely applied as an electrode material due to its benignancy and relatively low cost.[155] To some extent, $NiCo_2O_4$ can complement or replace electrode materials on the basis of NiO, Co_3O_4 and RuO_2 in the area of energy storage. In an alkaline environment, $NiCo_2O_4$ is reported to present a potential window of 0-0.55 V and its electrolyte pseudocapacitive behaviour in this environment can be expressed by the following equations:[156-158]

$$NiCo_2O_4 + OH^- + H_2O \leftrightarrow NiOOH + 2CoOOH + e^- \quad (2.12)$$

$$CoOOH + OH^- \leftrightarrow CoO_2 + H_2O + e^- \quad (2.13)$$

It is noticeable that changes of valence states between Co^{3+} and Co^{4+}, as well as M^{2+}/M^{3+} (M = Co or Ni) occur on the electrode materials surface, in which the rapid and reversible Faradaic reactions take place.[159, 160] M^{2+}/M^{3+} and Co^{3+}/Co^{4+} transitions have close electrochemical redox potentials and thus an overlapping redox peak is observed. Moreover, double layer capacitance as well as excellent pseudocapacitance (which normally is 10-100 times higher) are exhibited by metal oxides; consequently, double layer capacitances demonstrated by CV curves for the electrodes are barely observed as they belong to much lower orders of magnitude.[161] Unfortunately, as an electrode material for supercapacitors, the theoretical capacitance of $NiCo_2O_4$ has not been calculated yet and more specific evidences should be provided to elucidate the storage mechanism of this special material. The supercapacitive performance can also be evaluated by the capacity retention rate. Some studies intriguingly reveal that after several hundred cycles the specific capacitance of $NiCo_2O_4$ grows to some extent and this phenomena was ascribed to their distinctive morphologies and activation processes. Therefore, it can be concluded that supercapacitive performance is likely to be greatly influenced by the mass loading of $NiCo_2O_4$. In order to store more charges and reduce the effect of mass loading, it is crucial to prepare unique structures with distinctive morphology, large SSA and well-defined size so that this material can be used at its full potential. The $NiCo_2O_4$ electrode with a unique network is characterized by excellent cyclability as well as specific capacitances of 587 F g^{-1} and 518 F g^{-1} at 2 A g^{-1} and 16 A g^{-1} respectively when the loading mass is 5 mg cm^{-2}.[162] Furthermore, at the same loading mass, $NiCo_2O_4$ with a structure of nanowall network exhibits a specific capacitance of 1225 F g^{-1} at 5 A g^{-1} in comparison with $NiCo_2O_4$ nanoflakes which shows 844 F g^{-1} at 1 A g^{-1}.[163] Similarly, Chen et al. reported hierarchically 3D $NiCo_2O_4$ nanosheet-nanowire cluster arrays induced by NH_4F with better electrochemical performance than nanowire arrays, which corroborates the potential superiority of this material.[156]

2.3 The perovskite oxide electrode in oxygen ion intercalation supercapacitors

2.3.1 Perovskite oxide

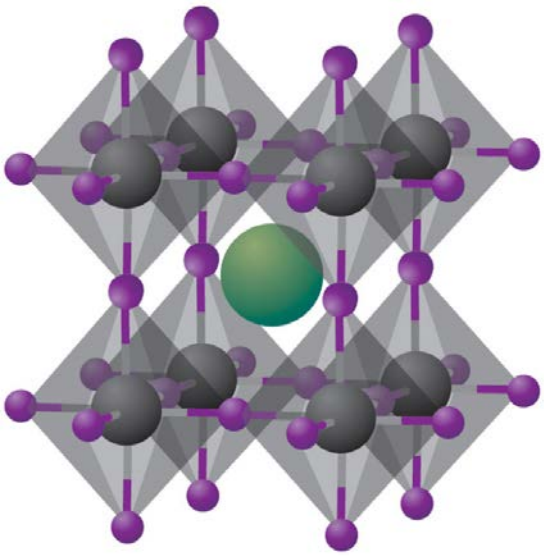

Figure 2.6 Crystal structure of cubic metal perovskites with the generic chemical formula ABX_3.[164] (Reproduced with permission. 2014, NATURE PUBLISHING GROUP)

The general formula of perovskites is ABX_3 and its structure is displayed in **Figure 2.6**. The B cation generally tends to be a rare earth or a transition metal with a valence state of +4 and it is located in the centre of a six-coordinated octahedron neighboured by oxygen ions. With a valence state of +2 and a coordination number of 12, the A site cation ionic radius is usually larger than that of the B site cation.[165] The perovskite structure is named after the Russian mineralogist Lev Perovski and the calcium titanium oxide ($CaTiO_3$) was the first mineral of this structural family to be discovered. Various physical and chemical features in bulk are exhibited by the perovskite oxide family because they have flexible electronic structures which are symbolized by the electronic states distribution. These properties include ferroelectricity in $PbTiO_3$, lithium mobility in $(Li,La)TiO_3$, colossal magnetoresistance in $La_xCa_{1-x}MnO_3$, pseudocapacitors intercalated by anions in $LaMnO_{3-\delta}$, proton conductivity in $(Ba,Sr)CeO_3$, and oxygen ion diffusion in $LaGaO_3$ regarding solid-state devices like solid oxide fuel cells (SOFCs). Inorganic oxides with perovskite type structures have the common formula of $AB_{1-x}M_xO_{3-\delta}$, in which M refers to a trivalent dopant element and δ represents the oxygen deficiency per unit cell. The replacement of the M dopant cation in the B site generates oxygen vacancies, influencing greatly the proton

conduction.[166-168] The equation 2.14 uses Kröger-Vink notation to represent the partial substitution of the B cation with a generic M dopant in trivalent state, which consequently creates oxygen vacancies (in order to rebalance the valence charge).

$$2B_B^X + O_O^X + M_2O_3 \leftrightarrow 2M_B' + V_O^{\bullet\bullet} + 2BO_2 \quad (2.14)$$

The inherent traits of the perovskite oxides in the ambit of electrical performances can also be affected by lattice distortions, which result from these larger ionic radius substitutions into A or B cation positions. For the undoped material, it is generally believed that change in unit cell volume can be used to measure the doping-induced strain. The Goldschmidt tolerance factor (t, which is revealed in the equation 2.15) can describe how much a perovskite structure is distorted from an ideal cubic structure:

$$t = \frac{(R_A + R_O)}{\sqrt{2}(R_B + R_O)} \quad (2.15)$$

In which R_A and R_B represent the respective ionic radii of the cations on the A and B sites, and R_O refers to the ionic radius of oxygen. Stable perovskite structures will generally be observed with t between 0.75 and 1.0. The cubic symmetry can be obtained for $0.95 \leq t \leq 1.04$, while typically orthorhombic or rhombohedral symmetries are presented by compounds when t is in the range of 0.75-0.90.[169, 170]

As it was stated before one common approach to tailor the perovskite compound properties is to substitute cations partially in either A or B sites also using different dopant ratios. However, special interest has recently been given to replace half cations at the B site with another cation. Under this condition, two cations, B' and B", can either be disordered in this position, or they may remain ordered to form a so-called B-site ordered double-perovskite written as $A_2B'B"X_6$. **Figure 2.7** shows three diverse ways of how the cations are ordered. Also, the expansion of combinations varieties of B-site cation oxidation states could be done with two different aliovalent A-site cations, (namely $A'A"B'B"O_6$), which would considerably enlarge the compounds number.

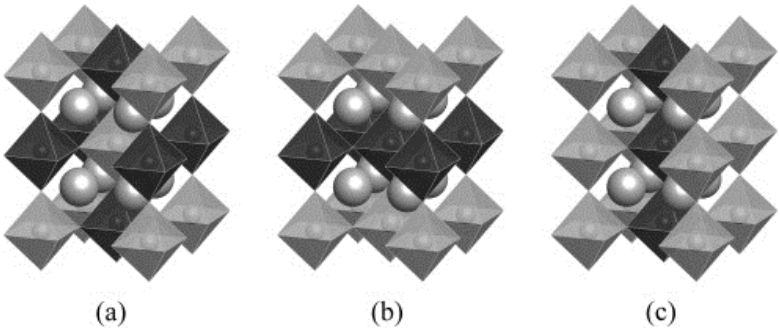

Figure 2.7 Diverse *B*-site cation orderings in $A_2B'B''O_6$ perovskites: (a) rock-salt, (b) layered and (c) columnar order.[171] (Reproduced with permission. 2015, ELSEVIER)

2.3.2 Oxygen ion intercalation capacitance in perovskite oxide

In 1973, Kudo et al. first demonstrated that $Nd_{1-x}Sr_xCoO_{3-\delta}$ perovskite oxide showed reversible electrochemical intercalation of oxygen into the crystal lattice in a KOH solution at room temperature. The calculated diffusion constant reached 1.4×10^{-11} cm^2 s^{-1}, which is much larger than that of ordinary oxides.[172] Following that, a common phenomenon presented by perovskites and perovskites-based structures which tends to happen is the reversibly topotactic intercalation of oxygen. Superconductor perovskite $YBa_2Cu_3O_{6+\delta}$ was demonstrated to be characteristic of oxygen intercalation at high temperatures accompanied by an orthorhombic-tetragonal structure transition.[173] Generally, two processes exist in the oxygen diffusion into the material. On one hand, rapid diffusion happens through a network of extended defects; on the other hand, structural changes can be observed in processes of slow diffusion (which occur inside microdomains in the enclosure of the defect network [174-176]). After that, the mechanism of oxygen intercalation in the $SrCoO_{3-\delta}$ perovskite was thoroughly investigated by X-ray absorption near-edge structure (XANES) spectroscopy. The procedures of oxygen intercalation in $SrCoO_{3-\delta}$ are as follows: (1) oxygen in the form of superoxide ions (O_2^-) were in the first place adsorbed on active materials surface, (2) it subsequently splits into O_x^- in the reduction process combined with square-pyramidally coordinated cobalt; (3) lastly it is re-oxidized to O_z^- ($0 < z < x$) in the bulk which is attached to octahedrally coordinated cobalt.[177] Based on the above mentioned oxygen intercalation processes, reduced $LaMnO_3$ perovskite oxide was used as a pseudocapacitive electrode in supercapacitors under alkaline electrolytes.[178] During the pseudocapacitive electron storage process, the intercalation of oxygen ions in the electrolyte can fill the oxygen vacancies and diffuse O_2^- through the crystal along

the octahedral edges, accompanied by the oxidation of two Mn^{2+} to Mn^{3+}. After that, the intercalation of surplus oxygen occurs at the surface when manganese is diffused , resulting in the proportional formation of two Mn^{4+} ions from the oxidation of each pair of Mn^{3+} ions. These intercalation processes demonstrated that higher concentration of oxygen vacancies can consequently improve the storage of O_2^- during the intercalation, thus increasing the pseudocapacitance in the charge-discharge process (**Figure 2.8**)[178]. Inspired by this, Shao et al. designed a Nb-doped $SrCoO_{3-\delta}$ perovskite oxide with high concentration of oxygen vacancies. When used as an electrode in pseudocapacitors, the Nb-doped $SrCoO_{3-\delta}$ perovskite exhibited an exceptionally high volumetric capacitance of nearly 2034.6 F cm^{-3} with a 0.5 A g^{-1} current density and after 3000 cycles, it preserved an outstanding cycling stability with 95.7 % of capacity retention.[179]

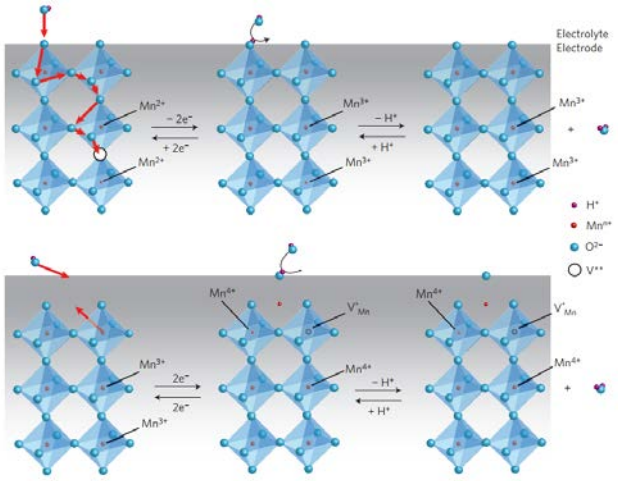

Figure 2.8 Mechanism of oxygen intercalation into $LaMnO_{3\pm\delta}$.[178] (Reproduced with permission. 2014, NATURE PUBLISHING GROUP)

2.4 Oxygen electrochemistry in energy storage applications

A Li-air battery has a theoretical specific energy density of 5,200 Wh kg^{-1} (considering the mass of lithium anode and the oxygen (O_2) gained during discharge), whereas in a Li-ion battery the corresponding theoretical value is only 150 Wh kg^{-1}. Although Li_2O is more likely to be formed at high discharge rates, Li_2O_2 is the product of the reduction process. The possible mechanism at the cathode involves the reactions below (represented by the equations 2.16, 2.17 and 2.18) which are normally named as oxygen reduction reaction (ORR):

$$O_2 + Li^+ + e^- \rightarrow LiO_2 (3V\ vs.\ Li/Li^+) \qquad (2.16)$$

$$2LiO_2 \rightarrow Li_2O_2 + O_2 \quad (2.17)$$

$$LiO_2 + Li^+ + e^- \rightarrow Li_2O_2\ (3.1V\ vs.\ Li/Li^+) \quad (2.18)$$

Ogasawara et al. demonstrated that Li_2O_2 decomposes electrochemically into Li and O_2 in the charging process, and the following equation 2.19 describes the relevant oxygen evolution reaction (OER):

$$Li_2O_2 \rightarrow 2Li^+ + 2e^- + O_2 \quad (2.19)$$

The reactions of O_2 reduction and evolution have different pathways. Peng et al. conducted an in situ spectroscopic study of O_2 reaction in an aprotic electrolyte and demonstrated that before the final product Li_2O_2 was formed, LiO_2 was an intermediate species in the reaction of O_2 reduction. However, Li_2O_2 broke down directly in one-pot reaction to generate O_2 and LiO_2 was not produced as an intermediate product.

Carbon materials are ideal ORR catalysts as a result of their desirable conductivity, good durability, excellent mechanical strength and reasonable cost. Therefore, as promising alternatives to metal-based catalysts, they are most commonly applied in lithium-air batteries. In addition to the above advantages, large SSA exhibited by carbon materials can provide extra active sites for the ORR.[180] Commercially produced from heavy petroleum products, carbon black (CB) is featured by high surface area (but still lower than activated carbon) and excellent electrical conductivity (making it frequently utilized as a reinforcing material). In the field of power production, CB is in the exclusive application as a catalyst support in lithium-air batteries or low-temperature fuel cells. However, in comparison with Pt or other catalysts based on metal, CB shows poor catalytic activity for ORR.[181] Activated carbon (AC), compared to those metal-based ORR catalysts, is regarded as a desirable and inexpensive candidate to be the electrode material. In the air-cathode system subject, similar or even greater performances are demonstrated by AC in the real application of lithium-air batteries, nevertheless the highest ORR overpotential reduction is possessed by a Pt catalyst. In addition, the ORR property of AC air electrode is largely influence by the fabrication method. Graphene, characterized by sp^2-hybridized carbon atoms in a 2D honeycomb-like framework,[182, 183] has so far received considerable attention from the fundamental science and applied studies.[184] ORR activity was attempted to be significantly enhanced via coating graphene simply using a Nafion binder on the cathode of CC, yet the activity was not higher and in fact,

it revealed itself to be lower than that of a cathode modified by Pt and CB.[185] Greater stability of ORR activity is also offered by the graphene support in comparison with the Pt catalyst.[186] Graphene functions as an ORR catalyst in a PANI composite and its proper addition could enhance the power density by 116 times relative to that of the graphite electrode through decreasing both the ohmic resistance and charge transfer.[187, 188]

2.5 Reference

[1] H. Lund, Energy, 32 (2007) 912-919.

[2] I. Dincer, Renewable Sustainable Energy Rev., 4 (2000) 157-175.

[3] S. Chu, A. Majumdar, Nature, 488 (2012) 294.

[4] J. Goldemberg, Science, 315 (2007) 808.

[5] S.D. Pohekar, M. Ramachandran, Renewable Sustainable Energy Rev., 8 (2004) 365-381.

[6] T.E. Springer, T.A. Zawodzinski, S. Gottesfeld, J. Electrochem. Soc., 138 (1991) 2334-2342.

[7] B.C.H. Steele, A. Heinzel, Nature, 414 (2001) 345.

[8] E.P. Murray, T. Tsai, S.A. Barnett, Nature, 400 (1999) 649.

[9] J.K. Nørskov, J. Rossmeisl, A. Logadottir, L. Lindqvist, J.R. Kitchin, T. Bligaard, H. Jónsson, J. Phys. Chem. B, 108 (2004) 17886-17892.

[10] S.C. Singhal, Solid State Ionics, 135 (2000) 305-313.

[11] M.S. Whittingham, R.R. Chianelli, J. Chem. Educ., (1980).

[12] S.Y. Huang, L. Kavan, I. Exnar, M. Grätzel, J. Electrochem. Soc., 142 (1995) L142-L144.

[13] N. Liu, Z. Lu, J. Zhao, M.T. McDowell, H.-W. Lee, W. Zhao, Y. Cui, Nat. Nanotechnol., 9 (2014) 187.

[14] F. Croce, A. D' Epifanio, J. Hassoun, A. Deptula, T. Olczac, B. Scrosati, Electrochem. Solid-State Lett., 5 (2002) A47-A50.

[15] C.K. Chan, H. Peng, G. Liu, K. McIlwrath, X.F. Zhang, R.A. Huggins, Y. Cui, Nat. Nanotechnol., 3 (2007) 31.

[16] C. Liang, N.J. Dudney, J.Y. Howe, Chem. Mater., 21 (2009) 4724-4730.

[17] J.M. Tarascon, M. Armand, Nature, 414 (2001) 359.

[18] S. Xin, L. Gu, N.-H. Zhao, Y.-X. Yin, L.-J. Zhou, Y.-G. Guo, L.-J. Wan, J. Am. Chem. Soc., 134 (2012) 18510-18513.

[19] D. Bresser, S. Passerini, B. Scrosati, Chem. Commun., 49 (2013) 10545-10562.
[20] P. He, H. Yu, D. Li, H. Zhou, J. Mater. Chem., 22 (2012) 3680-3695.
[21] H. Wang, Y. Yang, Y. Liang, J.T. Robinson, Y. Li, A. Jackson, Y. Cui, H. Dai, Nano Lett., 11 (2011) 2644-2647.
[22] K. Kang, G. Ceder, Phys. Rev. B, 74 (2006) 094105.
[23] K. Kang, Y.S. Meng, J. Bréger, C.P. Grey, G. Ceder, Science, 311 (2006) 977.
[24] V. Etacheri, R. Marom, R. Elazari, G. Salitra, D. Aurbach, Energy Environ. Sci., 4 (2011) 3243-3262.
[25] A.L.M. Reddy, A. Srivastava, S.R. Gowda, H. Gullapalli, M. Dubey, P.M. Ajayan, ACS Nano, 4 (2010) 6337-6342.
[26] D. Aurbach, E. Zinigrad, Y. Cohen, H. Teller, Solid State Ionics, 148 (2002) 405-416.
[27] R. Yazami, P. Touzain, J. Power Sources, 9 (1983) 365-371.
[28] E. Peled, C. Menachem, D. Bar-Tow, A. Melman, J. Electrochem. Soc., 143 (1996) L4-L7.
[29] M. Yoshio, H. Wang, K. Fukuda, Y. Hara, Y. Adachi, J. Electrochem. Soc., 147 (2000) 1245-1250.
[30] J. Li, E. Murphy, J. Winnick, P.A. Kohl, J. Power Sources, 102 (2001) 294-301.
[31] B. Scrosati, Electrochemistry of Novel Materials, by J. Lipkowski and PN Ross, VCH Publishers, New York, 1994.
[32] M. Armand, P. Johansson, J. Power Sources, 178 (2008) 821-825.
[33] M. Armand, J.M. Tarascon, Nature, 451 (2008) 652.
[34] R.J. Brodd, K.R. Bullock, R.A. Leising, R.L. Middaugh, J.R. Miller, E. Takeuchi, J. Electrochem. Soc., 151 (2004) K1-K11.
[35] V. Augustyn, P. Simon, B. Dunn, Energy Environ. Sci., 7 (2014) 1597-1614.
[36] J.R. Miller, A.F. Burke, Electrochem. Soc. Interface., 17 (2008) 53.
[37] K. Smith, C.-Y. Wang, J. Power Sources, 160 (2006) 662-673.
[38] X. Zhang, A.M. Sastry, W. Shyy, J. Electrochem. Soc., 155 (2008) A542-A552.
[39] T. Zhang, N. Imanishi, Y. Shimonishi, A. Hirano, Y. Takeda, O. Yamamoto, N. Sammes, Chem. Commun., 46 (2010) 1661-1663.
[40] G. Girishkumar, B. McCloskey, A.C. Luntz, S. Swanson, W. Wilcke, The Journal of Physical Chemistry Letters, 1 (2010) 2193-2203.
[41] B. Kumar, J. Kumar, R. Leese, J.P. Fellner, S.J. Rodrigues, K.M. Abraham, J. Electrochem. Soc., 157 (2010) A50-A54.

[42] H.-G. Jung, J. Hassoun, J.-B. Park, Y.-K. Sun, B. Scrosati, Nature Chemistry, 4 (2012) 579.
[43] T. Zhang, H. Zhou, Nat. Commun., 4 (2013) 1817.
[44] C.O. Laoire, S. Mukerjee, K.M. Abraham, E.J. Plichta, M.A. Hendrickson, J. Phys. Chem. C, 113 (2009) 20127-20134.
[45] Y. Wang, H. Zhou, J. Power Sources, 195 (2010) 358-361.
[46] P. Sharma, T.S. Bhatti, Energy Conversion and Management, 51 (2010) 2901-2912.
[47] D. Chunsheng, Y. Jeff, P. Ning, Nanotechnology, 16 (2005) 350.
[48] M.M.J. Treacy, T.W. Ebbesen, J.M. Gibson, Nature, 381 (1996) 678.
[49] L.L. Zhang, X.S. Zhao, Chem. Soc. Rev., 38 (2009) 2520-2531.
[50] Q. Ke, J. Wang, J. Materiomics, 2 (2016) 37-54.
[51] N.-S. Choi, Z. Chen, S.A. Freunberger, X. Ji, Y.-K. Sun, K. Amine, G. Yushin, L.F. Nazar, J. Cho, P.G. Bruce, Angew. Chem. Int. Ed., 51 (2012) 9994-10024.
[52] T. Morimoto, K. Hiratsuka, Y. Sanada, K. Kurihara, J. Power Sources, 60 (1996) 239-247.
[53] S. Yoon, J. Lee, T. Hyeon, S.M. Oh, J. Electrochem. Soc., 147 (2000) 2507-2512.
[54] Q. Lu, J.G. Chen, J.Q. Xiao, Angew. Chem. Int. Ed., 52 (2013) 1882-1889.
[55] L. Huang, D. Chen, Y. Ding, S. Feng, Z.L. Wang, M. Liu, Nano Lett., 13 (2013) 3135-3139.
[56] L. Yang, S. Cheng, Y. Ding, X. Zhu, Z.L. Wang, M. Liu, Nano Lett., 12 (2012) 321-325.
[57] C. Yuan, H.B. Wu, Y. Xie, X.W. Lou, Angew. Chem. Int. Ed., 53 (2014) 1488-1504.
[58] X. Lang, A. Hirata, T. Fujita, M. Chen, Nat. Nanotechnol., 6 (2011) 232.
[59] A. Yuan, Q. Zhang, Electrochem. Commun., 8 (2006) 1173-1178.
[60] M. Kim, F. Xu, J.H. Lee, C. Jung, S.M. Hong, Q.M. Zhang, C.M. Koo, J. Mater. Chem. A, 2 (2014) 10029-10033.
[61] H.I. Becker, in, Google Patents, US Patent, 1957.
[62] D.L. Boos, in, Google Patents, US Patent, 1970.
[63] B.E. Conway, J. Electrochem. Soc., 138 (1991) 1539-1548.
[64] M. Vangari, T. Pryor, L. Jiang, J. Energy Eng., 139 (2012) 72-79.
[65] H.V. Helmholtz, Ann. Phys., 243 (1879) 337-382.
[66] L.L. Zhang, X.S. Zhao, Chemical Society Reviews, 38 (2009) 2520-2531.

[67] H. Du, X. Lin, Z. Xu, D. Chu, J. Mater. Sci., 50 (2015) 5641-5673.
[68] R. Burt, G. Birkett, X.S. Zhao, Phys. Chem. Chem. Phys., 16 (2014) 6519-6538.
[69] X. Du, P. Guo, H. Song, X. Chen, Electrochim. Acta, 55 (2010) 4812-4819.
[70] S.T. Senthilkumar, R.K. Selvan, Y.S. Lee, J.S. Melo, J. Mater. Chem. A, 1 (2013) 1086-1095.
[71] A.B. Fuertes, F. Pico, J.M. Rojo, J. Power Sources, 133 (2004) 329-336.
[72] M. Zhi, C. Xiang, J. Li, M. Li, N. Wu, Nanoscale, 5 (2013) 72-88.
[73] W.G. Pell, B.E. Conway, W.A. Adams, J. de Oliveira, J. Power Sources, 80 (1999) 134-141.
[74] S. Trasatti, G. Buzzanca, J. Electroanal. Chem. Interfacial Electrochem., 29 (1971) A1-A5.
[75] J.P. Zheng, P.J. Cygan, T.R. Jow, J. Electrochem. Soc., 142 (1995) 2699-2703.
[76] S.-M. Chen, R. Ramachandran, V. Mani, R. Saraswathi, Int. J. Electrochem. Sci, 9 (2014) 4072-4085.
[77] B.-O. Park, C.D. Lokhande, H.-S. Park, K.-D. Jung, O.-S. Joo, J. Power Sources, 134 (2004) 148-152.
[78] M. Mahmoud, F.E.-K. Maher, Z. Zhiheng, M. Peter, M. Jun, Nanotechnology, 27 (2016) 442001.
[79] C.-C. Hu, C.-C. Wang, Electrochem. Commun., 4 (2002) 554-559.
[80] B.-O. Park, C.D. Lokhande, H.-S. Park, K.-D. Jung, O.-S. Joo, Journal of Power Sources, 134 (2004) 148-152.
[81] B.E. Conway, Electrochemical supercapacitors: scientific fundamentals and technological applications, Springer Science & Business Media, 2013.
[82] E. Herrero, L.J. Buller, H.D. Abruña, Chem. Rev., 101 (2001) 1897-1930.
[83] B.E. Conway, Electrochim. Acta, 38 (1993) 1249-1258.
[84] P.V. Braun, J. Cho, J.H. Pikul, W.P. King, H. Zhang, Curr. Opin. Solid State Mater. Sci., 16 (2012) 186-198.
[85] T. Brousse, D. Bélanger, J.W. Long, J. Electrochem. Soc., 162 (2015) A5185-A5189.
[86] J. Wang, J. Polleux, J. Lim, B. Dunn, J. Phys. Chem. C, 111 (2007) 14925-14931.
[87] R.A. Fisher, M.R. Watt, W. Jud Ready, ECS J. Solid State Sci. Technol., 2 (2013) M3170-M3177.
[88] T.C. Liu, W.G. Pell, B.E. Conway, S.L. Roberson, J. Electrochem. Soc., 145 (1998) 1882-1888.

[89] T. Brezesinski, J. Wang, S.H. Tolbert, B. Dunn, Nat. Mater., 9 (2010) 146.
[90] M. Sathiya, A.S. Prakash, K. Ramesha, J.M. Tarascon, A.K. Shukla, J. Am. Chem. Soc., 133 (2011) 16291-16299.
[91] T. Brezesinski, J. Wang, J. Polleux, B. Dunn, S.H. Tolbert, J. Am. Chem. Soc., 131 (2009) 1802-1809.
[92] J. Wang, J. Polleux, J. Lim, B. Dunn, The Journal of Physical Chemistry C, 111 (2007) 14925-14931.
[93] M. Mastragostino, C. Arbizzani, F. Soavi, Solid State Ionics, 148 (2002) 493-498.
[94] H. Wang, Q. Gao, L. Jiang, Small, 7 (2011) 2454-2459.
[95] Y. Huang, J. Liang, Y. Chen, Small, 8 (2012) 1805-1834.
[96] Y. Zhang, H. Feng, X. Wu, L. Wang, A. Zhang, T. Xia, H. Dong, X. Li, L. Zhang, International Journal of Hydrogen Energy, 34 (2009) 4889-4899.
[97] J. Gamby, P.L. Taberna, P. Simon, J.F. Fauvarque, M. Chesneau, J. Power Sources, 101 (2001) 109-116.
[98] X. Du, C. Wang, M. Chen, Y. Jiao, J. Wang, J. Phys. Chem. C, 113 (2009) 2643-2646.
[99] W. Gao, N. Singh, L. Song, Z. Liu, A.L.M. Reddy, L. Ci, R. Vajtai, Q. Zhang, B. Wei, P.M. Ajayan, Nat. Nanotechnol., 6 (2011) 496.
[100] J. Ji, L.L. Zhang, H. Ji, Y. Li, X. Zhao, X. Bai, X. Fan, F. Zhang, R.S. Ruoff, ACS Nano, 7 (2013) 6237-6243.
[101] C. Kim, B.T.N. Ngoc, K.S. Yang, M. Kojima, Y.A. Kim, Y.J. Kim, M. Endo, S.C. Yang, Adv. Mater., 19 (2007) 2341-2346.
[102] L.-F. Chen, X.-D. Zhang, H.-W. Liang, M. Kong, Q.-F. Guan, P. Chen, Z.-Y. Wu, S.-H. Yu, ACS Nano, 6 (2012) 7092-7102.
[103] J. Li, X. Wang, Q. Huang, S. Gamboa, P.J. Sebastian, J. Power Sources, 158 (2006) 784-788.
[104] R. Saliger, U. Fischer, C. Herta, J. Fricke, J. Non-Cryst. Solids, 225 (1998) 81-85.
[105] D.N. Futaba, K. Hata, T. Yamada, T. Hiraoka, Y. Hayamizu, Y. Kakudate, O. Tanaike, H. Hatori, M. Yumura, S. Iijima, Nat. Mater., 5 (2006) 987.
[106] H. Pan, J. Li, Y. Feng, Nanoscale Res. Lett., 5 (2010) 654.
[107] M. Endo, T. Maeda, T. Takeda, Y.J. Kim, K. Koshiba, H. Hara, M.S. Dresselhaus, J. Electrochem. Soc., 148 (2001) A910-A914.
[108] D. Qu, H. Shi, J. Power Sources, 74 (1998) 99-107.

[109] E. Raymundo-Piñero, K. Kierzek, J. Machnikowski, F. Béguin, Carbon, 44 (2006) 2498-2507.
[110] J. Jiang, L. Zhang, X. Wang, N. Holm, K. Rajagopalan, F. Chen, S. Ma, Electrochim. Acta, 113 (2013) 481-489.
[111] A. Thambidurai, J.K. Lourdusamy, J.V. John, S. Ganesan, Korean J. Chem. Eng., 31 (2014) 268-275.
[112] J. Wu, W. Pisula, K. Müllen, Chem. Rev., 107 (2007) 718-747.
[113] C. Niu, E.K. Sichel, R. Hoch, D. Moy, H. Tennent, Appl. Phys. Lett., 70 (1997) 1480-1482.
[114] K.H. An, W.S. Kim, Y.S. Park, J.-M. Moon, D.J. Bae, S.C. Lim, Y.S. Lee, Y.H. Lee, Adv. Funct. Mater., 11 (2001) 387-392.
[115] C. Lee, X. Wei, J.W. Kysar, J. Hone, Science, 321 (2008) 385.
[116] J. Xia, F. Chen, J. Li, N. Tao, Nat. Nanotechnol., 4 (2009) 505.
[117] T.J. Booth, P. Blake, R.R. Nair, D. Jiang, E.W. Hill, U. Bangert, A. Bleloch, M. Gass, K.S. Novoselov, M.I. Katsnelson, A.K. Geim, Nano Lett., 8 (2008) 2442-2446.
[118] D.-W. Wang, F. Li, J. Zhao, W. Ren, Z.-G. Chen, J. Tan, Z.-S. Wu, I. Gentle, G.Q. Lu, H.-M. Cheng, ACS Nano, 3 (2009) 1745-1752.
[119] J. Yan, Z. Fan, T. Wei, W. Qian, M. Zhang, F. Wei, Carbon, 48 (2010) 3825-3833.
[120] S. Wang, L. Ma, M. Gan, S. Fu, W. Dai, T. Zhou, X. Sun, H. Wang, H. Wang, J. Power Sources, 299 (2015) 347-355.
[121] B. Xu, F. Wu, R. Chen, G. Cao, S. Chen, Z. Zhou, Y. Yang, Electrochem. Commun., 10 (2008) 795-797.
[122] P. Simon, Y. Gogotsi, Nat. Mater., 7 (2008) 845.
[123] G.A. Snook, P. Kao, A.S. Best, Journal of Power Sources, 196 (2011) 1-12.
[124] J.-H. Kim, Y.-S. Lee, A.K. Sharma, C.G. Liu, Electrochim. Acta, 52 (2006) 1727-1732.
[125] R.K. Sharma, A.C. Rastogi, S.B. Desu, Electrochem. Commun., 10 (2008) 268-272.
[126] K. Wang, J. Huang, Z. Wei, J. Phys. Chem. C, 114 (2010) 8062-8067.
[127] K.-H. Chang, C.-C. Hu, Appl. Phys. Lett., 88 (2006) 193102.
[128] C.-C. Hu, K.-H. Chang, M.-C. Lin, Y.-T. Wu, Nano Lett., 6 (2006) 2690-2695.
[129] J. Zang, S.-J. Bao, C.M. Li, H. Bian, X. Cui, Q. Bao, C.Q. Sun, J. Guo, K. Lian, J. Phys. Chem. C, 112 (2008) 14843-14847.

[130] H. Xia, Y.S. Meng, G. Yuan, C. Cui, L. Lu, Electrochem. Solid-State Lett., 15 (2012) A60-A63.
[131] W. Wang, S. Guo, I. Lee, K. Ahmed, J. Zhong, Z. Favors, F. Zaera, M. Ozkan, C.S. Ozkan, Sci. Rep., 4 (2014) 4452.
[132] S. Yan, H. Wang, P. Qu, Y. Zhang, Z. Xiao, Synth. Met., 159 (2009) 158-161.
[133] X. Liu, T.A. Huber, M.C. Kopac, P.G. Pickup, Electrochim. Acta, 54 (2009) 7141-7147.
[134] M.S. Dandekar, G. Arabale, K. Vijayamohanan, J. Power Sources, 141 (2005) 198-203.
[135] R.Y. Song, J.H. Park, S.R. Sivakkumar, S.H. Kim, J.M. Ko, D.-Y. Park, S.M. Jo, D.Y. Kim, J. Power Sources, 166 (2007) 297-301.
[136] Y.-T. Wang, A.-H. Lu, H.-L. Zhang, W.-C. Li, J. Phys. Chem. C, 115 (2011) 5413-5421.
[137] M.-S. Song, K.M. Lee, Y.R. Lee, I.Y. Kim, T.W. Kim, J.L. Gunjakar, S.-J. Hwang, J. Phys. Chem. C, 114 (2010) 22134-22140.
[138] M. Vangari, T. Pryor, L. Jiang, J. Energy Eng., 139 (2013) 72-79.
[139] A. Malak-Polaczyk, C. Matei-Ghimbeu, C. Vix-Guterl, E. Frackowiak, J. Solid State Chem., 183 (2010) 969-974.
[140] R. Amade, E. Jover, B. Caglar, T. Mutlu, E. Bertran, J. Power Sources, 196 (2011) 5779-5783.
[141] S.G. Kandalkar, D.S. Dhawale, C.-K. Kim, C.D. Lokhande, Synth. Met., 160 (2010) 1299-1302.
[142] V. Gupta, T. Kawaguchi, N. Miura, Mater. Res. Bull., 44 (2009) 202-206.
[143] R.S. Jayashree, P. Vishnu Kamath, J. Appl. Electrochem., 31 (2001) 1315-1320.
[144] M.-S. Wu, Y.-A. Huang, J.-J. Jow, W.-D. Yang, C.-Y. Hsieh, H.-M. Tsai, Int. J. Hydrogen Energy, 33 (2008) 2921-2926.
[145] E.B. Castro, S.G. Real, L.F. Pinheiro Dick, Int. J. Hydrogen Energy, 29 (2004) 255-261.
[146] U.M. Patil, R.R. Salunkhe, K.V. Gurav, C.D. Lokhande, Appl. Surf. Sci., 255 (2008) 2603-2607.
[147] K.C. Liu, M.A. Anderson, J. Electrochem. Soc., 143 (1996) 124-130.
[148] J. Cheng, G.-P. Cao, Y.-S. Yang, J. Power Sources, 159 (2006) 734-741.
[149] H. Chen, J. Jiang, L. Zhang, T. Qi, D. Xia, H. Wan, J. Power Sources, 248 (2014) 28-36.

[150] J.W. Lee, A.S. Hall, J.-D. Kim, T.E. Mallouk, Chem. Mater., 24 (2012) 1158-1164.
[151] Z. Ma, X. Huang, S. Dou, J. Wu, S. Wang, J. Phys. Chem. C, 118 (2014) 17231-17239.
[152] Q. Guan, J. Cheng, B. Wang, W. Ni, G. Gu, X. Li, L. Huang, G. Yang, F. Nie, ACS Appl. Mater. Interfaces, 6 (2014) 7626-7632.
[153] W. Zhang, B. Quan, C. Lee, S.-K. Park, X. Li, E. Choi, G. Diao, Y. Piao, ACS Appl. Mater. Interfaces, 7 (2015) 2404-2414.
[154] S.-L. Kuo, J.-F. Lee, N.-L. Wu, J. Electrochem. Soc., 154 (2007) A34-A38.
[155] Z. Wu, Y. Zhu, X. Ji, J. Mater. Chem. A, 2 (2014) 14759-14772.
[156] Y. Chen, B. Qu, L. Hu, Z. Xu, Q. Li, T. Wang, Nanoscale, 5 (2013) 9812-9820.
[157] T.-Y. Wei, C.-H. Chen, H.-C. Chien, S.-Y. Lu, C.-C. Hu, Adv. Mater., 22 (2010) 347-351.
[158] X. Liu, S. Shi, Q. Xiong, L. Li, Y. Zhang, H. Tang, C. Gu, X. Wang, J. Tu, ACS Appl. Mater. Interfaces, 5 (2013) 8790-8795.
[159] Y. Li, P. Hasin, Y. Wu, Adv. Mater., 22 (2010) 1926-1929.
[160] P. Rasiyah, A.C.C. Tseung, D.B. Hibbert, J. Electrochem. Soc., 129 (1982) 1724-1727.
[161] G. Wang, L. Zhang, J. Zhang, Chemical Society Reviews, 41 (2012) 797-828.
[162] C. Yuan, J. Li, L. Hou, J. Lin, X. Zhang, S. Xiong, J. Mater. Chem. A, 1 (2013) 11145-11151.
[163] N. Padmanathan, S. Selladurai, RSC Adv., 4 (2014) 8341-8349.
[164] M. Grätzel, Nat. Mater., 13 (2014) 838.
[165] E. Fabbri, D. Pergolesi, E. Traversa, Chem. Soc. Rev., 39 (2010) 4355-4369.
[166] H. Iwahara, T. Yajima, T. Hibino, H. Ushida, J. Electrochem. Soc., 140 (1993) 1687-1691.
[167] N. Bonanos, K.S. Knight, B. Ellis, Solid State Ionics, 79 (1995) 161-170.
[168] H. Uchida, N. Maeda, H. Iwahara, Solid State Ionics, 11 (1983) 117-124.
[169] H. Iwahara, T. Yajima, H. Ushida, Solid State Ionics, 70-71 (1994) 267-271.
[170] A.F. Sammells, R.L. Cook, J.H. White, J.J. Osborne, R.C. MacDuff, Solid State Ionics, 52 (1992) 111-123.
[171] S. Vasala, M. Karppinen, Prog. Solid State Chem., 43 (2015) 1-36.
[172] T. Kudo, H. Obayashi, T. Gejo, J. Electrochem. Soc., 122 (1975) 159-163.

[173] W.R. McKinnon, M.L. Post, L.S. Selwyn, G. Pleizier, J.M. Tarascon, P. Barboux, L.H. Greene, G.W. Hull, Phys. Rev. B, 38 (1988) 6543-6551.
[174] E. Goldberg, A. Nemudry, V. Boldyrev, R. Schöllhorn, Solid State Ionics, 122 (1999) 17-22.
[175] A. Nemudry, E.L. Goldberg, M. Aguirre, M.Á. Alario-Franco, Solid State Sci., 4 (2002) 677-690.
[176] E. Goldberg, A. Nemudry, V. Boldyrev, R. Schöllhorn, Solid State Ionics, 110 (1998) 223-233.
[177] L. Karvonen, M. Valkeapää, R.-S. Liu, J.-M. Chen, H. Yamauchi, M. Karppinen, Chem. Mater., 22 (2010) 70-76.
[178] J.T. Mefford, W.G. Hardin, S. Dai, K.P. Johnston, K.J. Stevenson, Nat. Mater., 13 (2014) 726.
[179] L. Zhu, Y. Liu, C. Su, W. Zhou, M. Liu, Z. Shao, Angew. Chem. Int. Ed., 55 (2016) 9576-9579.
[180] Q. Deng, X. Li, J. Zuo, A. Ling, B.E. Logan, J. Power Sources, 195 (2010) 1130-1135.
[181] E. Martin, B. Tartakovsky, O. Savadogo, Electrochim. Acta, 58 (2011) 58-66.
[182] S.Y. Sawant, R.S. Somani, M.H. Cho, H.C. Bajaj, RSC Adv., 5 (2015) 46589-46597.
[183] S.Y. Sawant, R.S. Somani, S.S. Sharma, H.C. Bajaj, Carbon, 68 (2014) 210-220.
[184] A. ElMekawy, H.M. Hegab, D. Losic, C.P. Saint, D. Pant, Renewable Sustainable Energy Rev., 72 (2017) 1389-1403.
[185] L. Xiao, J. Damien, J. Luo, H.D. Jang, J. Huang, Z. He, J. Power Sources, 208 (2012) 187-192.
[186] R. Kou, Y. Shao, D. Wang, M.H. Engelhard, J.H. Kwak, J. Wang, V.V. Viswanathan, C. Wang, Y. Lin, Y. Wang, I.A. Aksay, J. Liu, Electrochem. Commun., 11 (2009) 954-957.
[187] Y. Ren, D. Pan, X. Li, F. Fu, Y. Zhao, X. Wang, J. Chem. Technol. Biotechnol., 88 (2013) 1946-1950.
[188] G. Wu, N.H. Mack, W. Gao, S. Ma, R. Zhong, J. Han, J.K. Baldwin, P. Zelenay, ACS Nano, 6 (2012) 9764-9776.

Every reasonable effort has been made to acknowledge the owners of copyright material. I would be pleased to hear from any copyright owner who has been omitted or incorrectly acknowledged.

Chapter 3 Design of perovskite oxides as anion-intercalation type electrodes for supercapacitors: cation leaching effect[§]

Abstract

Oxygen ions can be exploited as a charge carrier to effectively realize a new type of anion-intercalation supercapacitors. In this study, to get some useful guidelines for future materials development, we comparatively studied $SrCoO_{3-\delta}$ (SC), $Ba_{0.5}Sr_{0.5}Co_{0.8}Fe_{0.2}O_{3-\delta}$ (BSCF) and Co_3O_4 as electrodes in supercapacitors with aqueous alkaline electrolyte. The effect of interaction between the electrode materials with the alkaline solution was focused on the structure and specific surface area of the electrode material, and ultimately the electrochemical performance was emphasized. Both BSCF and SC were found to experience cation leaching in alkaline solution, resulting to an increase in the specific surface area of the material, but over leaching caused the damage of perovskite structure of BSCF. Barium leaching was more serious than strontium, and the cation leaching was component dependent. Although high initial capacitance was achieved for BSCF, it was not a good candidate as intercalation-type electrode for supercapacitor because of poor cycling stability from serious Ba^{2+} and Sr^{2+} leaching. Instead, SC was a favourable electrode candidate for practical use in supercapacitors due to its high capacity and proper cation leaching capacity, which brought beneficial effect on cycling stability. It is suggested that cation leaching effect should be seriously concerned in the development of new perovskite materials as electrodes for supercapacitors.

3.1 Introduction

The fast growth of global population and the heavy industrialization of human civilization have induced a great pressure on the environment and have also brought forward a serious concern about energy crisis. It is of great importance that continuous innovation should be made by energy technologies specifically the generation, storage and delivery in order to meet worldwide challenges for a sustainable supply of inexpensive and clean energy.[1-3] The combination of abundant renewable energies (such as solar energy and bio fuels) and versatile electrochemical storage devices and energy conversion technologies such as lithium-ion batteries, supercapacitor and fuel cells may provide an ideal energy system for the future.[4-9]

As an important type of electrochemical energy storage devices, supercapacitors, also named as electrochemical capacitors, have gathered worldwide attention due to the high power density in comparison to traditional capacitors and superiorly long cycle life (> 100,000 cycles) in comparison to lithium ion batteries, and have been successfully applied in several important fields, such as in electric vehicles where supercapacitors have been successfully used as main and accessory power.[10, 11] Based on specific charge storage mechanisms, there are two general categories of supercapacitors, i.e., electric double-layer capacitors (EDLCs), which rely on carbon based materials with high specific surface area, and the pseudocapacitors which store energy through Faradaic reactions over the surface or subsurface of conducting polymers and metal oxides.[12-14] For both categories of supercapacitors, an increase in specific surface area will facilitate the energy storage since the electric double-layer capacitance and surface pseudocapacitance both mainly involve the surface reactions. Thus, maximizing the specific surface area is the main research effort for such kind of electrode materials.[15] Lately, a new type of supercapacitors based on ion-intercalation reaction has been proposed.[16-20] The electrode reactions in the intercalation-type supercapacitors are similar to those in the intercalation-type electrodes in lithium-ion batteries (LIB), but typically no phase transition is involved for the former during the electrode reaction.[21] In addition to the surface properties, the bulk properties also play an important role in the energy storage of such intercalation-type electrodes.

Lithium ion is the main charge carrier for intercalation-type electrodes of supercapacitors.[16-20] At 2014, Mefford and co-workers reported that oxygen anion

can intercalate into perovskite type $LaMnO_{3\pm\delta}$ oxide with the development of a new anion-intercalation type supercapacitor.[22] it is surprising since the mobility of O^{2-} was considered to be much lower than Li^{+} due to the much larger ionic size of O^{2-}. Actually, our recent experimental results demonstrated outstanding rate capability of perovskite $SrNb_{0.1}Co_{0.9}O_{3-\delta}$ perovskite electrode with a capacity retention of > 92% was obtained when the discharge rate was increased from 0.1 to 10 A g^{-1}; in addition, the bulk diffusion was so fast that the surface reaction even became the primary limiting step for energy storage at relatively low charge/discharge rate.[23]

Since the oxygen vacancy concentration as well as the oxygen diffusion rate of a perovskite oxide is highly dependent on its structure and composition, a well-designed perovskite material is critical to achieve a high electrode performance.[24-26] On the other hand, it was well demonstrated that the environmental impurity and operation conditions possibly will have a substantial impact on the performance and operational stability of perovskite oxide as the oxygen reduction electrode of solid oxide fuel cells (SOFCs).[27-29] It should also be a big concern for the perovskite-type supercapacitor electrodes. As the anion-intercalation type electrode of supercapacitors, the perovskite material is immersed in a high concentration of alkaline solution (KOH or NaOH). The potential reaction/chemical interaction between the solid perovskite and the liquid electrolyte may affect the bulk phase structure, bulk composition, defect concentration or surface composition of the perovskite oxide, thus altering the bulk diffusion and/or surface reaction properties, and consequently changing the charge/discharge performance of the electrode. However, up to know, little knowledge about such reaction/interaction is available in the literature.

Herein, we specifically investigated the potential use of $SrCoO_{3-\delta}$ (SC), a parent oxide with high oxygen vacancy concentration for many perovskite oxides with highly diversified properties, and $Ba_{0.5}Sr_{0.5}Co_{0.8}Fe_{0.2}O_{3-\delta}$ (BSCF), a popular perovskite material with ultrahigh oxygen vacancy concentration and oxygen diffusivity, as anion-intercalation type electrodes of supercapacitor. Co_3O_4, a typical Faradic type electrode material for supercapacitors, was also investigated for comparison purpose. Importance was paid to the interaction/reaction between the electrode materials and the alkaline solution and its effect on the electrode performance, including capacity and cycling stability. Selective leaching of certain compositional element(s) from the perovskite oxides into the alkaline aqueous solution under the supercapacitor's

operation condition was observed, which could cause a change in the specific surface area in addition to the phase structure of the perovskite materials, resulting in an increase or decrease in capacity of the electrode that depended on the degree of the dissolution. The knowledge obtained in this study could provide a valuable guideline for the further progression of high-performance and stable perovskite-type anion intercalation electrode materials for supercapacitors.

3.2. Experimental section

Material Synthesis: An EDTA-citrate complexing (EDTA-CA) method was adopted for synthesis of BSCF, SC and Co_3O_4 oxide powders in this study.[30] The procedure for the synthesis of SC, as a model, is defined as follows. $Sr(NO_3)_2$ and $Co(NO_3)_2{\cdot}6H_2O$, commercially purchased from Sigma-Aldrich Pty. Ltd, were transferred into a mixed aqueous solution under magnetic stirring for 30 min at 80 ^oC in air. Once a clear solution was obtained, EDTA and CA were transferred into the above solution and serve as complexing agents at molar ratio of 1:1:2 for metal ions : EDTA : CA. During the heating for water evaporation, $NH_3{\cdot}H_2O$ was used to regulate the pH value of the mixture to approximately 7 to avoid the appearance of precipitation. A transparent gel was achieved after heating at 150 ^oC with continuous stirring, which was then heated at 250 ^oC to form a solid precursor, and further calcined at 1000 ^oC for 5 h in air to obtain the desired composite oxide. A final calcination temperature of 950 ^oC and 900 ^oC was chosen for BSCF and Co_3O_4, to create similar specific surface area of the three samples.

Material Characterization: The phase structures were analysed via X-ray powder diffraction at room temperature by means of an X-ray diffractometer (Model D8 Advance, Bruker, Germany) through filtered Cu Kα radiation (λ = 1.5418 Å). Step scanning in the 2θ range of 10–90^o with intervals of 0.02^o were used to collect diffraction patterns. Microstructure and elemental analysis were conducted via scanning electron microscope (SEM, Zeiss Neon 40EsB). X-ray photoelectron spectroscopy (XPS) was used with a Kratos AXIS Ultra DLD system with monochromated Al-Kα X-rays (1486.7 eV) under ultra-high vacuum conditions (<1 × 10^{-9} mbar). Patterns were analysed by CasaXPS software and calibrated to yield a primary C 1s component at 284.5 eV. The N_2 adsorption-desorption analysis was performed at a temperature of -196 ^oC using a Micromeritics Tristar 3000 instrument.

The Brunauere-Emmette-Teller (BET) method applied in calculation of specific surface areas of the samples. The samples were de-gased at 200 ^{o}C for 12 h under vacuum condition before analysis.

Electrochemical Performance Test: The electrochemical performance of the synthesized samples were tested by cyclic voltammograms (CV), which were analysed with CHI 660A electrochemical workstation (CH instruments Inc., USA) using a three electrode arrangement. The galvanostatic charge and discharge (GCD) tests were carried out on a NEWARE battery tester (Shenzhen, China) and galvanostat was controlled by computer in the same system. The working electrodes were made using the following steps. Firstly, 80 wt.% of active material in powder form was mixed with 10 wt.% of Super P conductive and 10 wt.% of PVDF (polyvinylidene fluoride) in a beaker with absolute ethanol solution and agitated with ultra-sonication for 2 h in order to achieve homogeneous dispersion. After that, the prepared colloid was dehydrated in a vacuum oven at 70 ^{o}C for 24 h to obtain the anticipated mixture and that was further fabricated to a film, which was pressed between two layers of nickel foam to form the electrode. The working electrode was soaked in the electrolyte solution for 12 h before testing to allow sufficient saturating of the electrode with the liquid electrolyte. The three-electrode setup used a counter electrode which consists of a Pt plate, a reference electrode consisting of an Hg/HgO electrode filled with 1 M KOH and an aqueous electrolyte consisting of 6 M KOH solution. In addition, the two-electrode cell consisting of a positive electrode (SC) and a negative electrode (active carbon, AC) spaced apart by 0.5 cm was utilized to analyse the electrochemical performance of the asymmetric supercapacitor (ASC) cell in 6 M KOH electrolyte.

3.3 Results and discussion

3.3.1 Leaching phenomenon and its effect on the structure and specific surface area

Phase structure and specific surface area of perovskite-type oxygen ion-intercalation type electrodes are two most important parameters that affect their performance in supercapacitors. The phase structure could affect the oxygen ion diffusivity as well as variable oxygen vacancy concentration in a perovskite material, thus exerting an impact on their capacity and rate capability, as well as their cycling stability, in supercapacitors. Shown in **Figure 3.1** are the XRD patterns of the as-synthesized

BSCF, SC and Co_3O_4. For the Co_3O_4 sample, a spinel type structure was demonstrated based on the XRD patterns. For perovskite oxides, their detailed lattice symmetry was closely related with the tolerance factor, defined as $t=(R_A+R_O)/(R_B+R_O)$, where R_A and R_B were the ionic radii of the cations occupying the A and B site respectively, while R_O was the oxygen ionic radius.[31] The tolerance factor t should be equal to 1 for an ideal cubic structure.[32] For the SC samples, the diffraction peaks can be well indexed based on the hexagonal crystalline structure of $SrCoO_{2.5}$, according to the standard spectrum (JCPDS card no. 48-0875), which was created due to the serious distortion of standard perovskite structure from the large mismatch in size of the A and B site cations. The BSCF sample took on an oxygen vacancy-disordered cubic perovskite structure. Typically, cubic structure was preferred for oxygen anion diffusion because of its three-dimensional diffusion channels, which would benefit the rate capability of the electrode in supercapacitors. The co-doping of Ba and Fe in the A and B sites respectively of SC effectively stabilized the cubic structure.

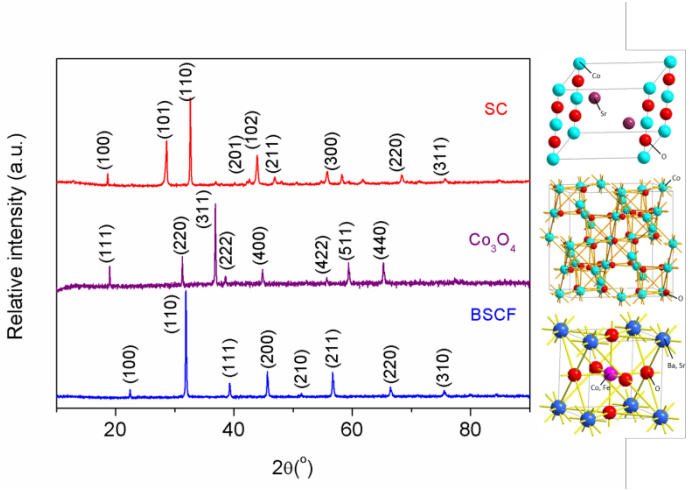

Figure 3.1 XRD patterns of the as-synthesized BSCF, SC and Co_3O_4 (left), and the diagram of the proposed structure (right), the Miller indexes on the top of XRD peaks of three samples were assigned based on cubic, hexagonal and cubic structure for BSCF, SC and Co_3O_4, respectively.

Table 3.1 The lattice volume and specific surface area of BSCF, SC and Co_3O_4 at different conditions

Materials	Crystal structure	Lattice volume (Å)	Specific surface area (m^2 g^{-1})		
			Fresh	KOH treated	Hydrothermal treated
BSCF	Cubic (Pm-3m)	63.28(7)	0.74(4)	2.88(8)	63.05(3)
SC	Hexagonal (P63-mmc)	120.03(5)	1.53(7)	3.88(9)	24.13(4)
Co_3O_4	Cubic (Fd-3m)	434.65(1)	1.04(2)	1.11(3)	1.78(2)

For pseudocapacitors, a high specific surface area of the electrode material is required in order to achieve high specific capacitance since the Faradaic reaction appeared at the electrode surface or subsurface.[33-35] As the anion-intercalation type electrodes, a high capacitance may be achieved for the materials with low specific surface area because the bulk of electrode will also be participated in the energy storage process. Anyway, the surface area may still have a big effect on the energy storage process, depending on the rate limiting step. SEM observation (**Figure 3.2a**) confirmed that all three samples had coarse particular morphology with large grain size of 2-15 μm and dense grain surface. The nitrogen adsorption desorption isotherms confirmed their specific surface areas under different conditions. Listed in the **Table 3.1** were the detailed structure parameters and the surface area of the three electrode materials. All of them showed low specific surface areas with the range of 0.7-1.6 m^2 g^{-1}.

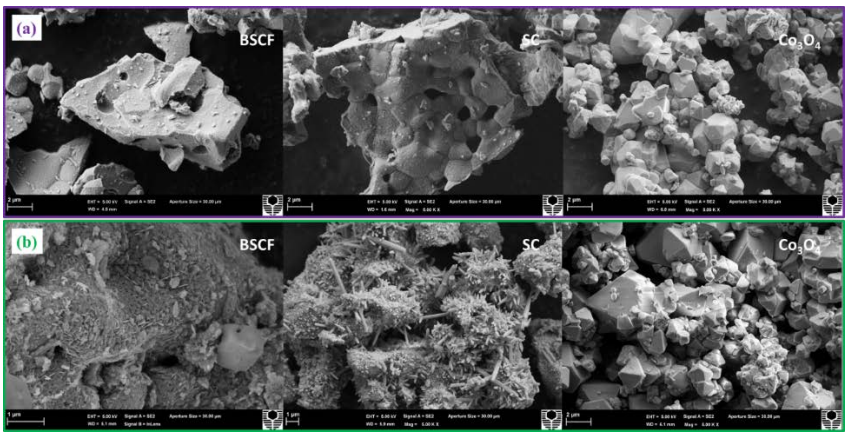

Figure 3.2 SEM micrograph of (a) fresh BSCF, SC and Co_3O_4 from EDTA-CA complexing method after the calcination at 950, 1000 and 900 ^oC for 6 h, respectively, and (b) these samples after the hydrothermal treatment.

Previously we demonstrated that the treatment of BSCF in an H_2O_2 solution at room temperature could result in a significant increase in the specific surface area due to the selective leaching of Ba^{2+} and Sr^{2+} (particularly, Ba^{2+}) into the H_2O_2 solution.[36] Therefore, the stability of the oxides in the alkaline solution was also a big concern; either a change in the specific surface area or the phase structure due to cation(s) leaching could affect the performance of the perovskite oxides as electrodes in supercapacitors. To examine the potential reaction/interaction of the three electrode materials with the alkaline solution, a small amount of above electrode materials were immersed in 6M KOH solution at room temperature under sealed atmosphere and treated for different periods, and then the samples after the treatment were characterized by phase structure, BET specific surface area, and particle morphology. Shown in **Figure 3.3** were the XRD patterns of BSCF, SC and Co_3O_4 after the treatment in 6M KOH solutions for different times of 8 - 72 h at room temperature. Little change in the diffraction patterns was observed for the Co_3O_4 sample after the treatment in KOH solution even for a prolonged period of 72 h, suggesting the good phase stability of spinel Co_3O_4 in alkaline solution. Interestingly, even a slight enhancement in the peaks intensity was observed for Co_3O_4 after the treatment as compared to the fresh one. It was likely that some surface amorphous phase in the fresh sample was dissolved by the alkaline solution during the treatment. Similar phenomenon was also observed for the SC oxide. For the BSCF sample, no obvious change in phase structure was observed after the treatment of the sample in KOH for 8 h; however, the perovskite structure was fully destroyed when the treatment time was prolonged to 36 h, and the sample became almost amorphous after the treatment in alkaline solution for a total period of 72 h. It indicates that BSCF was not stable under a strong alkaline solution. After the treatment for the same period of 8 h, the specific surface area of BSCF, SC and Co_3O_4 was found to be 2.89, 3.89 and 1.11 $m^2 g^{-1}$, respectively, while the corresponding values for the fresh samples were 0.74, 1.53 and 1.04 $m^2 g^{-1}$. It indicates the specific surface areas were increased by 3.9, 2.5 and 1.1 times for BSCF, SC and Co_3O_4, respectively. It was likely that the increased specific surface area of BSCF and SC samples, as well as the phase transition for BSCF after the treatment was also due to the leaching of Ba^{2+}/Sr^{2+} from BSCF and SC into the alkaline solution. To support this assumption, we further conducted hydrothermal treatment of BSCF, SC and Co_3O_4 in autoclave at 150 ^oC for 24 h to increase the intercalation between the oxides and water to accelerate the leaching of the cations.

During the treatment, 1 g of sample and 100 ml of water were applied. The Ba^{2+}, Sr^{2+}, Co^{x+} and Fe^{y+} cations in the mother solutions were then analysed by inductively coupled plasma-optical emission spectroscopy (ICP-OES). As shown in **Table 3.2**, high concentrations of Ba^{2+} of 27.3 mg L^{-1} and Sr^{2+} of 31.2 mg L^{-1} in the mother solution of BSCF were detected, while the Co^{x+} and Fe^{y+} concentrations (0.009 and 0.038 mg L^{-1}, respectively) were much lower. It confirms that the leaching of Ba^{2+}/Sr^{2+} was much more seriously than Co^{x+}/Fe^{y+}, while the leaching of Ba^{2+} was the most significant. The much lower concentration of Sr^{2+} (13.29 mg L^{-1}) in the mother solution of SC than that in the mother solution of BSCF (31.2 mg L^{-1}) implies the leaching of Sr^{2+} was also significantly affected by other components of perovskite oxides. The XRD patterns in the **Figure 3.3d** showed that the BSCF and SC samples lost their perovskite-type lattice structure after the treatment in autoclave at 150 ^{o}C, but the Co_3O_4 still kept the original spinel-type crystal structure. Shown in **Figure 3.2** were the SEM images of BSCF, SC and Co_3O_4 before and after the hydrothermal treatment. BSCF became porous after the treatment, and the particulate size of SC was significantly decreased, while the particular morphology of Co_3O_4 did not show a big change after the hydrothermal treatment compared with the fresh sample. Such different behaviours in morphological change for BSCF, SC and Co_3O_4 samples were clearly due to their different cation leaching capabilities. Actually, after the hydrothermal treatment, the BET specific surface area of BSCF increased to as large as 63.05 m^2 g^{-1}, and SC increased to 24.13 m^2 g^{-1}, while Co_3O_4 just increased slightly to 1.78 m^2 g^{-1}. The serious leaching of Ba^{2+}/Sr^{2+} contributed to the significant increase in specific surface area of BSCF and SC after the hydrothermal treatment.

Table 3.2 ICP-OES results of the mother solutions from the hydrothermal treatment of BSCF, SC and Co_3O_4 at 150 ^{o}C for 24 h, during the treatment, 1 g of sample and 100 ml of water were applied

Material	Ba (mg L^{-1})	Sr (mg L^{-1})	Co (mg L^{-1})	Fe (mg L^{-1})
BSCF	47.322	31.204	0.009	0.038
SC	n/a	13.287	0.051	n/a
Co_3O_4	n/a	n/a	0.078	n/a

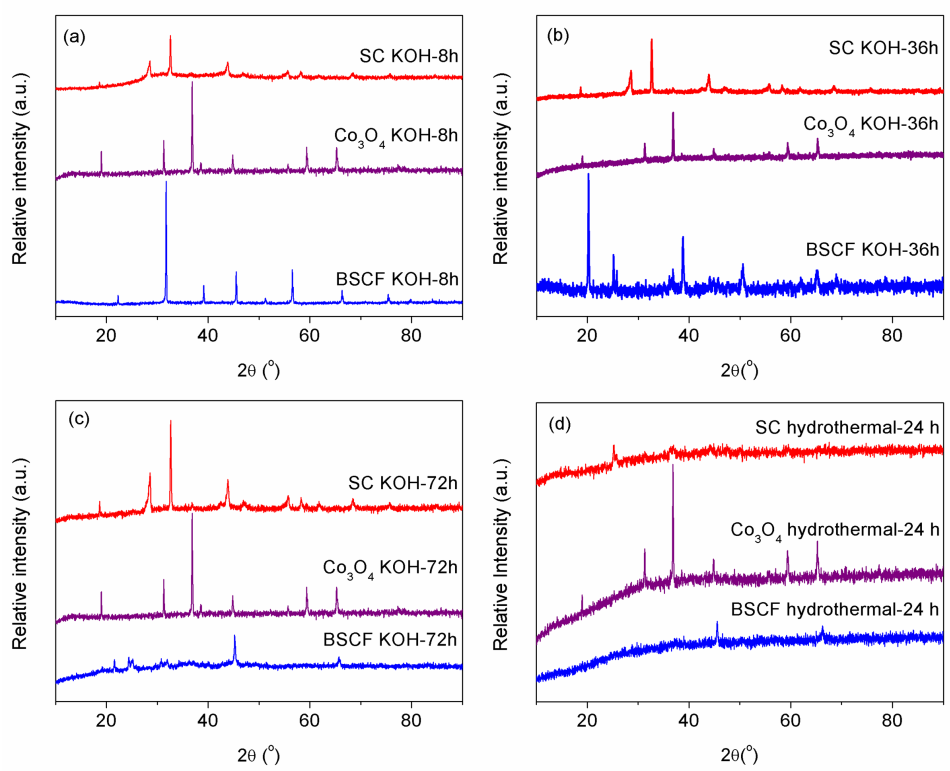

Figure 3.3 XRD patterns of BSCF, SC and Co_3O_4 after treatment in 6M KOH solution for (a) 8 h (b) 36 h and (c) 72 h. (d) XRD patterns of BSCF, SC and Co_3O_4 after treatment in autoclave at 150 ^oC.

3.3.2 Leaching effect on electrode of BSCF and SC in supercapacitor

The electrochemical performance of BSCF, SC and Co_3O_4 electrodes for supercapacitors were first comparatively investigated by GCDs (galvanostatic charge/discharge tests) at a fixed current rate of 1 A g^{-1} for 5000 cycles. As seen in **Figure 3.4**, for all three electrodes, an increase in capacitance in the initial cycles was observed. For example, Co_3O_4 showed an initial capacitance of around 200 F g^{-1}, and it increased to a peak value of around 270 F g^{-1} after cycling for about 100 times, then a slow decrease in the capacitance with the further cycling was observed. It was well known that Co_3O_4 was a Faradaic type supercapacitor electrode which stored energy through Faradaic redox reaction at the surface or subsurface of Co_3O_4.[37, 38] Because of the coarse-type Co_3O_4 used in this study, relatively poor capacitance was achieved. Here, the as-obtained capacitance was comparable to that achieved in literature for Co_3O_4 with similar specific surface area.[39] The modest increase in capacitance of Co_3O_4 during the initial around 100 cycles should be related with the surface activation,[40] which was supported by the increased crystallinity of the Co_3O_4 spinel

phase after the treatment in alkaline solution as demonstrated previously. For both BSCF and SC electrodes, much higher maximum capacitances than that of Co_3O_4 were observed, although all three electrodes had comparable specific surface area before the tests. The BSCF and SC electrodes showed a maximum capacitance of 610 F g^{-1} and 572 F g^{-1}, respectively, which was reached at 70th and 3000th cycles correspondingly. In oxygen-anion intercalation-type supercapacitor electrodes, the cumulative stored charge can be categorised into three mechanisms: the Faradaic contribution from the oxygen-anion insertion process, the Faradaic contribution from the charge-transfer process with surface atoms, and the non-faradaic contribution from the double layer effect.[41] As perovskite-type oxides, both BSCF and SC contain considerable amount of oxygen vacancies,[42, 43] which can be used for the intercalation of oxygen anion with the introduction of oxygen anion-intercalation energy storage mechanism. Since the low specific surface area of BSCF and SC, the contribution from the double layer effect should be negligible. On the other hand, because of their comparable specific surface areas, the much higher capacitance of BSCF/SC than that of Co_3O_4 should be attributed mainly from the Faradaic contribution from the oxygen anion insertion process in perovskite oxides.

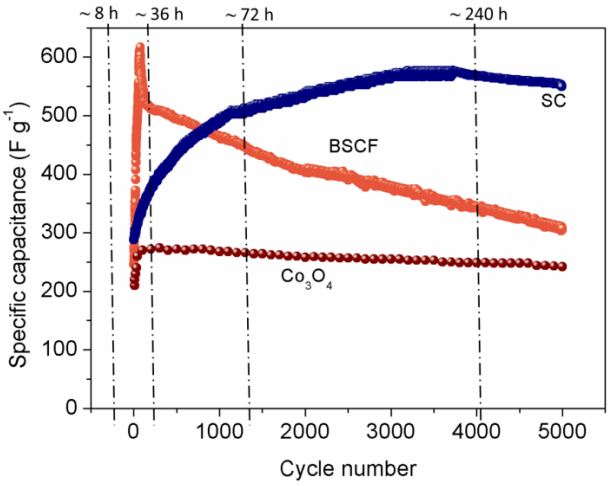

Figure 3.4. Cycling performance of BSCF, SC and Co_3O_4 at a current density of 1 A g^{-1} and the cycle number corresponding to cycle time.

To confirm the anion intercalation process of SC during the charge/discharge reaction, the electrochemical properties of the as-synthesized SC were analysed by CV measurements. Shown in **Figure 3.5** were the typical CVs of SC, which were performed at scanning rates of 5-500 mV s^{-1} in a potential window of 0.25 to 0.65 V.

it demonstrated a typical pseudo-capacitive behaviour of the oxide electrodes. According to these curves, there were an integrated oxidation peak and a reduction peak, which were related to the surface redox processes of $Co^{2+}/Co^{3+}/Co^{4+}$ occurring within the electroactive materials. All the CVs showed similar shape, and the positive shift in oxidation peak and negative shift in reduction peak correlated with increase of the scan rate, which is consistent with the electrodes internal resistance.[44] This indicated that SC electrode was in favour of fast redox reactions and possessed good reversibility. The charged and discharged SC electrode was then measured by XPS to get information about the oxidation state of cobalt with the typical spectrum shown in **Figure 3.6**. The Co2p signal was normally a distorted peak that resulted from complex state effects. In SC, the Co2p high resolution core-level spectrum showed two major peaks with binding energy of 779.8/784.4 eV ($2p_{3/2}$) and 794.7/800.5 eV ($2p_{1/2}$) for charged/discharged electrodes, with the spin-energy separation of 14.9/16.1 eV which was in agreement with the published data for Co^{3+}/Co^{2+}.[45, 46] By deconvoluting the Co2p spectrum in the charged SC, four resolved peaks and two weak shake-up Co^{3+} satellites peaks (789.6/804.6 eV) were obtained (**Figure 3.6a**).The peaks at 779.7 eV and 794.6 eV were similar to those reported for Co2p by O'Connell et al.,[47] which were attributed to Co^{3+} in the perovskite. The peaks appeared at 780.9 and 795.8 eV can be attributed to Co^{4+}, due to the electron density of Co^{4+} ion being higher than that of Co^{3+} ion. Co^{2+} can be overlooked as its satellite peaks normally appeared at a higher range. Furthermore, there were also two pairs of resolved peaks that were deconvoluted for the discharged Co2p spectrum (**Figure 3.6b**). The lower binding energy peaks at 783.9/799.9 eV belong to Co^{3+}, while the higher binding energy peaks at 789.7/805.7 eV could be ascribed to Co^{2+}. The resolved peaks in the charged/discharged samples may be ascribed to the Co^{x+}, which further identified the redox reaction between Co^{2+}, Co^{3+} and Co^{4+}. The relative concentrations of Co^{2+}, Co^{3+} and Co^{4+} calculated from the charged and discharged SC electrode were shown in the **Table 3.3**. Based on the difference in the oxidation state of cobalt in charged and discharged SC samples, the theoretical capacity based on oxygen anion intercalation mechanism can be calculated,[23] which was turned out to be 566 F g^{-1}, in good agreement with the measured value of about 572 F g^{-1} as reported previously. It thus strongly confirms the oxygen anion intercalation mechanism for energy storage in SC electrode in supercapacitor. The higher capacitance of BSCF than SC indicated that

the development of oxygen vacancy-disordered cubic structure benefited the oxygen-anion intercalation in perovskite oxides.

Table 3.3 The relative concentration of different Co species on the surface of material from the results of XPS.

Electrodes	Co^{2+}	Co^{3+}	Co^{4+}
Charged SC	n/a	67.14%	32.86%
Discharged SC	21.32%	78.68%	n/a

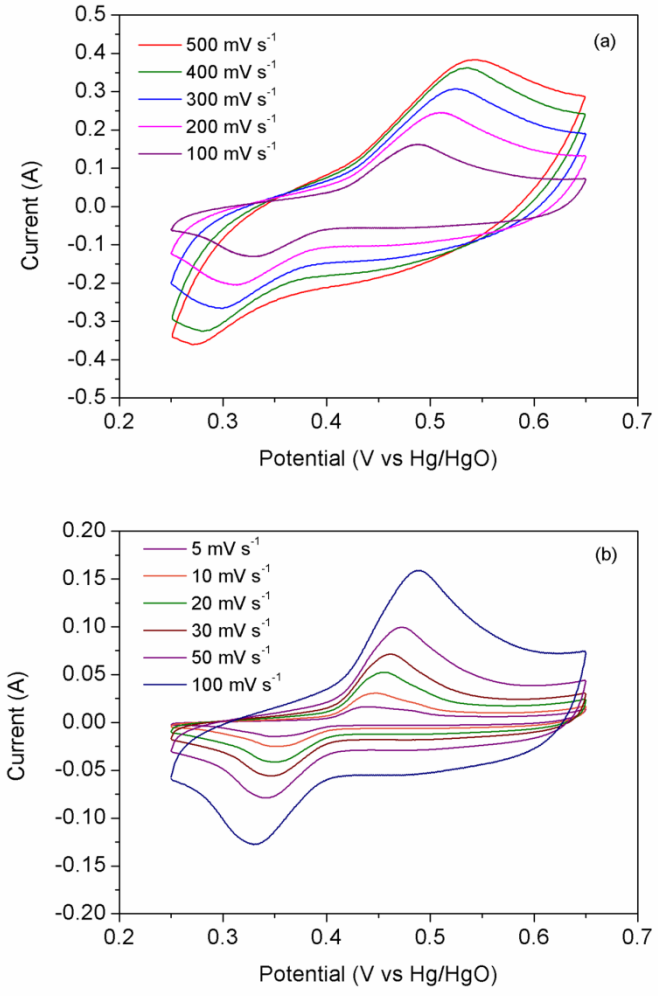

Figure 3.5 CV curves of SC electrode at various scan rates ranging (a) from 100 mV s^{-1} to 500 mV s^{-1} and (b) from 5mV s^{-1} to 100 mV s^{-1} in a potential windows of 0.25 to 0.65 V in 6M KOH electrolyte.

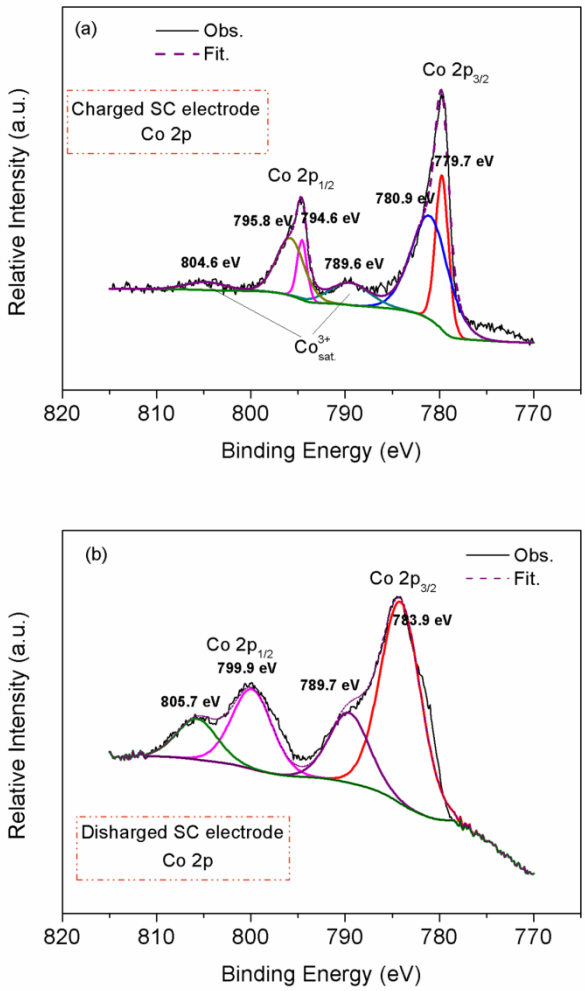

Figure 3.6 The Co2p XPS spectrum of (a) charged and (b) discharged SC electrode at room temperature.

Compared to Co_3O_4, BSCF experienced a much larger degree of increment in capacitance in the initial 8 h of cycling, i.e., from an initial value of around 200 to as high as 610 F g^{-1}. Such large increment could not be solely explained by the surface activation process. After reaching the peak capacitance at around 100th cycle, a sharp decrease in capacitance with a further increase in cycling time was observed. As demonstrated from the previous investigation, the leaching of Ba^{2+} and Sr^{2+} from the lattice structure of BSCF was happened when it was immersed alkaline solution, and such leaching led to an increase in specific surface area of the sample, while the over leaching could cause the phase transition of the perovskite structure. As demonstrated previously, a phase transition started to occur at a treatment time of around 8 h for the BSCF oxide, and it finally changed to amorphous phase when the treatment time was

prolonged to 72 h. An increase in specific surface area should be beneficial for surface reaction while the phase transition could destroy/reduce the oxygen anion intercalation sites (mobile oxygen vacancies) and impaired the oxygen-anion bulk phase diffusion channels. Clearly, the quick increase in capacitance in the first 8 h period was due to the surface activation as well as the increased specific surface area owing to the dissolution of surface impurity and leaching of Ba^{2+}/Sr^{2+}, respectively. However, a phase transition was occurred with a further increase of cycling times due to the over leaching of Ba^{2+}/Sr^{2+}, which were likely to reduce the oxygen bulk diffusion rate and oxygen vacancy concentration significantly. As a result, a sharp decrease in capacitance for the BSCF electrode was observed with a further increase in cycling times. Thus, appropriate tailoring of the components in order to avoid over leaching of compositional cations was critical to achieve a stable capacitance performance for perovskite oxides as oxygen anion-intercalation type electrodes for supercapacitors with alkaline solution electrolyte.

As to the SC electrode, after the most significant improvement in capacitance at the first 8 h of cycling, a progressive increase in capacitance with cycling times was still observed, until it reached the maximum capacitance of around 572 F g^{-1} at around 3500 cycles, then a slight decrease in capacitance with cycling time was observed. Anyway, a capacitance of 500 F g^{-1} was still maintained after the continuous cycling for 5000 times for SC electrode. As demonstrated previously, SC showed much improved phase stability as compared to BSCF in alkaline solution, due to much lower degree in the leaching of alkaline earth cation. As a result, no sharp decrease in capacitance with the cycling times was observed. Actually, a slow increase in capacitance with cycling times was observed for the first 4000 cycles. In combination with the results of XRD and BET specific surface area of SC after the treatment in alkaline solution for different times, such improvement should be related to the increased specific surface area of SC from the leaching of Sr^{2+} into the alkaline solution. The increased surface area enhanced the surface reaction rate, which improved the capacitance of SC with cycling time.

As mentioned, for oxygen anion-intercalation type supercapacitor electrodes, the energy storage involved both the surface reaction as well as oxygen anion bulk diffusion. If the energy storage process was rate determined mainly by slow oxygen-ion bulk diffusion process, a change in specific surface area should have no obvious

effect on the capacitance of the electrode. Previously we demonstrated that SCNb, a cubic perovskite oxide, was mainly limited by surface reaction in the energy storage process when it performed as an oxygen anion intercalation-type electrode for supercapacitor.[23] BSCF was reported to have higher oxygen diffusion capability than SC because of the Ba and Fe co-doping stabilized the oxygen vacancy-disordered cubic lattice structure, which was actually one of the most famous mixed oxygen-ion and electron conductors for SOFCs and ceramic oxygen permeating membranes.[48] Thus, the quick increase in capacitance for BSCF electrode in the initial cycling stage was easy to understand, i.e., the increased surface area promoted the surface reaction. SC, as the parent oxide for BSCF, was reported to have much lower oxygen diffusivity. The bulk diffusion was thus a big concern for energy storage in SC electrode. To probe the basic charge process behaviour in the SC electrode, **Figure 3.7** presented a plot of log (i) versus log (v) from 0.1 to 500 mV s^{-1} for anodic and cathodic peaks based on the result of CVs in **Figure 3.5**. According to the power law relationship between current and sweep rate:

$$i = av^b \tag{3.1}$$

where *a* and *b* were adjustable values such that *b* value of 1 indicated that the current was surface controlled, while *b* value of 0.5 would indicated that the current was controlled by linear diffusion. Based on the plot, the *b* factor exhibited a value for both anodic and cathodic current of 0.846 and 0.870 at the scan rates from 0.1 to 20 mV s^{-1} and a value of 0.638 and 0.679 at the scan rates from 30 to 500 mV s^{-1} scan rates ranges, respectively. It suggests that, at relatively low scan rate, the SC electrode was also mainly rate-limited by the low surface process. In other words, the oxygen-anion diffusion rate under polarization condition in SC was still favourably high. The slow yet steady increase in capacitance with cycling times up to 4000 cycles could be well explained by the slow increase in specific surface area from the selective leaching of Sr^{2+} in SC into the alkaline solution during cycling.

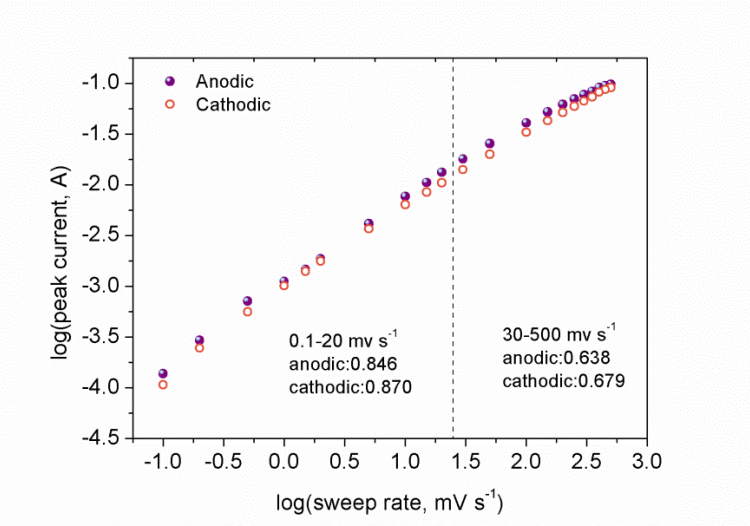

Figure 3.7. The b value determination of normalized anodic and cathodic peak currents.

Based on the results above, it was apparent that although Ba^{2+} doping could stabilise the oxygen vacancy-disordered cubic perovskite structure, it may not be the best choice for developing perovskite oxides as oxygen-anion intercalation type electrodes for supercapacitors because the leaching of Ba^{2+} in high-concentration alkaline solution is easy to occur, which could destroy the perovskite structure, thus inhibiting the oxygen ion diffusion as well as destroying the oxygen vacancy sites. Interestingly, the parent oxide SC was still an attractive electrode material for supercapacitors. Under polarization condition, the oxygen-ion diffusion rate was still sufficiently high; as a result, the surface reaction was the main rate limiting step for energy storage process. On the other hand, the modest leaching behaviour created beneficial effects by increasing the specific surface area but not damaging the perovskite structure. As a result, improved capacitance with cycling times was observed for the SC electrode. The favourable oxygen bulk diffusion was further supported by the high capacitance retention at high rate as demonstrated in **Figure 3.8**. Specific capacitances of 572, 560, 512 and 420 F g^{-1} at current densities of 1, 2, 5 and 10 A g^{-1} respectively, were obtained.

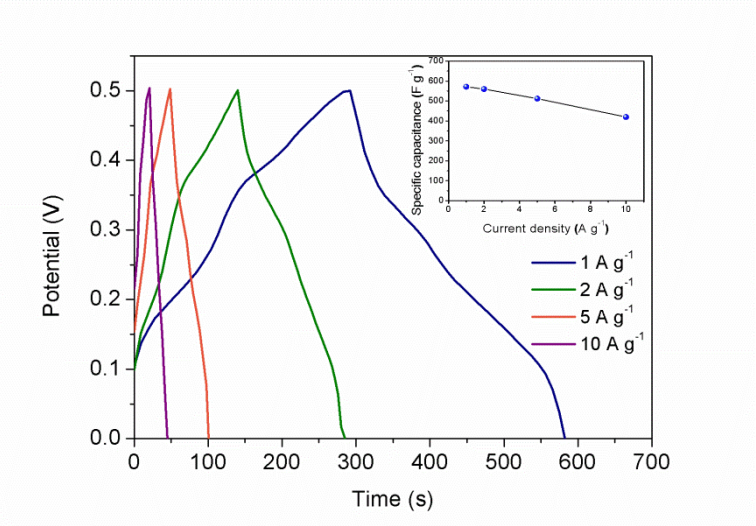

Figure 3.8 Charge-discharge profiles of SC at various current density in 6M KOH aqueous solution. The inset is the specific capacitance as a function of current density.

3.3.3 Application in asymmetric supercapacitor

Lastly, an asymmetric supercapacitor (ASC) was synthesised by utilising activated carbon (AC) in place of a negative electrode and SC as the positive electrode. **Figure 3.9a** displayed the CV curves of the ASC at various scan rates in the potential range of 0-1.5 V. All of the CV curves consisted of a pair of well-defined redox peaks, indicative of Faradaic redox reaction being the main influence on capacitance characteristics. When compared to electric double layer capacitors that usually produced a CV curve close to an ideal rectangular shape, difference in Faradaic mechanisms are evident. The galvanostatic charge/discharge (GCD) curves of the ASC at current densities of 1-10 A g^{-1} were shown in **Figure 3.9b**. Encouragingly, the Ni foam supported SC electrode exhibited excellent specific capacitances of 87, 85, 83 and 80 F g^{-1} at current densities of 1, 2, 5 and 10 A g^{-1}, respectively. This suggested that about 92% of the capacitance was still retained after the charge-discharge rate was increased from 1 A g^{-1} to 10 A g^{-1}. The energy density (E) and power density (P) for the ASC were calculated based on the galvanostatic discharge curves according to the following formulas:[49]

$$\mathrm{E} = \frac{1}{2} \times C_m \times \Delta V^2 \tag{3.2}$$

$$\mathrm{P} = \frac{E}{\Delta t} \tag{3.3}$$

where Cm (F g^{-1}) was the specific capacitance of the ACS, E (Wh kg^{-1}) is the energy density, P (W kg^{-1}) was the power density and ΔV (V) is the discharge potential window.[49] The calculation of energy density and power density are dependent on the weight of electrode active materials only. **Figure 3.9c** manifested the Ragone plot of the relevant value of energy densities and power densities for the ASC. The ASC delivered a high energy density of 27.5 Wh kg^{-1} at a power density of 750 Wkg^{-1} (1 A g^{-1}), and the energy density retained a decent value of 25 Wh kg^{-1} even at a power density of 7500 kW kg^{-1} (10 A g^{-1}). As shown in **Figure 3.9d**, it can be seen that the specific capacitance of both the electrodes increased slowly in the first 300 cycles, which may be attributed to the complete activation of the electrode. It showed a specific capacitance of 88 F g^{-1} after 2000 cycles, suggesting long operational life and robust stability.

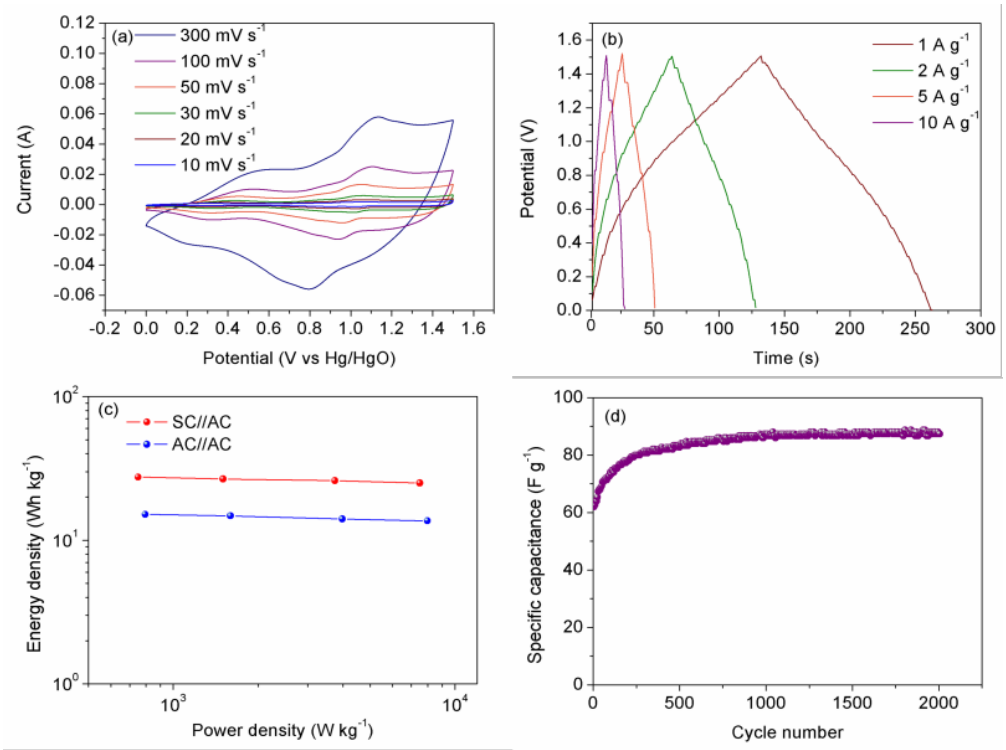

Figure 3.9 (a) CV curves at different scan rates and (b) galvanostatic charge/discharge curves at different current densities of the SC//AC ASC. (c) Ragone plots of the SC//AC and AC//AC device. (d) Cycling performance of SC//AC ASC at a current density of 1 A g^{-1}.

3.4 Conclusions

Forming perovskite compounds to introduce oxygen anion-intercalation-type charge storage mechanism was an effective way to significantly improve the capacitance of cobalt-based oxides as electrodes for supercapacitor. A high oxygen vacancy concentration was critical to achieve high capacitance. In order to maintain stable performance, the dopant should be carefully selected to avoid the over-leaching of selective cations in alkaline solution, which may cause the collapse of perovskite structure, thus detrimentally affected the electrode performance. From this consideration, although it had high initial capacitance from the high variable oxygen vacancy concentration, BSCF was not a good candidate because of poor cycling stability. This poor stability was resulted from the significant leaching of Ba^{2+} and Sr^{2+} in alkaline solution during cycling, which destroyed the perovskite structure seriously. Interestingly, modest level of cation leaching can help to increase the specific surface area without affecting the perovskite phase structure; as a result, the surface reaction was promoted and the electrode performance was subsequently improved. Although the hexagonal SC was believed to have poor oxygen-ion conductivity due to the structural ordering, favourable rate performance was still achieved as electrode in supercapacitors. It implied that improved oxygen anion diffusivity was likely experienced under electrically biased condition. All above findings provided useful guidelines for the design of perovskite oxides as high-performance oxygen anion-intercalation type electrodes for supercapacitors. As a whole, SC was a promising electrode candidate for practical use in supercapacitors. Stabilizing its oxygen vacancy-disordered cubic phase through doping strategy by using dopant other than Ba^{2+} could be a useful way to further improve the electrode performance of SC in the future.

3.5 Reference

[1] R. Subbaraman, D. Tripkovic, K.-C. Chang, D. Strmcnik, A.P. Paulikas, P. Hirunsit, M. Chan, J. Greeley, V. Stamenkovic, N.M. Markovic, Nat. Mater., 11 (2012) 550-557.

[2] R. Borup, J. Meyers, B. Pivovar, Y.S. Kim, R. Mukundan, N. Garland, D. Myers, M. Wilson, F. Garzon, D. Wood, P. Zelenay, K. More, K. Stroh, T. Zawodzinski, J. Boncella, J.E. McGrath, M. Inaba, K. Miyatake, M. Hori, K. Ota, Z. Ogumi, S. Miyata,

A. Nishikata, Z. Siroma, Y. Uchimoto, K. Yasuda, K.-i. Kimijima, N. Iwashita, Chem. Rev., 107 (2007) 3904-3951.
[3] M.G. Walter, E.L. Warren, J.R. McKone, S.W. Boettcher, Q. Mi, E.A. Santori, N.S. Lewis, Chem. Rev., 110 (2010) 6446-6473.
[4] J.-H. Im, J. Luo, M. Franckevičius, N. Pellet, P. Gao, T. Moehl, S.M. Zakeeruddin, M.K. Nazeeruddin, M. Grätzel, N.-G. Park, Nano Lett., 15 (2015) 2120-2126.
[5] G. Niu, X. Guo, L. Wang, J. Mater. Chem. A, 3 (2015) 8970-8980.
[6] X. Sun, P.V. Radovanovic, B. Cui, New J. Chem., 39 (2015) 38-63.
[7] B.J. Landi, M.J. Ganter, C.D. Cress, R.A. DiLeo, R.P. Raffaelle, Energy Environ. Sci., 2 (2009) 638-654.
[8] X. Chen, B. Zhao, Y. Cai, M.O. Tade, Z. Shao, Nanoscale, 5 (2013) 12589-12597.
[9] C. Duan, J. Tong, M. Shang, S. Nikodemski, M. Sanders, S. Ricote, A. Almansoori, R. O'Hayre, Science, 349 (2015) 1321-1326.
[10] L.L. Zhang, X.S. Zhao, Chem. Soc. Rev., 38 (2009) 2520-2531.
[11] M. Beidaghi, Y. Gogotsi, Energy Environ. Sci., 7 (2014) 867-884.
[12] P. Simon, Y. Gogotsi, Nat. Mater., 7 (2008) 845-854.
[13] G. Wang, L. Zhang, J. Zhang, Chem. Soc. Rev., 41 (2012) 797-828.
[14] E. Frackowiak, Phys. Chem. Chem. Phys., 9 (2007) 1774-1785.
[15] T.-Y. Wei, C.-H. Chen, H.-C. Chien, S.-Y. Lu, C.-C. Hu, Adv. Mater., 22 (2010) 347-351.
[16] L. Kong, C. Zhang, S. Zhang, J. Wang, R. Cai, C. Lv, W. Qiao, L. Ling, D. Long, J. Mater. Chem. A, 2 (2014) 17962-17970.
[17] V. Augustyn, J. Come, M.A. Lowe, J.W. Kim, P.-L. Taberna, S.H. Tolbert, H.D. Abruña, P. Simon, B. Dunn, Nat. Mater., 12 (2013) 518-522.
[18] J.W. Kim, V. Augustyn, B. Dunn, Adv. Energy Mater., 2 (2012) 141-148.
[19] K.M. Hercule, Q. Wei, O.K. Asare, L. Qu, A.M. Khan, M. Yan, C. Du, W. Chen, L. Mai, Adv. Energy Mater., 5 (2015) 1500060.
[20] Z. Li, K. Xiang, W. Xing, W.C. Carter, Y.-M. Chiang, Adv. Energy Mater., 5 (2015) 1401410.
[21] M. Zhu, W. Meng, Y. Huang, Y. Huang, C. Zhi, ACS Appl. Mater. Interfaces, 6 (2014) 18901-18910.
[22] J.T. Mefford, W.G. Hardin, S. Dai, K.P. Johnston, K.J. Stevenson, Nat. Mater., 13 (2014) 726-732.

[23] L. Zhu, Y. Liu, C. Su, W. Zhou, M. Liu, Z. Shao, Angew. Chem. Int. Ed., (2016) DOI: 10.1002/anie.201603601.
[24] W.L. Warren, K. Vanheusden, D. Dimos, G.E. Pike, B.A. Tuttle, J. Am. Ceram. Soc., 79 (1996) 536-538.
[25] M. Cherry, M.S. Islam, C.R.A. Catlow, J. Solid State Chem., 118 (1995) 125-132.
[26] G. Kim, S. Wang, A.J. Jacobson, L. Reimus, P. Brodersen, C.A. Mims, J. Mater. Chem., 17 (2007) 2500-2505.
[27] Z. Shao, S.M. Haile, Nature, 431 (2004) 170-173.
[28] F. Dong, Y. Chen, R. Ran, D. Chen, M.O. Tade, S. Liu, Z. Shao, J. Mater. Chem. A, 1 (2013) 9781-9791.
[29] W. Zhou, J. Sunarso, M. Zhao, F. Liang, T. Klande, A. Feldhoff, Angew. Chem. Int. Ed., 52 (2013) 14036-14040.
[30] Y. Liu, R. Ran, S. Li, Y. Jiao, M.O. Tade, Z. Shao, J. Power Sources, 257 (2014) 308-318.
[31] E. Fabbri, D. Pergolesi, E. Traversa, Chem. Soc. Rev., 39 (2010) 4355-4369.
[32] A.F. Sammells, R.L. Cook, J.H. White, J.J. Osborne, R.C. MacDuff, Solid State Ionics, 52 (1992) 111-123.
[33] J. Chmiola, G. Yushin, Y. Gogotsi, C. Portet, P. Simon, P.L. Taberna, Science, 313 (2006) 1760-1763.
[34] C. Yuan, L. Yang, L. Hou, L. Shen, X. Zhang, X.W. Lou, Energy Environ. Sci., 5 (2012) 7883-7887.
[35] W. Chen, R.B. Rakhi, L. Hu, X. Xie, Y. Cui, H.N. Alshareef, Nano Lett., 11 (2011) 5165-5172.
[36] C. Su, X. Xu, Y. Chen, Y. Liu, M.O. Tadé, Z. Shao, J. Power Sources, 274 (2015) 1024-1033.
[37] Y. Wang, Y. Lei, J. Li, L. Gu, H. Yuan, D. Xiao, ACS Appl. Mater. Interfaces, 6 (2014) 6739-6747.
[38] Y. Wang, T. Zhou, K. Jiang, P. Da, Z. Peng, J. Tang, B. Kong, W.-B. Cai, Z. Yang, G. Zheng, Adv. Energy Mater., 4 (2014) 1400696.
[39] C. Lin, J.A. Ritter, B.N. Popov, J. Electrochem. Soc., 145 (1998) 4097-4103.
[40] X. Lu, D. Zheng, T. Zhai, Z. Liu, Y. Huang, S. Xie, Y. Tong, Energy Environ. Sci., 4 (2011) 2915-2921.
[41] B.E. Conway, V. Birss, J. Wojtowicz, J. Power Sources, 66 (1997) 1-14.
[42] W. Zhou, Z. Shao, R. Ran, W. Jin, N. Xu, Chem. Commun., (2008) 5791-5793.

[43] H. Taguchi, M. Shimada, M. Koizumi, J. Solid State Chem., 29 (1979) 221-225.
[44] W. Li, L. Xin, X. Xu, Q. Liu, M. Zhang, S. Ding, M. Zhao, X. Lou, Sci. Rep., 5 (2015) 9277.
[45] T.J. Chuang, C.R. Brundle, D.W. Rice, Surf. Sci., 59 (1976) 413-429.
[46] Y. Okamoto, T. Imanaka, S. Teranishi, J. Catal., 65 (1980) 448-460.
[47] M. O'Connell, A.K. Norman, C.F. Hüttermann, M.A. Morris, Catal. Today, 47 (1999) 123-132.
[48] W. Zhou, R. Ran, Z. Shao, J. Power Sources, 192 (2009) 231-246.
[49] Z. Fan, J. Yan, T. Wei, L. Zhi, G. Ning, T. Li, F. Wei, Adv. Funct. Mater., 21 (2011) 2366-2375.

Chapter 4 Highly defective layered double perovskite oxide for efficient energy storage via reversible pseudocapacitive oxygen-anion intercalation[§]

Abstract

The use of perovskite materials as anion-based intercalation pseudocapacitor electrodes has received significant attention in recent years. Notably, these materials, characterized by high oxygen vacancy concentrations, do not require high surface areas to achieve a high energy storage capacity as a result of the bulk intercalation mechanism. Here we report that reduced $PrBaMn_2O_{6-\delta}$ (r-PBM), possessing a layered double perovskite structure, exhibits ultrahigh capacitance and functions as an excellent oxygen anion-intercalation-type electrode material for supercapacitors. Formation of the layered double perovskite structure, as facilitated by hydrogen treatment, is shown to significantly enhance the capacitance, with the resulting r-PBM material demonstrating a very high gravimetric capacitance of 1034.8 F g^{-1} and an excellent volumetric capacitance of approximately 2535.3 F cm^{-3} at a current density of 1 A g^{-1}. The resultant formation of a double perovskite crystal oxide with a specific layered structure leads to the r-PBM with a substantially higher oxygen diffusion rate and oxygen vacancy concentration. These superior characteristics show immense promise for their application as oxygen anion-intercalation-type electrodes in pseudocapacitors.

[§]*Reprinted (adapted) with permission from (Y. Liu, Z.B. Wang, J.P. Veder, Z.Y. Xu, Y.J. Zhong, W. Zhou, M.O. Tadé, S.B. Wang, Z.P. Shao, Highly defective layered double perovskite oxide for efficient energy storage via reversible pseudocapacitive oxygen-anion intercalation, Adv. Energy Mater. 2018, 1702604). Copyright (2018) John Wiley and Sons.*

4.1 Introduction

Electrochemical energy storage and conversion devices, including lithium-ion batteries (LIBs) and supercapacitors, play important roles in modern society by creating a more convenient and sustainable life for our future. For example, LIBs are arguably the most reliable and heavily used power sources for personal electronics, such as smart phones, digital cameras and laptops. More recently, LIBs and supercapacitors have also been widely considered as power systems for electric vehicles. They have also attracted significant attentions in large-scale energy storage options for renewable energies, such as wind and solar power, as well as grid energy storage.

Energy density, power density, cycling stability and cost are four crucial concerns in the development and exploitation of electrochemical energy storage devices. LIBs, which are dependent on intercalation, conversion or alloying reactions over their electrodes for energy storage, usually exhibit favourable energy densities; however, the associated power densities and cycling stabilities are sometimes insufficient for many applications. Supercapacitors, which store energy via charge adsorption over the electrode (carbon) surface or through Faradaic redox reactions over the electrode (typically an oxide or polymer) surface or subsurface, have attracted worldwide attentions because of their higher power density than traditional capacitors and substantially longer cycle life (> 100,000 cycles) when compared to LIBs. Significant efforts have been directed towards the improvement of energy density of supercapacitors.[1-3] By optimizing the electrode microstructure and surface area, a maximum capacitance of 150-300 F g^{-1} can be achieved using a carbon-based electrode based on the electric double-layer capacitors (EDLC) for energy storage,[4] while a capacitance more than 10 times higher can be obtained with a pseudocapacitive electrode based on surface Faradaic redox reactions.[5-7] Recent progress in the development of nanostructured electrodes has seen the gap in energy density and power density between LIBs and supercapacitors diminish significantly. Some intercalation-type nanostructured electrodes for new energy applications have demonstrated impressive capacitive charge storage.[8-10] However, the nanostructure may lead to a low pack density of the electrode, leading to poor volumetric energy density of the corresponding supercapacitor. Importantly, in many portable electronics applications, the volumetric energy density is a more important characteristic than the

gravimetric energy density. It is still a considerable challenge to develop energy materials with high power densities, high volumetric energy densities and good cycling stability at low cost.

Recently, a new type of supercapacitor has emerged that utilizes the cations (e.g., Li^+) for charge storage with a view to enhancing energy density while maintaining the high power density of conventional supercapacitors.[9-12] For example, orthorhombic Nb_2O_5 nanocrystals were shown to exhibit an intercalation pseudocapacitive phenomenon, whereby the Nb_2O_5 crystalline network provided an abundance of two dimensional transport channels for Li^+ intercalation/de-intercalation with minimal destructive structural changes.[9] Tolbert et al. found that mesoporous crystalline MoO_3 had an intercalation pseudocapacitance comparable to traditional redox pseudocapacitors due to its unique nanoscale architecture.[12] Hence, intercalation supercapacitance provides a new approach for the development of electrochemical energy storage devices with both desirable energy density and power density.

It is a widely held belief that oxygen anion diffusion in the oxides at room temperature is difficult due to the relatively large size of anion. Intriguingly, Kudo et al.[13] demonstrated in 1973 that reversible electrochemical intercalation of oxygen into defective $Nd_{1-x}Sr_xCoO_{3-\delta}$ perovskite oxide was possible in a KOH solution at room temperature. The calculated diffusion constant was as high as 1.4×10^{-11} cm^2 s^{-1}. More recently, the oxygen anion intercalation capability of $LaMnO_3$ lattices has been exploited by Johnston et al. for energy storage, reaching a capacitance of approximately 600 F g^{-1} for a reduced $LaMnO_3$ perovskite oxide at room temperature, as calculated on the basis of the cyclic voltammetry (CV) tests.[14] Subsequently, we demonstrated that a Nb-doped $SrCoO_{3-\delta}$ perovskite with a high oxygen vacancy concentration behaved as a promising pseudocapacitors electrode with a gravimetric capacitance of 773.6 F g^{-1}. Its volumetric capacitance reached approximately 2034.6 F cm^{-3} with exceptional cycling stability after several thousand cycles.[15] Nevertheless, major concerns regarding the high price of cobalt and the easy leaching of cobalt into the aqueous systems that surround the use of cobaltite-based perovskites render their widespread adoption undesirable. Clearly, new cobalt-free materials that possess high oxygen vacancy concentrations and oxygen anion diffusion rates are crucial for the widespread realization of this developing technology.

Since volumetric energy density is highly dependent on the packing density of the electrode material, it is preferable to prepare pore-free electrode materials with a high tap density. To maximize the intercalation pseudocapacitance, the amount of accessible oxygen defect sites and the diffusion rate of oxygen anions inside the oxide lattice should also be maximized. Several reports indicated that some layered double perovskite oxides possessed fast oxygen ion diffusion channels, in which the oxygen diffusion exhibited a very low activation energy.[16, 17] In fact, the oxygen-ion conductivities of some double perovskites are even higher than those of many benchmark single perovskite oxides.[18, 19] Furthermore, many double perovskite oxides also present high concentrations of variable oxygen vacancies. These favourable properties suggest that such materials may be developed into electrodes materials for oxygen anion-intercalation-type supercapacitors.

In this study, we provide the very first report of the use of reduced $PrBaMn_2O_{6-\delta}$ (r-PBM) with a layered double perovskite structure as an excellent oxygen anion-intercalation-type electrode material in supercapacitors. A maximum gravimetric capacitance of 1034.8 F g^{-1} (> 1000 F g^{-1}) was attained in a liquid electrolyte of a 6 M KOH solution for a coarse-type r-PBM with a low specific surface area of only 7.83 m^2 g^{-1}. The pore-free nature of r-PBM also resulted in an ultrahigh volumetric capacitance of 2535.3 F cm^{-3}, which is the highest reported value. The formation of the layered double perovskite structure facilitated by hydrogen treatment was found to significantly increase both the oxygen vacancy concentration and oxygen anion diffusion rate, thus contributing to the outstanding capacitance. Notably, Mn leaching in alkaline solution was minimal compared with the leaching of cobalt in a $PrBaCo_2O_{6-\delta}$ (PBC) double perovskite. Cumulatively, these outstanding features make r-PBM a highly promising electrode material for oxygen anion-intercalation-type supercapacitors.

4.2 Experimental section

Preparation of f-PBM and r-PBM: $Pr_{0.5}Ba_{0.5}MnO_{3-\delta}$ (f-PBM) was synthesized following our previously reported EDTA-CA complexing approach. In a typical procedure, stoichiometric quantities of Pr, Ba and Mn nitrates (praseodymium (III) nitrate hexahydrate (99.9%), barium nitrate (≥99%), manganese (II) nitrate tetrahydrate (99%), Sigma-Aldrich) were dissolved in Milli-Q water under magnetic

stirring for 30 min at 80 °C in air. Once a clear solution was obtained, ethylenediaminetetraacetic acid and anhydrous citric acid (EDTA (99%) and CA (99.5%), Sigma-Aldrich) were added into the above solution and served as complexing agents with a molar ratio of 1:2; the molar ratio of metal ion to EDTA was 1:1. During heating to evaporate water, $NH_3 \cdot H_2O$ was used to regulate the pH value of the mixture to approximately 7 to avoid precipitation. A transparent gel was obtained after the removal of water, and then the gel was treated in an oven at 250 °C for 6 h to obtain a solid black-coloured precursor, which was further sintered at 950 °C for 10 h in a muffle furnace with a heating rate of 5 °C min^{-1} to obtain the target material. The A-site layered $PrBaMn_2O_{6-\delta}$ (r-PBM) perovskite oxide was obtained by sintering f-PBM oxide under a hydrogen atmosphere at 800 °C for 45 minutes. $PrBaMn_2O_{6-\delta}$ and $La_{0.5}Sr_{0.5}MnO_{3-\delta}$ (LSM) were synthesized by the following same procedure as that of f-PBM.

Basic characterization: The crystal structures of the as-prepared powder samples were investigated at room-temperature via X-ray diffraction (model D8 Advance, Bruker, Germany) using filtered Cu Kα radiation (λ = 1.5418 Å) step-scanning in the 2θ range of 10-80°. TEM samples were prepared by crushing the crystals in a mortar, an ultrasonic treatment in ethanol, and then depositing onto a carbon-support copper grid. Electron diffraction patterns, HRTEM images, HAADF-STEM images and energy dispersive X-ray spectra were obtained with a Titan G^2 80−200 with an electron microscope operated at 200 kV. X-ray photoelectron spectroscopy (XPS) measurements were undertaken using a Kratos AXIS Ultra DLD system with monochromated Al Kα X-rays (1486.7 eV) under ultrahigh vacuum conditions (<1 × 10^{-9} mbar). The spectra were analyzed by CasaXPS software and calibrated to yield a primary C 1s component at 284.8 eV. The specific surface areas of as-synthesized powders were characterized by nitrogen adsorption tests (Micromeritics Tristar 3000) using the Brunauer-Emmett-Teller (BET) method. Approximately 1.0 g of each sample was weighed and degassed at 200 °C for at least 6 h before N_2 physisorption measurements at the boiling point of liquid nitrogen (77 K). The room temperature oxygen non-stoichiometry of various perovskite oxides was determined by the iodometric titration method.

Electrochemical Measurements: The electrochemical performance of the synthesized samples was tested by cyclic voltammetry (CV), and the samples were analysed with

a Solartron Analytical 1287A potentiostat/galvanostat using a three-electrode arrangement. The galvanostatic charge and discharge (GCD) tests were carried out on a NEWARE battery tester (Shenzhen, China), and the galvanostat was controlled by a computer in the same system. The electrode was prepared according to a previous report.[15] A mixture of the active materials, carbon black (Super-P), and poly(tetrafluoroethylene) (PTFE) in a mass ratio of 80: 15: 5 was prepared into a film and dried at 100 °C for 24 h in an electric vacuum oven, which was then pressed between two nickel foams. The total mass of the working electrode material (active material +carbon black+ PTFE) was approximately 3 mg cm^{-2}. For the three-electrode system, a Hg/HgO electrode filled with 1 M KOH was used as the reference electrode, a Pt plate as the counter electrode, and a 6 M KOH solution as the electrolyte.

Oxygen diffusion rate measurements: The reversible oxygen diffusion rates of PBM were measured by an adaptation of a procedure in the literature.[25, 38-40] In a typical measurement, cyclic voltammetry was first performed in a three-electrode setup with a 6 M KOH electrolyte solution at 20 mVs^{-1}. Then, a difference of the redox peak shift of 50 mV in the anodic direction was used as the potential in the following chronoamperometric current test. After the electrode was tested chronoamperometrically for 4 hours, the result was applied in the calculation of the oxygen diffusion rate.

NEXAFS Experimental: Near-edge X-ray absorption fine structure (NEXAFS) spectroscopy measurements were conducted at the Soft X-ray beamline of the Australian Synchrotron.[41] These measurements were carried out at room temperature under ultra-high vacuum (UHV) conditions with a base pressure of 5×10^{-10} mbar or better. All spectra were obtained in total electron yield (TEY) mode. The NEXAFS spectra were recorded at the Mn L-edge (630-670eV). All NEXAFS spectra were processed and normalized using the QANT software programme developed at the Australian Synchrotron[42]. X-ray energy calibrations were achieved by applying the offset required to shift the simultaneously measured reference spectra of manganese foil to its known energy position. The intensities were normalized with respect to the impinging photon flux.

DFT Computational method: The spin-polarized density functional theory (DFT) calculations were performed using the Vienna ab initio simulation package (VASP)

within the projected-augmented wave method.[43, 44] The generalized gradient approximation (GGA) Perdew-Burke-Ernzerhof (PBE) function was adopted to describe the exchange-correlation interaction.[45] The DFT+U approach was used to correct the self-interaction error of standard DFT with a Hubbard U value of 3.9 eV for Mn.[46, 47] The energy cut-off was 520 eV. The electronic energy and atomic force were smaller than 1-5 eV and 0.01 eV/Å, respectively. The k-point mesh density was at least 0.05 $Å^{-1}$ along each direction when integrating the Brillouin zone. The 2×2×2 supercell was constructed to calculate the oxygen vacancy formation energy, which was defined as the following equation:

$$Evac = E[defect] + 1/2\ E[O_2] – E[perfect],$$

where E[defect] and E[perfect] are the total electronic energies of defective and perfect systems, respectively. $E[O_2]$ is the ground state energy of triplet O_2. The formation energies of an oxygen vacancy are averaged in terms of oxygen site multiplicity in the crystal structure.

4.3 Results and Discussions

4.3.1. Structure and microstructure characterizations

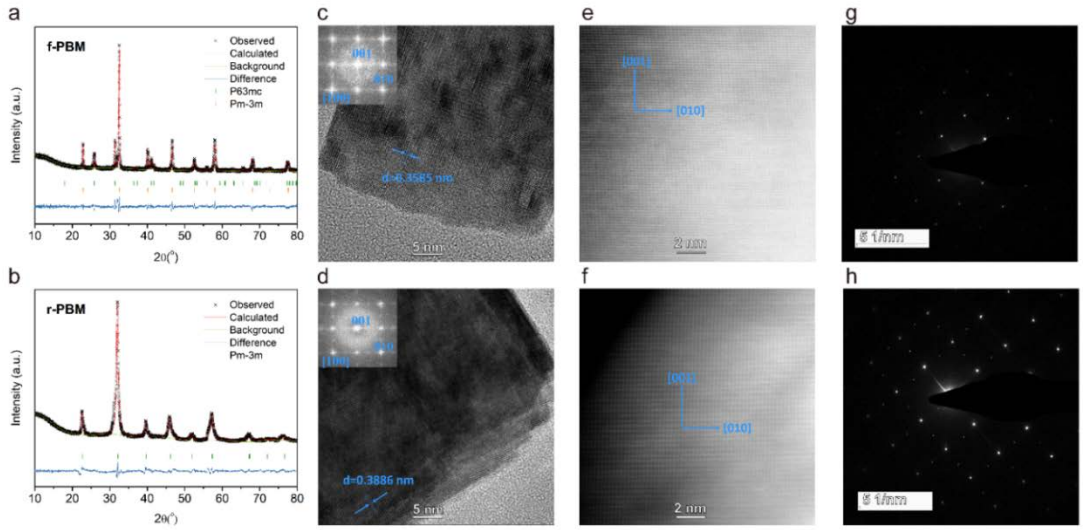

Figure 4.1 XRD patterns and Rietveld refinement fits for a) f-PBM and b) r-PBM. The diffraction peaks of f-PBM could be indexed to a mixture of *Pm-3m* and *$P6_3mc$* phases, and the peaks of r-PBM could be indexed to a single phase of *Pm-3m*. HR-TEM images of c) f-PBM and d) r-PBM; the insets show the FFT pattern with zone axis (Z.A.) =

[100]. HAADF-STEM images of e) f-PBM and f) r-PBM, and their atomic arrangements. SAED patterns of g) f-PBM and h) r-PBM.

The performance of a material as an oxygen anion-intercalation-type electrode in a supercapacitor is closely related to the existence of accessible oxygen defect sites as well as the oxygen anion diffusion rate. In turn, these properties are closely dependent on the phase structure of the target material. Based on the ionic radius database and tolerance factor calculation equation, the tolerance factor values for $Pr_{0.5}Ba_{0.5}MnO_{3-\delta}$ (f-PBM) and $PrBaMn_2O_{6-\delta}$ (r-PBM) were calculated to be 0.914 and 0.835, respectively, assuming the high spin states of Mn^{2+}, Mn^{3+} and Mn^{4+}. This further implies that $PrBaMn_2O_{6-\delta}$ can theoretically maintain a perovskite crystal structure with a wide range of oxygen nonstoichiometries. However, in some cases, the large difference in cation size of dopant from the host may result in cation ordering. For instance, it was previously reported that A-site cation ordering was appeared in a $PrBaCo_2O_{6-\delta}$ perovskite, resulting in the formation of a layered double perovskite with the structure [BaO]-[CoO_2]-[PrO_x]-[CoO_2]-[BaO].[20]

Table 4.1 The results of lattice parameters and fitting parameters of Rietveld refinement

	PBM		r-PBM
Space group	*P6$_3$mc*	*Pm-3m*	*Pm-3m*
a(Å)	5.698(3)	3.896(2)	3.941(7)
b(Å)	5.698(3)	3.896(2)	3.941(7)
c(Å)	4.814(6)	3.896(2)	3.941(7)
R_p	0.0634		0.0405
R_{wp}	0.0842		0.0632
χ^2	1.343		1.625

$PrBaMn_2O_{6-\delta}$ was first developed by Kim et al. and applied in the anode side of high-temperature solid oxide fuel cells (SOFCs). They found that $PrBaMn_2O_{6-\delta}$ possessed a mixed cubic and hexagonal structure when synthesized in air, while an A-site cation-ordered double perovskite was formed when the sample was further treated in H_2 at 800 °C.[21] Our results from the Rietveld refinement of the X-ray diffraction (XRD) patterns, as shown in **Figure. 4.1a,b**, confirm that the $Pr_{0.5}Ba_{0.5}MnO_{3-\delta}$ synthesized

from the calcination of the sol-gel precursor in air at 850 °C for 5 h (f-PBM) possessed a mixed cubic and hexagonal structure. This subsequently alters to an A-site cation-ordered double perovskite structure after a treatment in pure hydrogen at 800 °C for 45 min (r-PBM). **Table 4.1** presents the parameters established via the Rietveld refinement, including lattice parameters, bond lengths, bond angles and site occupancies. These phase compositions are further supported by high-resolution transmission electron microscopy (HR-TEM) observations **(Figure 4.1c,d)**. Highly-crystalline structures were formed for both f-PBM and r-PBM. The HR-TEM images of both f-PBM and r-PBM clearly demonstrate their polyhedral morphological structures. For f-PBM, lattice fringes with a d-spacing of 0.3585 nm were observed, which corresponds to the (100) plane of dual-phase f-PBM. The HR-TEM image of r-PBM exhibits a lattice spacing of 0.3886 nm, matching well with the spacing of the (100) plane of the double perovskite. The weak additional spot with excellent indexing to the (001) of a tetragonal superlattice presented in the fast Fourier transformed (FFT) pattern confirms the existence of A-site ordering in r-PBM. Importantly, the tetragonal superlattice is linked to structural relaxation in these planes.[21] High-angle annular dark-field scanning TEM (HAADF-STEM) images show an atomic arrangement aligned along the [100] direction for the r-PBM sample, suggesting a periodic layered arrangement of atoms. The A-site layered structure of r-PBM was also corroborated by the selected area electron diffraction pattern (SAED), which possessed a weak spot indexed to the (001) compared with the SAED pattern of f-PBM. The HADDF-STEM image and elemental mapping based on energy-dispersive X-ray spectroscopy (EDX) measurements (**Figure. 4.2**) show the existence and uniform dispersion of Pr, Ba, Mn and O elements in the f-PBM and r-PBM, indicating the existence of homogeneous phase even after high-temperature reduction. As a comparison, $La_{0.5}Sr_{0.5}MnO_{3-\delta}$ (LSM) demonstrated a disordered perovskite structure for both the freshly prepared sample produced from calcinations in air, as well as the sample after further treatment in an atmosphere of 10% H_2 in Ar reforming gas at a temperature of 450 °C for 0.5 h. (**Figure. 4.3**). The mismatch in the cation sizes of Ba^{2+} (1.61 Å) and Pr^{3+} (1.286 Å) together with the creation of oxygen vacancies is likely to promote the formation of the double perovskite structure for r-PBM.

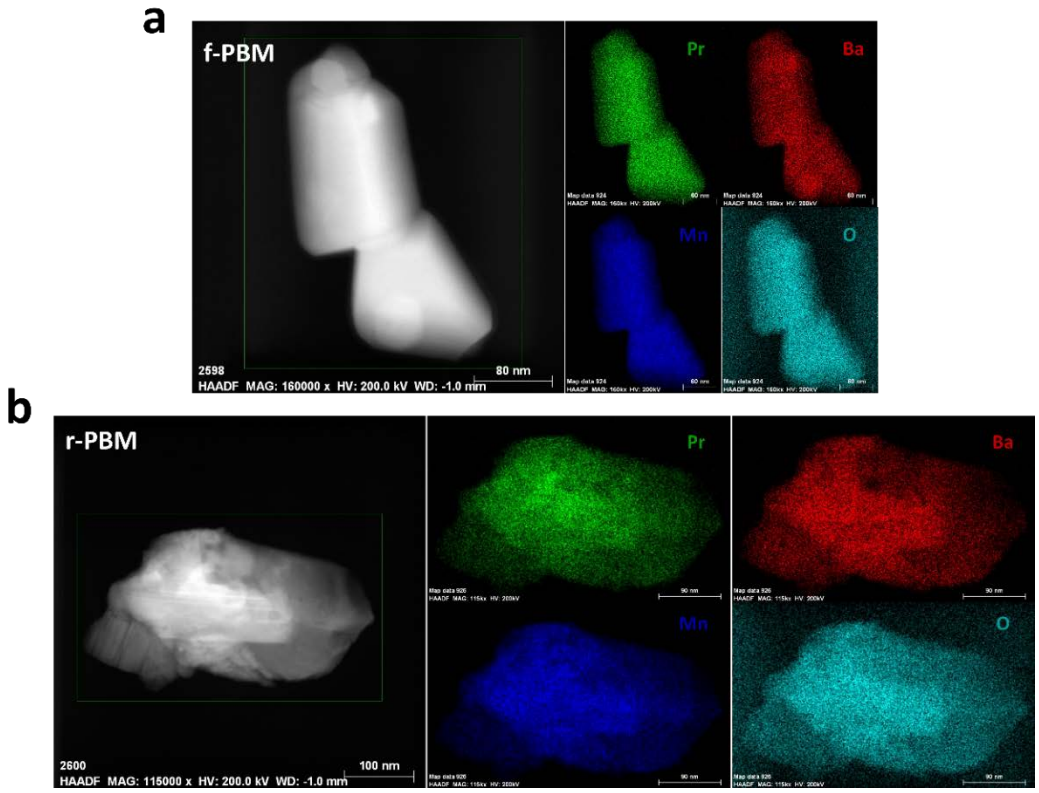

Figure 4.2 The STEM images and EDS-mapping images of a) f-PBM and b) r-PBM.

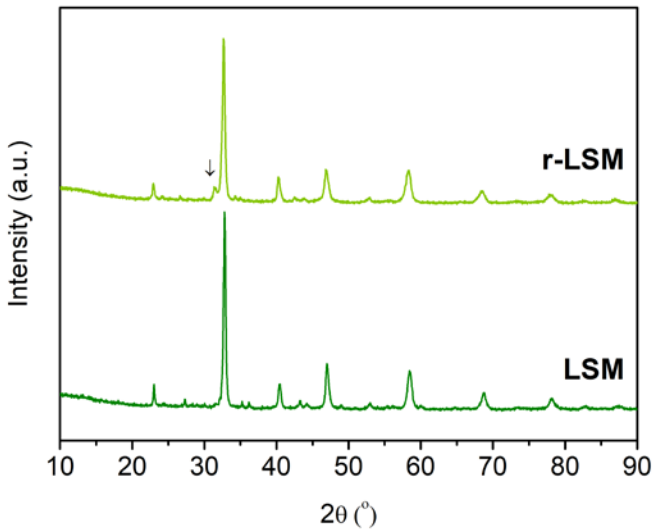

Figure 4.3 X-ray diffraction spectra of LSM and r-LSM. The reduced r-LSM still keep the original rhombohedral structure, however, only an impurity peak which comes from the hexagonal La is detected.

It is generally well accepted that Mn may take on multiple valence states in the perovskite lattice, i.e., 2+, 3+ and 4+.[22-24] Under a reducing hydrogen atmosphere, the

partial reduction of Mn in f-PBM from a higher valence state to a lower valence state is likely to occur, which will induce a change in the tolerance factor and possibly cause a phase transition of $PrBaMn_2O_{6-\delta}$. The successful partial reduction of Mn after the treatment of f-PBM in H_2 atmosphere at 800 °C was confirmed by X-ray photoelectron spectroscopy (XPS), as shown in **Figure 4.4**. For the Mn2p spectrum of fresh f-PBM shown in **Figure 4.4a**, Mn exists as a mixture of Mn^{2+}, Mn^{3+} and Mn^{4+}. The peak at 640.6 eV is assigned to Mn^{2+}, the peak at 641.8 eV is attributed to Mn^{3+}, and that at 642.9 eV corresponds to Mn^{4+}. The atomic ratios of Mn^{2+}, Mn^{3+} and Mn^{4+} based on the integrated area of the corresponding peaks are found to be 0.19: 0.39: 0.42, respectively. Thus, the oxygen vacancy concentration on the surface of f-PBM reaches 0.127 ($\delta = 0.254$). Similarly, the peaks located at 640.9, 641.2 and 642.9 eV in the XPS spectrum of r-PBM (**Figure 4.4b**) are attributed to Mn^{2+}, Mn^{3+} and Mn^{4+}, respectively. The atomic ratios of Mn^{2+}: Mn^{3+}: Mn^{4+} on the surface of r-PBM were found to be 0.28: 0.25: 0.47, with a concomitant oxygen vacancy concentration of 0.157 (δ=0.314) on the surface of sample.

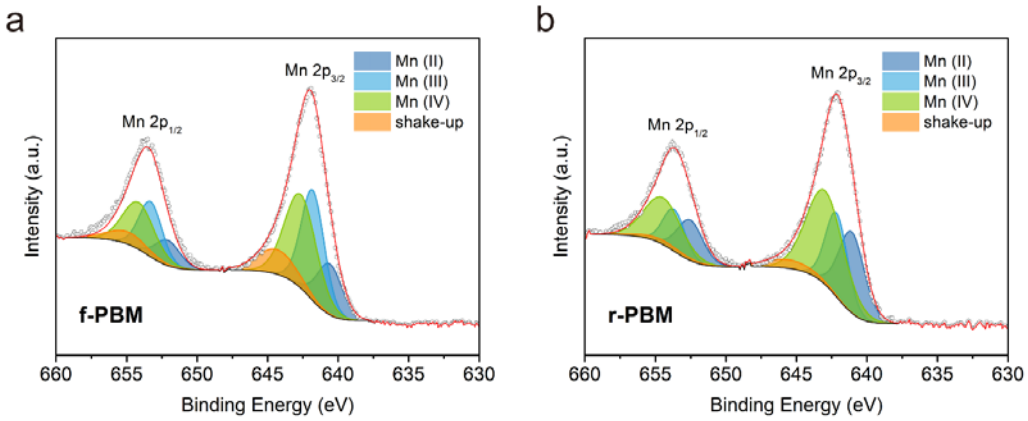

Figure 4.4 High-resolution Mn 2p XPS spectra of a) f-PBM and b) r-PBM and the results of the curve fitting.

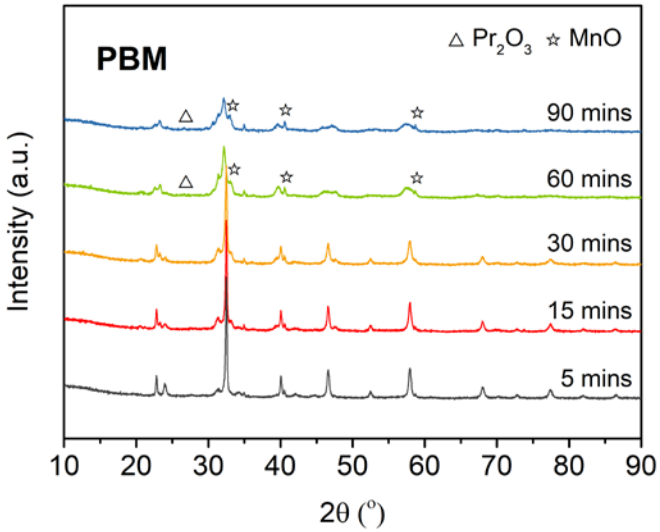

Figure 4.5. The XRD patterns of PBM reduced in the hydrogen atmosphere depending on different time. It shows the conversion from hexagonal to cubic structure with increasing treated time in hydrogen atmosphere. The impurities peaks of Pr_2O_3 and MnO were detected after 60 minutes or longer treatment time.

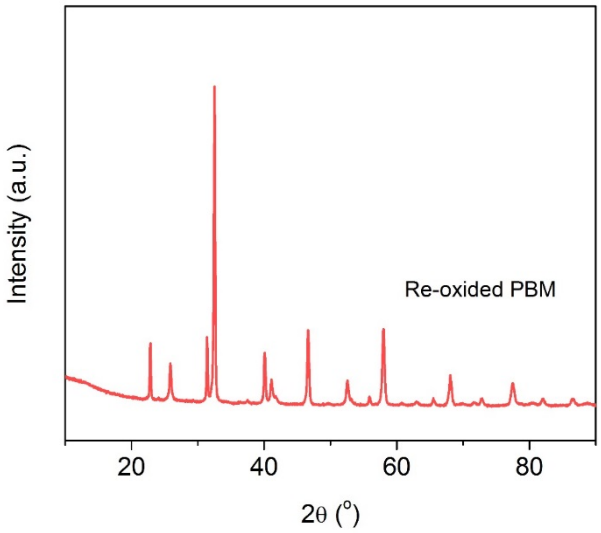

Figure 4.6 X-ray diffraction spectra of r-PBM after the treatment of oxidation. The re-oxided sample displays a mixture of cubic and hexagonal structure.

In order to glean a more thorough understanding of the oxygen vacancy-induced phase transition, f-PBM was treated in hydrogen at 800 °C for different time from 0-90 minutes. The corresponding average oxidation state of Mn was measured precisely by an iodometric titration method, and the phase structure was characterized by *ex situ*

XRD. As illustrated in **Figure 4.5**, the phase structure of f-PBM progressively converted from a mixed cubic/hexagonal structure to a double perovskite structure with increasing treatment time in hydrogen, with a pure double perovskite phase forming after a treatment time of 45 min. Further increases in the treatment time saw the occurrence of impurity phases (Pr_2O_3 and MnO). Correspondingly, according to the results from iodine titration, a steady decrease in oxidation states of Mn is observed with hydrogen treatment time until it reaches an unchanged value with further increase in treatment time. Assuming that a perovskite structure is prevalent for all samples, the oxygen vacancy concentrations were calculated to be 0.125, 0.576, 0.595, 0.672, 0.714, 0.715 and 0.719 for PBM after treatment in H_2 for 0, 5, 15, 30, 45, 60 and 90 minutes, respectively, based on the average oxidation state of Mn. Clearly, the phase transition is induced by the change in the oxidation state of Mn in PBM. Notably, the tolerance factors for various PBM samples are all within the range of 0.75-1.0. This suggests that the valence state of the B-site cation exerts a significant effect on the A-site cation ordering. As shown in **Figure 4.6**, the mixed cubic/hexagonal structure was restored by re-oxidation of the reduced sample in air at 850 °C for 5 h, suggesting highly reversible phase transition behaviour.

4.3.2. Characterization of the electrochemical performance

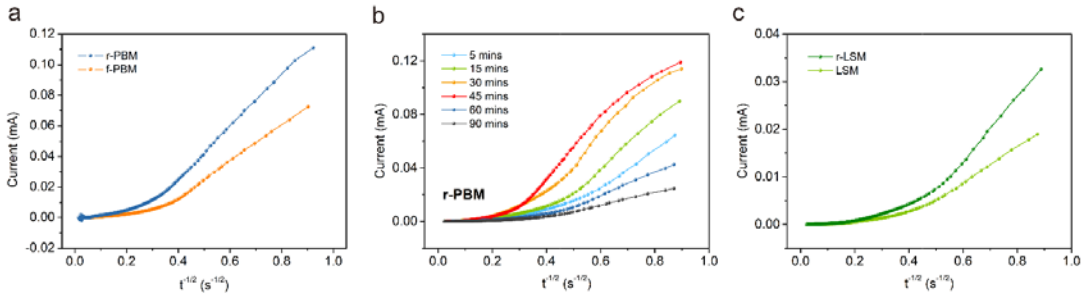

Figure 4.7. Chronoamperometric measurements of the oxygen diffusion rate. a) Current vs. $t^{-1/2}$ curves for f-PBM and r-PBM. b) PBM treated under a reducing atmosphere for different time. c) LSM and r-LSM. The diffusion rate can be measured from the intersection of the linear portion of the current vs. $t^{-1/2}$ with the $t^{-1/2}$ axis.

Table 4.2 The oxygen ion diffusion rates of PBM treated in different time in the 6M KOH electrolyte solution.

Treated time	5 min	15 min	30 min	45 min	60 min	90 min
Oxygen ion diffusion rates (cm^2 s^{-1})	3.1×10^{-12}	7.7×10^{-12}	10.3×10^{-12}	11.9×10^{-12}	4.5×10^{-12}	2.1×10^{-12}

As an intercalation-type electrode for supercapacitors, the energy is stored via the incorporation of oxygen anions into the lattice defects of oxygen vacancies or interatomic spaces.[14] A high oxygen anion diffusion rate within the oxide lattice facilitates the charge storage. If the oxygen anion diffusion rate is sufficiently high, then macro-sized particles can be employed to maximize the pack density and achieve a high volumetric energy density. The oxygen anion diffusion rates inside various PBM samples were measured chronoamperometrically in an aqueous electrolyte consisting of a 6 M KOH solution and based on a three-electrode system with a Pt plate as the counter electrode and a Hg/HgO electrode filled with 1 M KOH as the reference electrode.[25] Here, a contribution of the measured rate could be from the oxygen anion diffusion around the grain boundary or within the oxide lattice. **Figure 4.7b** displays the chronoamperometric measurement of the oxygen anion diffusion rates of PBM samples treated for different time. As shown in **Table 4.2**, the PBM reduced in hydrogen at 800 °C for 45 min (r-PBM) showed the highest oxygen anion diffusion rate with a value of 11.9×10^{-12} cm^2 s^{-1}, which corresponds to the presence of a maximum amount of oxygen vacancies in the r-PBM with a phase-pure A-site cation-ordered double perovskite structure. Any reduction or increase to the treatment time below or above 45 min yielded a lower oxygen anion diffusion rate. This result suggests that both the oxygen vacancies and the double perovskite structure promote oxygen diffusion. The fact that the oxygen diffusion rate of r-PMB is substantially higher than that of f-PBM results from its significantly higher oxygen vacancy concentration and the formation of the double perovskite structure. It has been reported that the oxygen anion diffusion within the ab plane is highly favourable in the A-site cation-ordered perovskite structure.[26, 27] For comparison, fresh and reduced $La_{0.5}Sr_{0.5}MnO_{3-\delta}$ perovskites were also measured with the results shown in **Figure 4.7c**. The results show that r-PBM has a higher oxygen anion diffusion rate than the reduced $La_{0.5}Sr_{0.5}MnO_{3-\delta}$ sample under similar operating conditions. This reinforces our

conclusion that the formation of the unique double perovskite structure is responsible for the enhancement of oxygen anion diffusion inside the r-PBM oxide lattice.

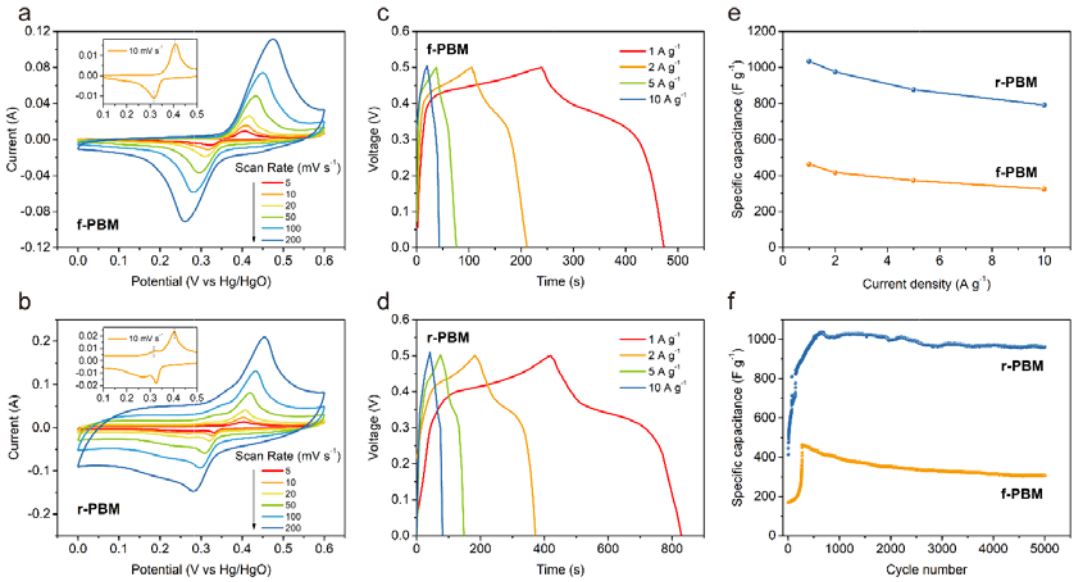

Figure 4.8 Cyclic voltammetry plots of a) f-PBM and b) r-PBM electrodes at a range of scan rates in a potential window of 0.0-0.6 V in a 6 M KOH electrolyte. Galvanostatic charge-discharge profiles of c) f-PBM and d) r-PBM at various current densities in a 6 M KOH aqueous solution. e) The specific capacitance as a function of current density. f) The cycling performance at a current density of 1 A g^{-1} and the cycle number corresponding to cycling time.

To evaluate the potential application of PBM oxides as an oxygen anion-intercalation type supercapacitors electrode, both f-PBM and r-PBM were comparatively studied by cyclic voltammetry (CV) in a 6 M KOH solution with typical results shown in **Figure 4.8a,b**. For an ideal EDLC supercapacitor electrode, a rectangular shape of the CV curve should be observed. However, all CV curves collected for f-PBM and r-PBM deviate significantly from the rectangular shape. Instead, strong redox peaks were observed within the potential window of 0.0-0.6 V (vs. Hg/HgO), indicative of pseudocapacitive behaviour. The CV curves for f-PBM displays only one pair of redox peaks, which was assigned to the Mn^{3+}/Mn^{4+} redox couple. By contrast, the r-PBM clearly displayed two pairs of redox peaks, assigned to the electrochemical reactions between Mn^{2+}/Mn^{3+} and Mn^{3+}/Mn^{4+} that were especially prevalent at low sweep rates. r-PBM achieved higher current densities at corresponding sweep rates, suggesting its higher capacitance. Moreover, r-PBM showed higher peak potentials than f-PBM at

corresponding sweep rates. It is known that a higher oxygen vacancy concentration leads to intercalation redox peaks at higher potentials, as explained by the pseudocapacitive Nernst Equation. These results demonstrate that r-PBM indeed has a higher oxygen vacancy concentration than f-PBM, agreeing well with the iodometric titration results.

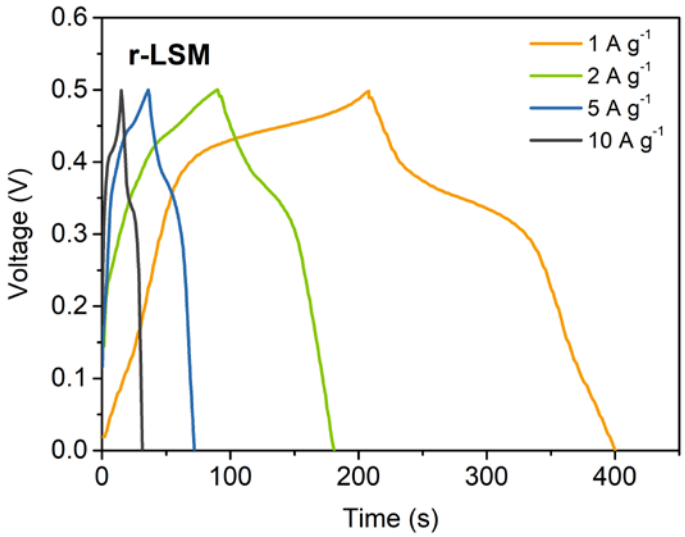

Figure 4.9 Galvanostatic charge-discharge profiles of r-LSM. It reached 386.6, 371.3, 360.2, and 330.7 F g^{-1}, at current densities of 1, 2, 5 and 10 A g^{-1}, respectively.

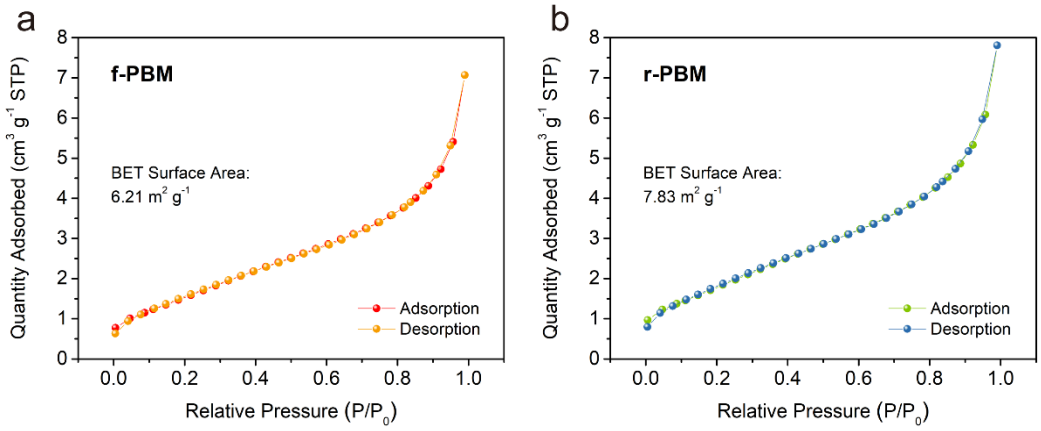

Figure 4.10 N_2 adsorption–desorption spectra of a) f-PBM and b) r-PBM.

Galvanostatic charge-discharge (GCD) measurements were also then performed in the potential window of 0.0-0.5 V (vs. Hg/HgO) to highlight the merits of r-PBM as an anion intercalation-type electrode for supercapacitors (**Figure 4.8c,d**). The tests were conducted in the three-electrode configuration at current densities ranging from 1 to

10 A g^{-1} within a 6 M KOH aqueous electrolyte solution. For comparison, the reduced $La_{0.5}Sr_{0.5}MnO_{3-\delta}$ perovskite oxides were also measured under the same operating conditions. (**Figure 4.9**) As displayed in **Figure 4.8e**, the corresponding specific capacitances of A-site cation-ordered layered r-PBM were calculated to be 1034.8, 974.9, 876.0, and 791.0 F g^{-1} at current densities of 1, 2, 5 and 10 A g^{-1}, respectively, confirming its highly reversible charge storage capability. The capacitance retention of r-PBM still reached 76.5% at 10 A g^{-1} compared with the value at 1 A g^{-1}, which is indicative of it possessing good rate capability. These gravimetric capacitances are comparable to many well-designed nanostructured and porous pseudocapacitive electrodes based on surface Faradaic reactions, such as Co_3O_4, NiO and $NiCo_2O_4$.[5, 28, 29] The better performance of r-PBM over that of r-LSM is clearly related to the higher oxygen vacancy concentration of the former. It should be mentioned that the specific surface area of r-PBM is only 7.83 m^2 g^{-1}, with negligible micro- and mesopores, as shown in **Figure 4.10**. The tap density of the as-prepared r-PBM reached as high as 2.45 g cm^{-3}, suggesting that the volumetric capacitance of r-PBM reached as high as 2535.3 F cm^{-3}. This volumetric capacitance is the highest value reported in the literature at present, demonstrating its superior performance. Finally, the cycling performance of r-PBM was then investigated at a fixed current density of 1 A g^{-1}. As shown in **Figure 4.8f**, the initial gravimetric capacitance of r-PBM reached approximately 445 F g^{-1}, after which increased steadily in the first 600 cycles to reach a maximum value of 1034.8 F g^{-1}. Following this, the capacitance decreased very slowly, retaining a capacitance of approximately 960.8 F g^{-1} even after continuous cycling over 5000 times. Such outstanding performance characteristics are attributed to the A-site layered perovskite structure formed after reduction in a hydrogen atmosphere.

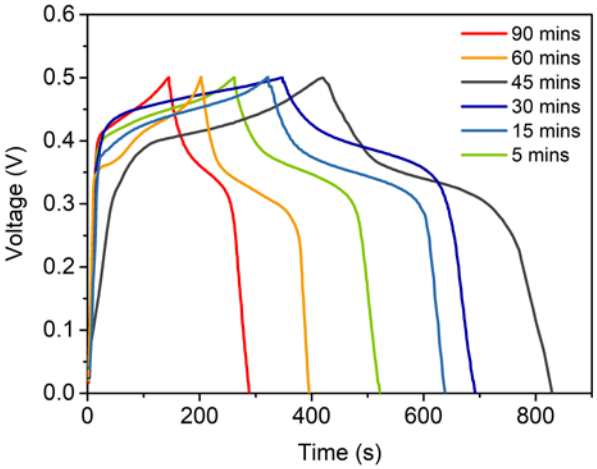

Figure 4.11. Galvanostatic charge-discharge profiles of r-PBM with different reducing treatment time at current densities of 1 A g^{-1}.

In order to determine the best operation conditions for the material as an intercalation-type supercapacitor electrode, GCD measurements were also performed on r-PBM electrodes exposed to hydrogen treatment over different time spans. As shown in **Figure 4.8e**, for the unreduced PBM with a mixed cubic/hexagonal structure, the calculated specific capacitances were 462.3, 416.5, 372.5 and 324.8 F g^{-1} at current densities of 1, 2, 5 and 10 A g^{-1}, respectively. In **Figure 4.11**, the specific capacitances of r-PBM with different treatment times (5, 15, 30, 45, 60, 90 minutes) were 522.7, 630.7, 832.3, 1034.8, 396.3 and 289.9 F g^{-1}, respectively, at current density of 1 A g^{-1}. Clearly, hydrogen treatment over a time span of 45 minutes significantly improved the capacitance of PBM. However, excessive treatment in hydrogen (i.e. longer than 45 minutes) induced inferior electrode performance. The maximum capacitance at treatment time of 45 minutes corresponds well to a maximum oxygen vacancy concentration when the double perovskite structure was formed. With a further increase in treatment time, damage of the double perovskite crystal structure was observed, which leads to a decreasing capacitance. For example, the PBM treated for 5 minutes and 60 minutes displayed similar oxygen vacancy concentrations, however, the specific capacitance of the former was substantially higher than that of the longer treated sample. This further confirms that both the oxygen vacancy concentration and the double perovskite structure are mutually responsible for the excellent charge storage performance of the r-PBM electrode.

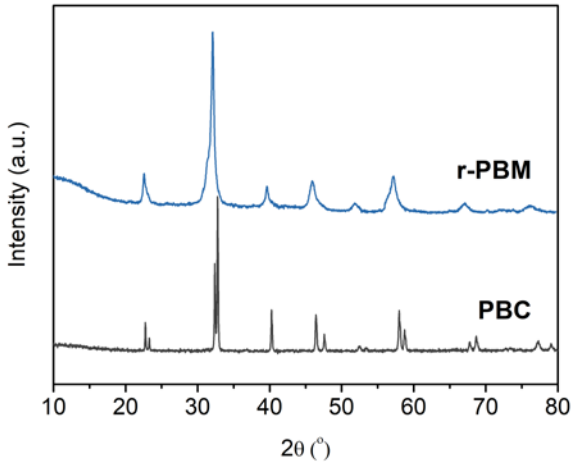

Figure 4.12. X-ray diffraction spectra of r-PBM and PBC after treated in the 6 M KOH solution for one month.

As noted previously, the leaching of cations into the electrolyte solution is of significant concern for the long-term operation of supercapacitors comprising an aqueous alkaline electrolyte.[30] We investigated the potential leaching of Mn from r-PBM in a 6 M KOH solution using two methods. In the first method, 1g of electrode material was soaked in 100 mL of solution at room temperature for 2 months. In the second method, we treated the same amount of electrode material in an autoclave at 100 °C in 100 mL of pure water for 24 h. For comparison, $PrBaCo_{0.5}O_{3-\delta}$ was also tested in the same way. The XRD patterns of the samples after being treated in the KOH solution are displayed in **Figure 4.12**. Both of the samples display their original crystal structure without impurities, demonstrating that r-PBM is able to maintain a stable phase structure in the aqueous alkaline solution. Following the accelerated leaching treatment in the autoclave, the concentration of Mn^{x+} and Co^{x+} cations in the mother liquor were measured via inductively coupled plasma-optical emission spectroscopy (ICP-OES). The concentration of Co^{x+} for $PrBaCo_{0.5}O_{3-\delta}$ was determined to be 0.131 mg L^{-1}. This value is significantly higher than the concentration of Mn^{x+} of 0.027 mg L^{-1} in the r-PBM mother liquor, demonstrating that Mn leaching is much less significant than cobalt leaching.

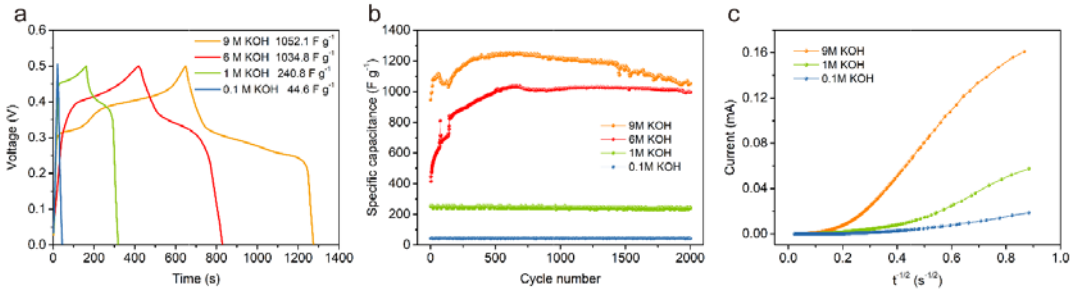

Figure 4.13. a) Galvanostatic charge-discharge profiles of r-PBM. b) The cycling performance of r-PBM at a current density of 1A g^{-1}. c) Current vs. $t^{-1/2}$ curves of r-PBM in different concentrations of the KOH electrolyte solution.

One of the important advantages associated with the use of an oxygen anion-intercalation electrode is that very high OH^- electrolyte concentrations can be achieved due to the high solubility of KOH in water and its strong basic properties. This exerts a favourable effect in minimizing the oxygen anion diffusion ohmic resistance in the electrolyte whilst also maximizing the interfacial reaction between the electrode and electrolyte. Four different KOH concentrations of 0.1, 1, 6 and 9 M were investigated in order to examine the effect of KOH concentration on the electrode intercalation behaviour. The GCD curves of the r-PBM electrode in different concentrations of the KOH electrolyte solution are presented in **Figure 4.13a**. A significant increase in capacitance was observed with the increase in the KOH concentration. For example, at 1 A g^{-1} current density, the capacitance was 44.6, 240.8, 1034.8 and 1252.1 F g^{-1} for the PBM electrode in 0.1, 1, 6 and 9 M KOH electrolyte, respectively. **Figure 4.13b** displays the cycling performance of r-PBM in the various KOH electrolyte solutions. All of the samples retained more than 90% specific capacitance after 2000 cycles. Finally, **Figure 4.13c** presents the measured oxygen anion diffusion rates, with values of 14.7×10^{-12}, 1.8×10^{-12} and 0.3×10^{-12} cm^2 s^{-1} observed for measurements conducted in 9 M KOH, 1 M KOH and 0.1 M KOH electrolyte solutions, respectively. These results suggest that an increase in the OH^- concentration enhances the oxygen anion diffusion rate in the PBM oxide lattice.

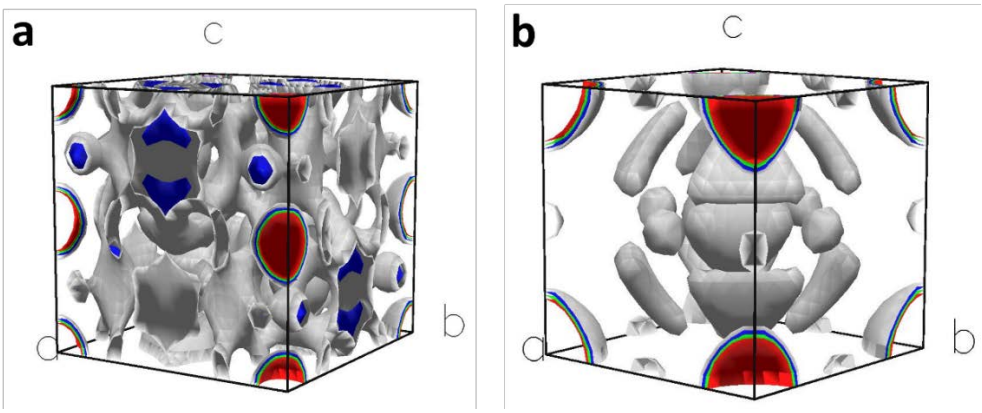

Figure 4.14 3D electron density map of hexagonal with space group of *P6$_3$mc* and cubic structure with space group of *Pm-3m*. The maps were built up based on the results of X-ray diffraction Rietveld refinement

Based on the above analysis, reduced PBM is demonstrated to be an excellent intercalation-type supercapacitor electrode with a superior capacitance compared against $La_{0.5}Sr_{0.5}MnO_{3-\delta}$ perovskite oxide materials. The theoretical capacitance of a perovskite oxide is dependent on the amount of accessible oxygen intercalation sites inside the oxide lattice within the operation potential window. r-PBM was shown to possess a significantly larger oxygen vacancy concentration than the reduced $La_{0.5}Sr_{0.5}MnO_{3-\delta}$ perovskite. It was also shown to yield a higher oxygen diffusion rate than $La_{0.5}Sr_{0.5}MnO_{3-\delta}$ at room temperature. Both factors likely account for the better performance of r-PBM compared to r-LSM. For oxygen anion-intercalation electrodes used in energy storage, the oxygen anions incorporated into an oxide lattice may occupy the available oxygen vacancy sites or enter as interstitial species. As lattice defects, oxygen vacancies can be created via a doping strategy. The doping of Ba^{2+} with a lower valence state to the Pr^{3+} site in $PrMnO_3$ could either cause the creation of oxygen vacancies inside the oxide lattice or, alternatively, lead to an increase in the valence state of Mn in the B site to maintain the overall electric neutrality of the oxide. Clearly, charge neutrality under a reducing atmosphere is compensated more preferably through the creation of oxygen vacancies. The 3D electron density maps for the *P6$_3$mc* and *Pm-3m* phases of perovskite as obtained from the Rietveld refinement results are shown in **Figure 4.14**. The *P6$_3$mc* phase is shown to have an overlap of the electron cloud between different elements, significantly larger than that of the double layered structure. This suggests that facile charge compensation is achieved through a change in the oxidation state of the Mn element in the B site. The relatively small

overlap of the electron cloud observed in the double perovskite structure is beneficial for the creation of oxygen vacancies. Under a hydrogen reducing atmosphere, the compensation for electric neutrality arising from Ba^{2+} doping occurs mainly through the creation of oxygen vacancies in the r-PBM, as supported by the high oxygen vacancy concentration measured by the iodine titration method. Based on the measured capacitance after the charging process, the final composition of r-PBM was $PrBaMn_2O_{6+0.82}$. This suggests the partial oxygen is also present as interstitial oxygen anions in the r-PBM lattice, and the surface electron storage contributes to the total capacitance, as well during the charge process. Comparatively, only 11.7% of oxygen per unit was accessible in r-LSM during the charge-discharge processes. In addition, the formation of a specific layered structure in the highly oxygen-mobile PrOx provided r-PBM with an oxygen diffusion rate substantially higher than r-LSM. Consequently, r-PBM demonstrated a large capacitance even for the sample comprising a dense and coarse particle morphology.

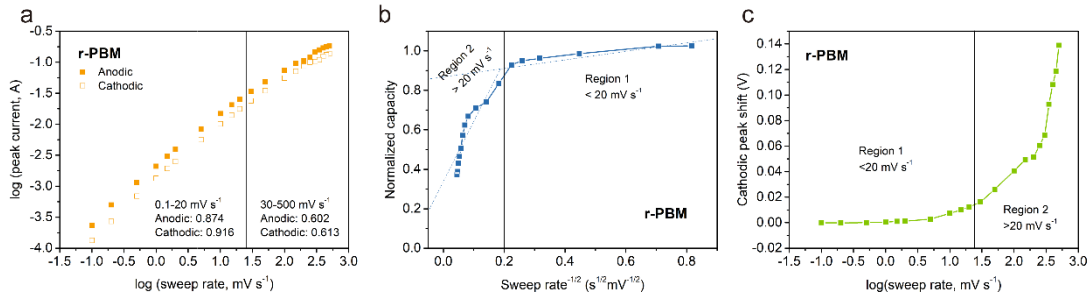

Figure 4.15. a) The b-value determination based on the redox peak currents indicated that this value was close to 1 up to 30 mV s^{-1}, proving that charge storage is capacitive even at the highest currents. b) Capacity versus $v^{-1/2}$ curves can separate the contributions from the diffusion-controlled capacity and capacitive-controlled capacity; two distinct kinetics regions were created by the CV sweep rate from 1 to 500 mV s^{-1}. The dashed lines represent the fitted lines of the infinite sweep rate capacitance using the capacity. c) The intercalation kinetics was also investigated by the cathodic peak shift, which is divided into two regions by the CV sweep rates.

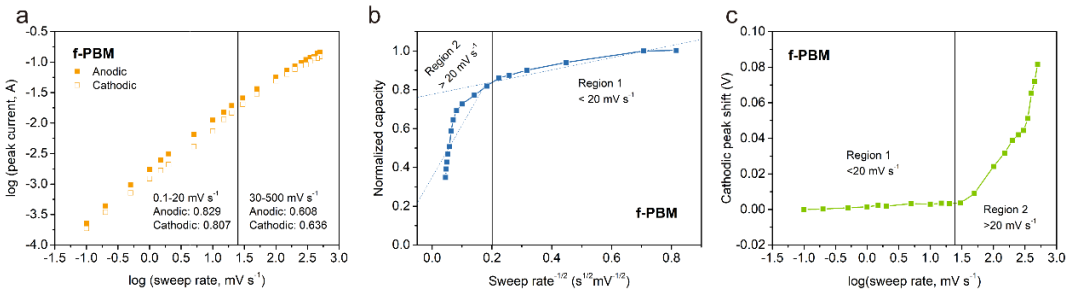

Figure 4.16. a) b-value determination of the peak anodic and cathodic currents shows that this value is approximately 1 up to 30mV s^{-1}. b) Capacity versus $v^{-1/2}$ allows for the separation of diffusion-controlled capacity from capacitive-controlled capacity. c) The variation of the cathodic peak voltage with the sweep rate exhibits a region of small peak separation followed by increased separation at 20mV s^{-1}.

It is possible that both surface Faradaic reactions and bulk intercalation reactions may occur in parallel during energy storage in intercalation-type supercapacitors. The basic charge mechanism in the r-PBM electrode can be interrogated by the plots of log(i) versus log(v) based on the CV scan rates from 0.1 to 500 mV s^{-1} for the anodic and cathodic peaks (**Figure 4.15a** and **Figure 4.16a)**. The b factor values for both anodic and cathodic currents were determined to be 0.829 and 0.807, respectively, for the f-PBM electrode, and 0.874 and 0.916, respectively, for the r-PBM electrode at scan rates from 0.1 to 20 mV s^{-1}. The b factor for anodic and cathodic currents at scan rates from 30 to 500 mV were 0.608 and 0.636, respectively, for the f-PBM electrode and 0.602 and 0.613, respectively, for the r-PBM electrode. These results suggest that at relatively low scan rates, the f-PBM and r-PBM electrodes are mainly rate-limited by the low surface process. In other words, the oxygen anion diffusion rate under polarization conditions in f-PBM and r-PBM electrodes are still sufficiently high. In addition to this, the rate-limiting step of a charge-storage mechanism can be further understood by examining the relationship between capacity and sweep rate.[31] In **Figure 4.15b** and **Figure 4.16b**, the fitted *y*-intercept represents the infinite scan rate capacitance in the range below 20 mV s^{-1}. In this region, the capacity is largely independent of sweep rate. However, in the region beyond 20 mV s^{-1}, the decrease of capacity with $v^{-1/2}$ follows a linear pattern, demonstrating that diffusion-controlled charge storage plays a dominant role at high sweep rates. Hence, diffusion is rate-limiting under the condition of high-speed charging, but there is no evidence for diffusion limitations at low-speed charging. As presented in **Figure 4.15c** and **Figure**

4.16c, region 1 exhibits capacitive behaviour causing a slight shift in the peak potential (< 0.05 V), suggesting that insertion of O^{2-} is facile due to a slow diffusion-controlled process.[10]

4.3.3. Mechanism of oxygen intercalation into the r-PBM electrode

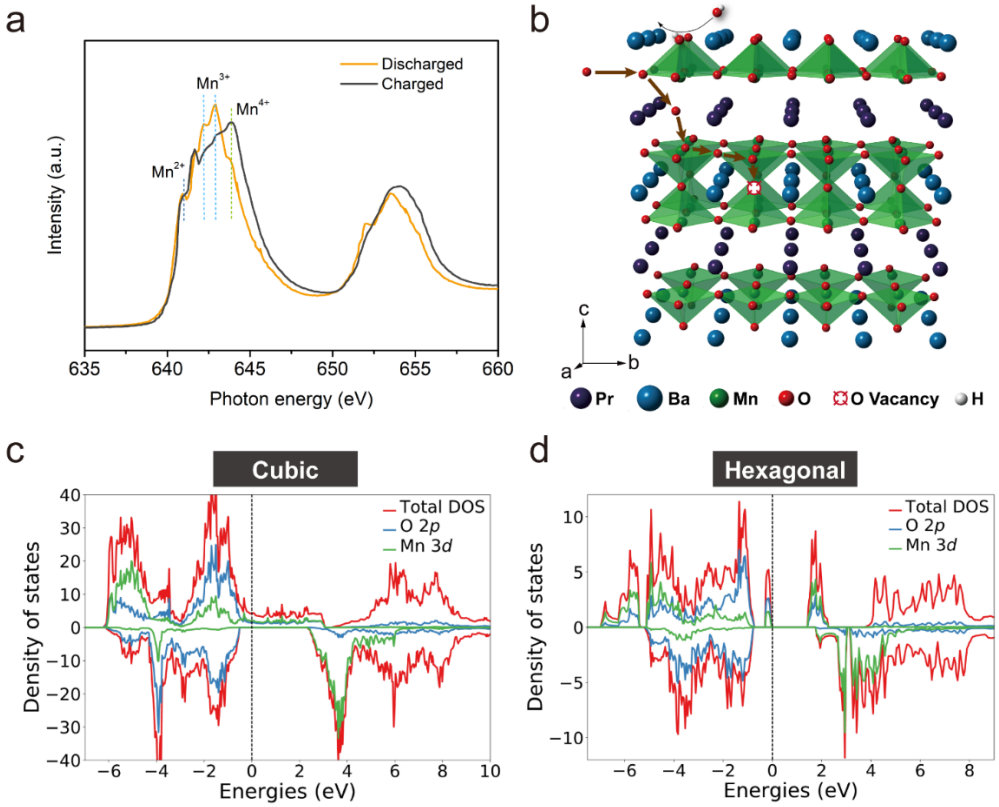

Figure 4.17. a) NEXAFS spectra measured at the Mn 2p adsorption edge (Mn L-edge). b) A schematic diagram of oxygen intercalation into r-PBM during the energy storage process. DFT+U calculated density of states (DOS) for c) cubic and d) hexagonal PBM.

To thoroughly explore the reaction mechanism of oxygen intercalation into the r-PBM electrode, charged and discharged r-PBM electrodes were measured by *ex situ* near-edge X-ray adsorption fine structure (NEXAFS) at the Soft X-ray Beamline of the Australian Synchrotron. **Figure 4.17a** presents Mn L-edge NEXAFS spectra of both charged and discharged r-PBM electrodes. The Mn L-edge is split into two separate multiplets, namely, the L_3-edge located between 640 eV and 645 eV, and the L_2-edge at 650-655 eV. The appearance of two multiplets is ascribed to the spin-orbit interaction of the Mn $2p_{3/2}$ and $2p_{1/2}$ core states.[32] The rich fine structure resulting from the multiplet splitting reflects the transitions into the unoccupied 3d orbitals, and as such, is highly sensitive to the local chemical environment. Hence, NEXAFS is

highly suited to probing Mn valence as it provides clear information compared with the Mn 2p core-level spectra recorded via XPS, which has to be evaluated with a degree of caution.[33-36] It is evident from the spectra that the charged r-PBM electrode contains a mixture of predominantly Mn^{4+} but also Mn^{3+}. This observation is based on comparisons of the NEXAFS data with reference spectra for Mn^{2+}, Mn^{3+} and Mn^{4+} reported in the literature.[33, 37] When compared with the discharged electrode, the L_3 peak undergoes a shift to a lower energy, indicative of a decrease in the formal Mn valence. A similar observation is made with the L_2 edge. Accordingly, stronger contributions from Mn^{2+} and Mn^{3+} were clearly apparent after the electrode was discharged. The results suggest that the mechanism of the oxygen intercalation process for energy storage can be described as the following equations:

$$PrBa\left[Mn_{2\delta}^{2+}; Mn_{2-2\delta}^{3+}\right]O_{6-\delta} + 2\delta OH^- \leftrightarrow PrBaMn_2^{3+}O_{6-\delta} + 2\delta e^- + \delta H_2O \qquad (4.1)$$

$$PrBaMn_2^{3+}O_{6-\delta} + 2\delta OH^- \leftrightarrow PrBa\left[Mn_{2\delta}^{4+}; Mn_{2-2\delta}^{3+}\right]O_{6+\delta} + 2\delta e^- + H_2 \qquad (4.2)$$

The schematic diagram of this intercalation mechanism is displayed in **Figure 4.17b**. The oxygen ions are intercalated into the crystal lattice by occupation of the oxygen vacancies, and partial oxygen ions diffuse along the pathway at the edges through the lattice, subsequently accompanied by the oxidation of Mn^{2+} to Mn^{3+}. Afterwards, other additional oxygen ions are adsorbed on the surface of the crystal by Mn ion diffusion and further oxidation of Mn^{3+} to Mn^{4+}.

The above results are also supported by density functional theory (DFT) calculations. As derived from XRD results, the freshly prepared f-PBM in air comprises hexagonal and cubic phases, while the reduced r-PBM exhibits a pure cubic double perovskite phase. DFT calculations were employed to provide further insights into the oxygen vacancy formation in f-PBM and r-PBM. The oxygen vacancy formation energies for cubic and hexagonal f-PBM were 2.19 eV and 2.93 eV, respectively. These results indicate that it is somewhat easier to form an oxygen vacancy in cubic PBM than it is in the hexagonal phase. We therefore predict that the oxygen vacancy concentration in the cubic PBM is higher than that in the hexagonal phase, which is consistent with our experimental observations that δ=x in the cubic phase was larger than δ=y in the hexagonal phase. In **Figure 4.17c**, it is shown that orbitals crossed the fermi level in terms of the total density of states (DOS), which arises from the hybridization of Mn 3d and O 2p orbitals, demonstrating its metallic character in the ground state. In

contrast, in **Figure 4.17d** we observe a small band gap of 1.39 eV in the DOS of the hexagonal phase, implying it possesses poor electronic conductivity compared with the cubic phase.

4.4. Conclusions

In summary, we have demonstrated that the reduction of PBM in a hydrogen atmosphere at 850 ^{o}C leads to a phase transition from a mixture of hexagonal and cubic phases to a cubic phase for PBM. The introduction of a higher oxygen vacancy concentration into the r-PBM lattice after reduction results in improved electrochemical properties, especially the intercalation pseudocapacitive charge storage. As demonstrated by the experimental results and DFT calculations, the formation of a layered double perovskite structure after hydrogen reduction over an optimal time of 45 minutes was found to significantly increase both the oxygen vacancy concentration and the oxygen anion diffusion rate, in turn contributing to the outstanding capacitance. We therefore believe that the above findings provide a useful guideline for the design of perovskite oxides as high-performance oxygen anion-intercalation electrodes for supercapacitors.

4.5. Reference

[1] P. Simon, Y. Gogotsi, B. Dunn, Science 2014, 343, 1210.

[2] N. Jha, P. Ramesh, E. Bekyarova, M. E. Itkis, R. C. Haddon, Adv. Energy Mater. 2012, 2, 438.

[3] J. Yan, Z. Fan, W. Sun, G. Ning, T. Wei, Q. Zhang, R. Zhang, L. Zhi, F. Wei, Adv. Funct. Mater. 2012, 22, 2632.

[4] P. Simon, Y. Gogotsi, Nat. Mater. 2008, 7, 845.

[5] Y. Liu, Z. Wang, Y. Zhong, M. Tade, W. Zhou, Z. Shao, Adv. Funct. Mater. 2017, 1701229.

[6] G. Zhang, X. W. Lou, Adv. Mater. 2013, 25, 976.

[7] L. Shen, Q. Che, H. Li, X. Zhang, Adv. Funct. Mater. 2014, 24, 2630.

[8] M. R. Lukatskaya, O. Mashtalir, C. E. Ren, Y. Dall'Agnese, P. Rozier, P. L. Taberna, M. Naguib, P. Simon, M. W. Barsoum, Y. Gogotsi, Science 2013, 341, 1502.

[9] L. Kong, C. Zhang, J. Wang, W. Qiao, L. Ling, D. Long, ACS Nano 2015, 9, 11200.

[10] V. Augustyn, J. Come, M. A. Lowe, J. W. Kim, P.-L. Taberna, S. H. Tolbert, H. D. Abruña, P. Simon, B. Dunn, Nat. Mater. 2013, 12, 518.

[11] B. Hao, Y. Yan, X. Wang, G. Chen, ACS Appl. Mater. Interfaces 2013, 5, 6285.

[12] H.-S. Kim, J. B. Cook, H. Lin, J. S. Ko, S. H. Tolbert, V. Ozolins, B. Dunn, Nat. Mater. 2017, 16, 454.

[13] T. Kudo, H. Obayashi, T. Gejo, J. Electrochem. Soc. 1975, 122, 159.

[14] J. T. Mefford, W. G. Hardin, S. Dai, K. P. Johnston, K. J. Stevenson, Nat. Mater. 2014, 13, 726.

[15] L. Zhu, Y. Liu, C. Su, W. Zhou, M. Liu, Z. Shao, Angew. Chem. Int. Ed. 2016, 128, 9728.

[16] S. Choi, S. Yoo, J. Kim, S. Park, A. Jun, S. Sengodan, J. Kim, J. Shin, H. Y. Jeong, Y. Choi, G. Kim, M. Liu, Sci. Rep. 2013, 3, 2426.

[17] A. Chroneos, B. Yildiz, A. Tarancon, D. Parfitt, J. A. Kilner, Energy Environ. Sci. 2011, 4, 2774.

[18] Y. H. Huang, R. I. Dass, Z. L. Xing, J. B. Goodenough, Science 2006, 312, 254.

[19] G. Kim, S. Wang, A. J. Jacobson, L. Reimus, P. Brodersen, C. A. Mims, J. Mater. Chem. 2007, 17, 2500.

[20] M. Burriel, J. Peña-Martínez, R. J. Chater, S. Fearn, A. V. Berenov, S. J. Skinner, J. A. Kilner, Chem. Mater. 2012, 24, 613.

[21] S. Sengodan, S. Choi, A. Jun, T. H. Shin, Y.-W. Ju, H. Y. Jeong, J. Shin, J. T. S. Irvine, G. Kim, Nat. Mater. 2015, 14, 205.

[22] Y. Y. Huang, T. S. Zhao, G. Zhao, X. H. Yan, K. Xu, J. Power Sources 2016, 304, 74.

[23] E. S. Ilton, J. E. Post, P. J. Heaney, F. T. Ling, S. N. Kerisit, Appl. Surf. Sci. 2016, 366, 475.

[24] Z. Huang, W. Zhou, C. Ouyang, J. Wu, F. Zhang, J. Huang, Y. Gao, J. Chu, Sci. Rep. 2015, 5, 10899.

[25] J. T. Mefford, X. Rong, A. M. Abakumov, W. G. Hardin, S. Dai, A. M. Kolpak, K. P. Johnston, K. J. Stevenson, Nat. Commun. 2016, 7, 11053.

[26] C. Chen, D. Chen, F. Ciucci, Phys. Chem. Chem. Phys. 2015, 17, 7831.

[27] B. P. Uberuaga, G. Pilania, Chem. Mater. 2015, 27, 5020.

[28] S. Xiong, C. Yuan, X. Zhang, B. Xi, Y. Qian, Chem. Eur. J. 2009, 15, 5320.

[29] Q. Lu, M. W. Lattanzi, Y. Chen, X. Kou, W. Li, X. Fan, K. M. Unruh, J. G. Chen, J. Q. Xiao, Angew. Chem. Int. Ed. 2011, 123, 6979.

[30] Y. Liu, J. Dinh, M. O. Tade, Z. Shao, ACS Appl. Mater. Interfaces 2016, 8, 23774.

[31] S. Ardizzone, G. Fregonara, S. Trasatti, Electrochim. Acta 1990, 35, 263.

[32] D. Mierwaldt, S. Mildner, R. Arrigo, A. Knop-Gericke, E. Franke, A. Blumenstein, J. Hoffmann, C. Jooss, Catalysts 2014, 4.

[33] K. Mette, A. Bergmann, J.-P. Tessonnier, M. Hävecker, L. Yao, T. Ressler, R. Schlögl, P. Strasser, M. Behrens, ChemCatChem 2012, 4, 851.

[34] S. P. Cramer, F. M. F. DeGroot, Y. Ma, C. T. Chen, F. Sette, C. A. Kipke, D. M. Eichhorn, M. K. Chan, W. H. Armstrong, J. Am. Chem. Soc. 1991, 113, 7937.

[35] M. C. Biesinger, L. W. M. Lau, A. R. Gerson, R. S. C. Smart, Appl. Surf. Sci. 2010, 257, 887.

[36] M. C. Biesinger, B. P. Payne, A. P. Grosvenor, L. W. M. Lau, A. R. Gerson, R. S. C. Smart, Appl. Surf. Sci. 2011, 257, 2717.

[37] A. Saywell, G. Magnano, C. J. Satterley, L. M. A. Perdigão, A. J. Britton, N. Taleb, M. del Carmen Giménez-López, N. R. Champness, J. N. O'Shea, P. H. Beton, Nat. Commun. 2010, 1, 75.

[38] F. R. Van Buren, G. H. J. Broers, A. J. Bouman, C. Boesveld, J. Electroanal. Chem. Interfacial Electrochem. 1978, 87, 389.

[39] F. R. Van Buren, G. H. J. Broers, A. J. Bouman, C. Boesveld, J. Electroanal. Chem. Interfacial Electrochem. 1978, 88, 353.

[40] A. G. C. Kobussen, F. R. van Buren, G. H. J. Broers, J. Electroanal. Chem. Interfacial Electrochem. 1978, 91, 211.

[41] B. C. C. Cowie, A. Tadich, L. Thomsen, AIP Conf. Proc. 2010, 1234, 307.

[42] E. Gann, C. R. McNeill, A. Tadich, B. C. C. Cowie, L. Thomsen, J. Synchrotron Radiat. 2016, 23, 374.

[43] G. Kresse, J. Furthmüller, Phys. Rev. B 1996, 54, 11169.

[44] P. E. Blöchl, Phys. Rev. B 1994, 50, 17953.

[45] J. P. Perdew, K. Burke, M. Ernzerhof, Phys. Rev. Lett. 1996, 77, 3865.

[46] S. L. Dudarev, G. A. Botton, S. Y. Savrasov, C. J. Humphreys, A. P. Sutton, Phys. Rev. B 1998, 57, 1505.

[47] L. Wang, T. Maxisch, G. Ceder, Phys. Rev. B 2006, 73, 195107.

Every reasonable effort has been made to acknowledge the owners of copyright material. I would be pleased to hear from any copyright owner who has been omitted or incorrectly acknowledged.

Chapter 5 Molecular design of mesoporous $NiCo_2O_4$ and $NiCo_2S_4$ with submicron-polyhedron architectures for efficient pseudocapacitive energy storage[§]

Abstract

Spinel-type $NiCo_2O_4$ (NCO) and $NiCo_2S_4$ (NCS) polyhedron architectures with sizes of 500-600 nm and rich mesopores with diameters of 1-2 nm are prepared facilely by the molecular design of Ni and Co into polyhedron-shaped zeolitic imidazolate frameworks (ZIFs) as solid precursors. Both as-prepared NCO and NCS nanostructures exhibit excellent pseudocapacitance and stability as electrodes in supercapacitors. In particular, the exchange of O^{2-} in the lattice of NCO with S^{2-} obviously improves the electrochemical performance. NCS shows a highly attractive capacitance of 1296 F g^{-1} at a current density of 1 A g^{-1}, ultrahigh rate capability with 93.2% capacitance retention at 10 A g^{-1}, and excellent cycling stability with a capacitance retention of 94.5 % after cycling at 1 A g^{-1} for 6000 times. The asymmetric supercapacitor with an NCS negative electrode and an active carbon positive electrode delivers very attractive energy density of 44.8 Wh kg^{-1} at power density 794.5 W kg^{-1}, and a favourable energy density of 37.7 Wh kg^{-1} is still achieved at a high power density of 7981.1 W kg^{-1}. The specific mesoporous polyhedron architecture contributes significantly to the outstanding electrochemical performances of both NCO and NCS for capacitive energy storage.

[§]*Reprinted (adapted) with permission from (Y. Liu, Z.B. Wang, Y.J. Zhong, M.O. Tadé, W. Zhou, Z.P. Shao, Molecular design of mesoporous $NiCo_2O_4$ and $NiCo_2S_4$ with submicron-polyhedron architectures for efficient pseudocapacitive energy storage, Adv. Funct. Mater. 2017, 27, 1701229). Copyright (2017) John Wiley and Sons.*

5.1 Introduction

With rapid growth of the world's population and continuous expansion in global economy, a fast increase in the application of energy-based appliances has been envisioned, which ultimately will lead to a quick increase in the energy consumption rate. Currently, advanced energy-conversion and storage technologies have rapidly developed that can facilitate the use of renewable energies, such as solar power, biomass and wind energy, which are important for the healthy and sustainable development of our society. Supercapacitors are one of the most important electrochemical energy storage devices, which possess some highly attractive properties such as ultrahigh power density (up to ~10 000 Wkg^{-1}), short charging times (in the order of tens of seconds), and long lifetime over repeated charge-discharge cycles (>100 000 cycles). Supercapacitors have many potential applications, such as frequency regulation in smart grids and power sources for hybrid-electric vehicles. The improvement of energy density with no significant sacrifice in power density and cycle lifetime plays a key role in realizing the wide applications of supercapacitors in the abovementioned important fields.[1-3]

Pseudo-capacitors are an important type of electrochemical capacitor that store energy through surface Faradaic reactions. Compared to supercapacitors with carbon based electrode materials, whose mechanism based on double layer ion-adsorption, pseudo-capacitors show much higher capacitance, which have received considerable attention during the past decade.[4, 5] However, the Faradaic reactions typically are much slower in rate than ion adsorption over carbon surfaces. Thus, the rate capability is a big concern for the development of supercapacitors based on pseudo-capacitance. On the other hand, the Faradic reaction is usually associated with a noticeable volume change, which may cause a detrimental effect on the cycling stability of the pseudo-capacitive electrode. An increase of the surface area and the rational design of mesoporous electrode architectures are strategies to increase the capacitance of pseudo-capacitive electrodes. In addition, the increase of intrinsic conductivity of the electrode material is also helpful in improving the rate capability. Development of appropriate techniques for the facile fabrication of electrode materials with the abovementioned properties is critical to realize high-performance pseudo-capacitors.

Metal-organic frameworks (MOFs), initially given a definition by Yaghi and co-workers in 1995,[6] are a class of porous functional materials. MOFs have several important properties, including extraordinarily light weight (apparent density as low as 0.13 g cm^{-3}), large pore volume, tuneable pore size and clear pore size distribution, superior specific surface area (up to 10,000 m^2 g^{-1}), and high flexibility of the material composition.[7] More significantly, the properties and performance of MOFs can be tailored through molecular design. During the past two decades, tremendous research activities have been conducted on MOFs towards potential applications in catalysis, drug delivery, and gas storage and separation.[8-10] More recently, the application of MOFs in electrochemical energy storage has also attracted much attention, either as a direct energy material or as a precursor for developing oxide or carbon-based electrode materials for supercapacitors, lithium-ion batteries (LIBs), and water electrolysers.[8, 11, 12] By incorporating pseudocapacitive redox centers, MOFs can be directly utilized as a new kind of electrode material for supercapacitors directly. For example, a Co-based MOFs was demonstrated to possess a capacitance of nearly 200 F g^{-1} in a LiOH electrolyte solution.[13] However, owing to their low electrical conductivity and steric hindrance to ion insertion due to the insufficient pore size and incompatibility between MOFs and the electrolyte, it is a big challenge for the direct use of MOFs as supercapacitor electrodes. Instead, the use of MOFs as precursors for the preparation of porous metal oxides or carbon as supercapacitor electrodes have been much frequently exploited, as attracted by the rich compositional flexibility of MOFs and large surface areas.[14, 15] Several attempts for the preparation of mesoporous metal oxides derived from MOFs electrodes for pseudo-capacitive supercapacitors have been made.[11, 16] Recently, a newly emerged sub-family of MOFs, i.e., zeolitic imidazole frameworks (ZIFs), which are topologically isomorphic with zeolites, has attracted considerable attention as a platform for the development of new electrochemical energy materials, including electrode materials for supercapacitors.[17] A mesoporous cobalt oxide polyhedral nanostructure, for instance, developed from the thermal decomposition of a cobalt-containing ZIFs organic framework, was exploited as an electrode material for supercapacitors, showing modest specific capacitance of 270 F g^{-1} at a current density of 2 A g^{-1}.[18] Nevertheless, metal oxides from MOFs still have unsatisfactory electrochemical performance so far, leaving substantial room for further improvement.

Up until now, transition-metal sulphides with promising performance have been a potential great type of electrode material for supercapacitors. For example, CoS_2 ellipsoids, accompanied by anisotropic tube-like cavities and prepared by a hydrothermal preparation, demonstrated a high specific capacitance of 980 F g^{-1} at a current density of 1 A g^{-1}.[19] Meanwhile, a flaky Ni_3S_2 electrode synthesized by a potentiodynamic deposition technique displayed a reversible capacitance of 717 F g^{-1} at a current density of 2 A g^{-1}.[20] Similarity to binary Ni-Co oxides, the formation of binary Ni-Co sulphides may also be beneficial to improve capacitance as compared with the respective nickel sulphide and cobalt sulphide.[21-23] Indeed, it was reported that $NiCo_2S_4$ (NCS) prepared by a hydrothermal method possessed higher electrochemical activity than the respective mono-metal sulphides.[24] Compared to binary Ni-Co oxides, the binary Ni-Co sulphides possess much higher conductivity. For example, the electrical conductivity of NCS was reported to be at least two orders of magnitude greater than that of $NiCo_2O_4$ (NCO).[25] Up to now, a variety of NCS nanostructures, including microspheres,[24], nanotubes,[26] nanoprisms,[27] and nanoplates,[28] have been successfully prepared in recent years, exhibiting promising performance in electrochemical application; however, no reports on the preparation of NCO and NCS polyhedrons from ZIF-67 towards the application of electrodes in supercapacitors are available in previous literatures.

In this current work, we report the successful preparation of mesoporous polyhedron-structured NCO and NCS nanoparticles by molecular design of Ni and Co bimetallic ZIFs as solid precursors. The as-prepared samples (ZIF-NCO and ZIF-NCS) were applied as electrodes of supercapacitors, demonstrating ultrahigh electrochemical performance. In particular, the NCS nanostructure showed very attractive electrochemical performance in supercapacitors, among the highest performance reported in the literature. The advances in this study greatly extend the potential application of MOFs in high-power energy storage applications.

5.2 Experimental section

Preparation of Ni and Co-Containing Bimetallic ZIF-67: All chemicals and solvents were purchased from Sigma-Aldrich Co. LLC.and used with no further purification. In a typical synthesis, $Ni(NO_3)_2{\cdot}6H_2O$ (582 mg, 2 mmol) and $Co(NO_3)_2{\cdot}6H_2O$ (1164 mg, 4 mmol) were mixed in methanol (MeOH) (60 ml) to form a clear solution. Then

this solution was gradually poured into MeOH solution (20 ml) containing 2-methylimidazole (1968 mg, 24mmol). After thorough mixing, the solution was incubated at room temperature (25 ^{o}C) for 24 h. The as-obtained precipitate was centrifuged and washed by ethanol several times, resulting in the so-called ZIF-NCO precursor.

Synthesis of ZIF-NCO Hollow Polyhedrons: The powdered of ZIF-NCO precursor was put in a tube furnace and subsequently heated to 400 ^{o}C for 30 minutes with a heating rate of 5 ^{o}C min^{-1} under nitrogen. Then, the nitrogen gas was turned off, and the furnace was maintained at the same temperature in air for another 30 minutes. Finally, the product was taken out, showing a colour change from purple to black.

The Sulphide Conversion Process of ZIF-NCO: The sulphide conversion process was carried out by placing the ZIF-NCO nanoparticle in a sodium sulphide aqueous solution (0.1 M) at 90 ^{o}C for 24 h. The as-prepared ZIF-NCS nanoparticles were washed with DI water after the sulphide conversion process and were dried at 60 ^{o}C before utilizing as a working electrode for the supercapacitor.

Characterization of Materials: X-ray diffraction (XRD) patterns were acquired on a D8-Advanced diffractometer system from Bruker with Cu Kα radiation (λ = 1.5418 Å). Thermogravimetric-differential thermal analysis (TGA) was recorded on a PerkinElmer Diamond thermal analyser with a temperature ramp of 10 ^{o}C min^{-1} under air. The specific surface area and pore size distribution of the MOF materials were evaluated by the Brunauer−Emmett−Teller (BET) equation and the Barrett-Joyner-Halenda (BJH) method, respectively. X-ray photoelectron spectroscopy (XPS) was conducted on a ThermoEscalab 250 using an Al Kα X-ray source to detect the elemental composition of the carbon materials. The morphological information was analysed on a Zeiss Neon 40EsV FIBSEM by scanning electron microscopy (SEM) images. An FEI Titan G^{2} 80-200 TEM/STEM with ChemiSTEM Technology operating at 200 kV was used to evaluate high angle annular dark field scanning transmission electron microscopy (HAADF-STEM) imaging and element mapping. Energy dispersive X-ray spectroscopy was employed to obtain the elemental mapping with the utilization of a Super-X detector on the Titan under a probe size of ~1 nm along with a probe current of ~0.4 nA.

Electrochemical Measurements: A three-electrode system was employed to investigate the electrochemical performance of the as-prepared carbon material with a Hg/HgO electrode, a 1 M KOH solution as the reference electrode, a Pt plate as the counter electrode, and a 6 M KOH solution as the aqueous electrolyte. The working electrode was synthesized in the following procedure: the as-prepared sample, Super P as well as polytetrafluoroethylene (PTFE) were mixed at a weight ratio of 80:10:10 and fabricated into film and subsequently pressed between two nickel foams to shape the working electrode. The active material had a typical mass loading of around 3 mg cm^{-2}. A CHI 760a electrochemical workstation was used to record the cyclic voltammograms (CVs). A NEWARE BTS computer-controlled galvanostat made in Shenzhen China was adopted to obtain the galvanostatic charge and discharge measurements. Electrochemical impedance spectroscopy (EIS) was calculated at the open circuit voltage with an amplitude of 5 mV in the frequency range of 0.01 Hz to 100 kHz by a Solartron 1260 frequency response analyser together with a Solartron 1287 potentiostat.

5.3 Results and Discussion

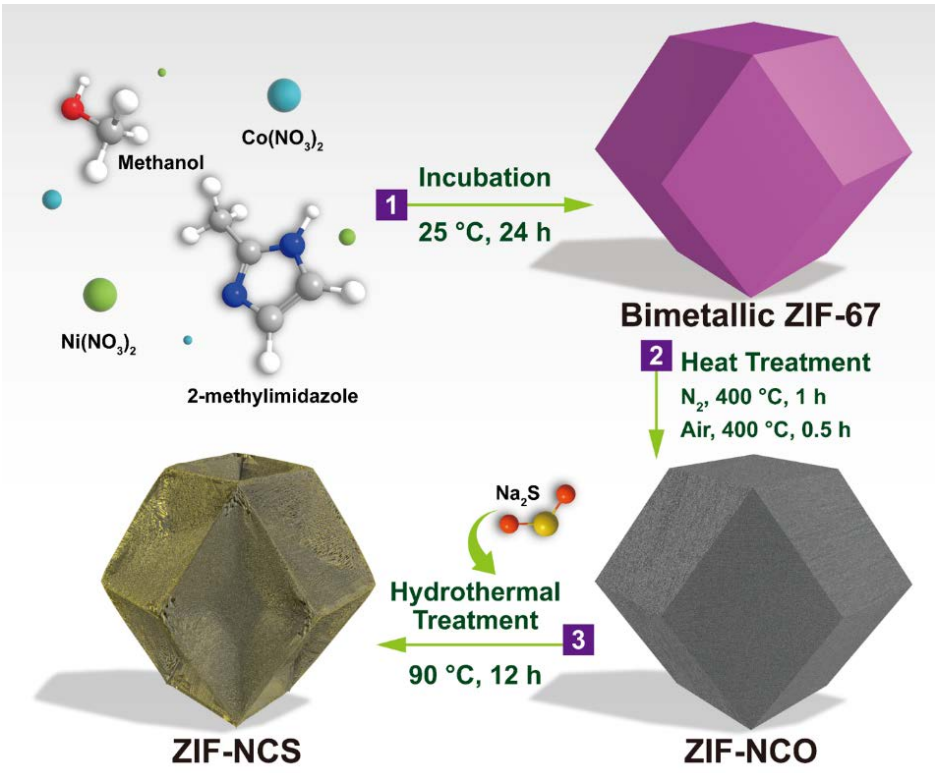

Scheme 5.1 Schematic diagram of the overall synthetic process for the ZIF-NCO and ZIF-NCS nanoparticles.

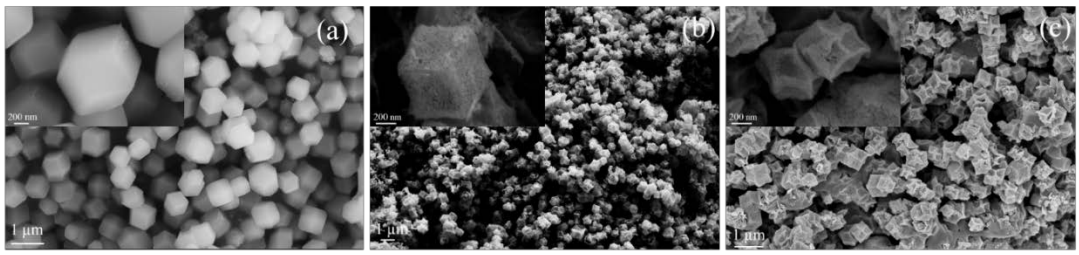

Figure 5.1 The morphologies of a) ZIF precursor, b) ZIF-NCO and c) ZIF-NCS.

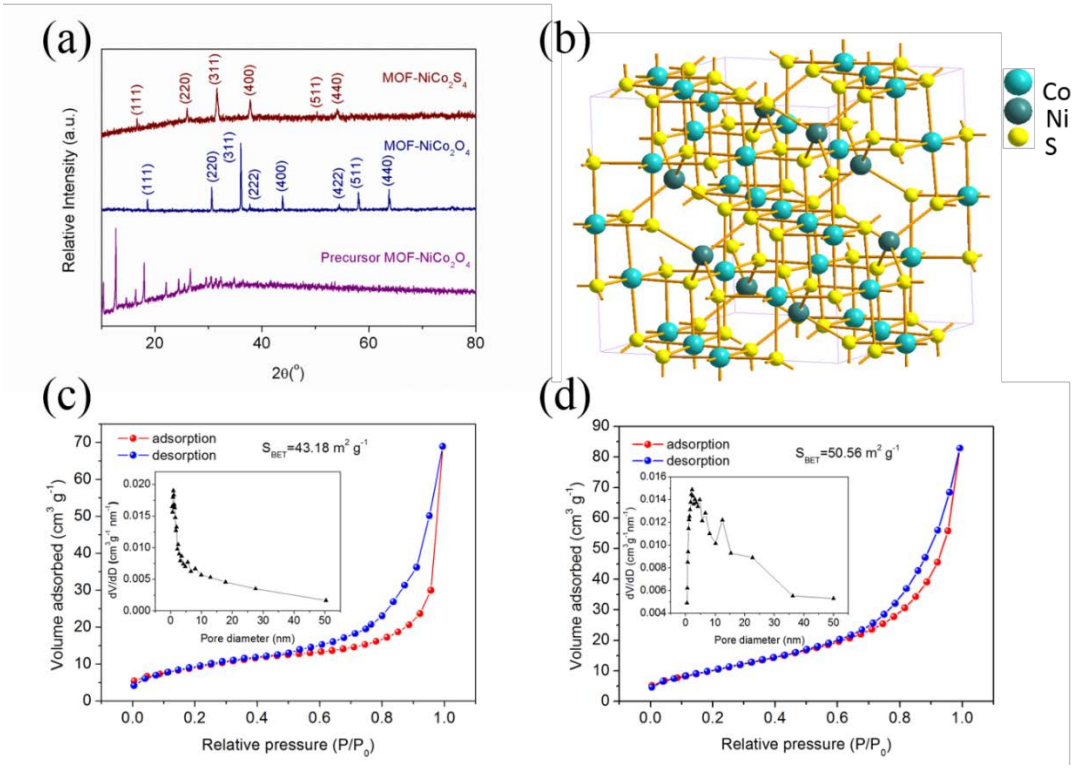

Figure 5.2 a) XRD patterns of the precursor sample, ZIF-NCO and ZIF-NCS. b) The crystal structure model of $NiCo_2S_4$. N_2 adsorption-desorption analysis of c) ZIF-NCO and d) ZIF-NCS. Insets show the corresponding pore size distribution profiles.

The schematics in **Scheme 5.1** shows the overall procedure for the synthesis of ZIF-NCO and ZIF-NCS nanostructures via the MOFs route. The successful formation of Ni and Co bimetallic ZIFs via the reaction of 2-methylimidazole with divalent Ni ions and Co ions in a methanol solution at room temperature was confirmed by both SEM and XRD characterizations. **Figure 5.1a** shows a typical SEM image of the precipitate from the synthesis. Similarly to the reported Ni or Co single metallic ZIFs,[29, 30] polyhedral nanoparticles with a uniform size of approximately 400 nm were observed from the precipitates, and such polyhedral crystals with 6 exposed [110] facets demonstrated high symmetry with smooth surfaces. The XRD pattern of the precipitate,

as shown in **Figure 5.2**, confirms the successful formation of bimetallic ZIFs, as indicated by the well match of all diffraction peaks with the typical metal organic framework (ZIF-67) material in the 2θ range between 10 and 90 °. The precipitated sample was then used as a precursor for the synthesis of ZIF-NCS. After consecutive annealing treatments at 400 °C in N_2 atmosphere for 30 min and then in air for an additional 30 min, as shown in **Figure 5.1b**, the hexahedral morphological shape was well maintained and the size of the nanoparticles did not obviously change. However, the surface of the sample after calcination became much rougher in nature. After careful observation, the polyhedrons were found to be actually composed of many nanoparticles and mesopores. In addition, the edges of the polyhedrons turned out to be denser than the other parts. It should be mentioned that pre-calcination in nitrogen is critical to maintain the polyhedral morphological structure of the precipitate in the calcined sample. Instead, the direct calcination of the precipitate in air was found to cause serious damage to the polyhedral morphology structure, likely due to over vagarious combustion of the organic ligand during the calcination. After calcination at 400 °C in first N_2 and then air, as shown in **Figure 5.2**, the diffraction pattern of the sample obviously changed, and new diffraction peaks with strong intensity were clearly indexed to the spinel-type $NiCo_2O_4$ phase (JCPDS No.20-0781). This suggests that, after the calcination, the as-prepared NiCo-bimetallic ZIF was successfully converted to the spinel-type $NiCo_2O_4$ composite oxide (ZIF-NCO). After further treatment of the calcined sample in a 0.1 M sodium sulphide aqueous solution at 90 °C for 24 h, the corresponding XRD patterns of the obtained sample were well indexed to the (111), (220), (311), (400), (511) and (440) diffraction planes of standard cubic $NiCo_2S_4$ phase (JCPDS No.43-1477). This suggests that the oxygen atoms in the spinel $NiCo_2O_4$ were successfully exchanged with sulphur atoms upon formation of spinel-type $NiCo_2S_4$ (ZIF-NCS) after the sulphidation process. Interestingly, the as-obtained ZIF-NCS sample maintained the primary polyhedral particulate morphological shape (**Figure 5.1c**). However, the polyhedrons were somewhat deformed, each facet was slightly contorted inwards, and the edges of the particles became obviously denser than the center of the facets.

As mentioned, MOFs have characteristics of high specific surface area, large pore size, and well-defined pore size distribution. The specific surface area of the as-prepared NiCo-bimetallic ZIF turned out to be higher than 1000 $m^2\ g^{-1}$. Nitrogen adsorption

technique was also used to investigate the specific surface area and pore size and its distribution of the derived ZIF-NCO and ZIF-NCS samples. According to **Figure 5.2**, N_2 adsorption and desorption isotherms of the ZIF-NCO and ZIF-NCS samples demonstrated typical type-IV profiles, suggesting the presence of rich mesopores. By applying the Brunauer-Emmett-Teller (BET) calculation method, the BET specific surface area of the produced porous ZIF-NCO polyhedrons was 43.2 m^2 g^{-1}, and increased to 50.6 m^2 g^{-1} after further sulphidation upon formation of ZIF-NCS. From the pore size distribution profiles in the insets of **Figure 5.2c&d**, the ZIF-NCO sample had pores with sizes mainly less than 3 nm. However, the pore distribution of the sample became much broader after sulphidation, and the maximum size of the pores increased up to 15 nm. The increased pore size and broadened size distribution may result from the increased specific surface area of the oxide material after the sulphidation. As we know S^{2-} (1.84 Å) has a larger anion size than O^{2-} (1.4 Å), the substitution of O^{2-} in $NiCo_2O_4$ with S^{2-} could introduce large strain inside the crystals to introduce many defects. Thus, an increase in pore size and specific surface area was observed, however, this increase allows for electrolyte to more easily access the void space of the polyhedrons, leading to higher saturation of electrolyte in the interior surface (higher utilization of the interior surface). This is beneficial for improving the electrochemical activity for energy storage.

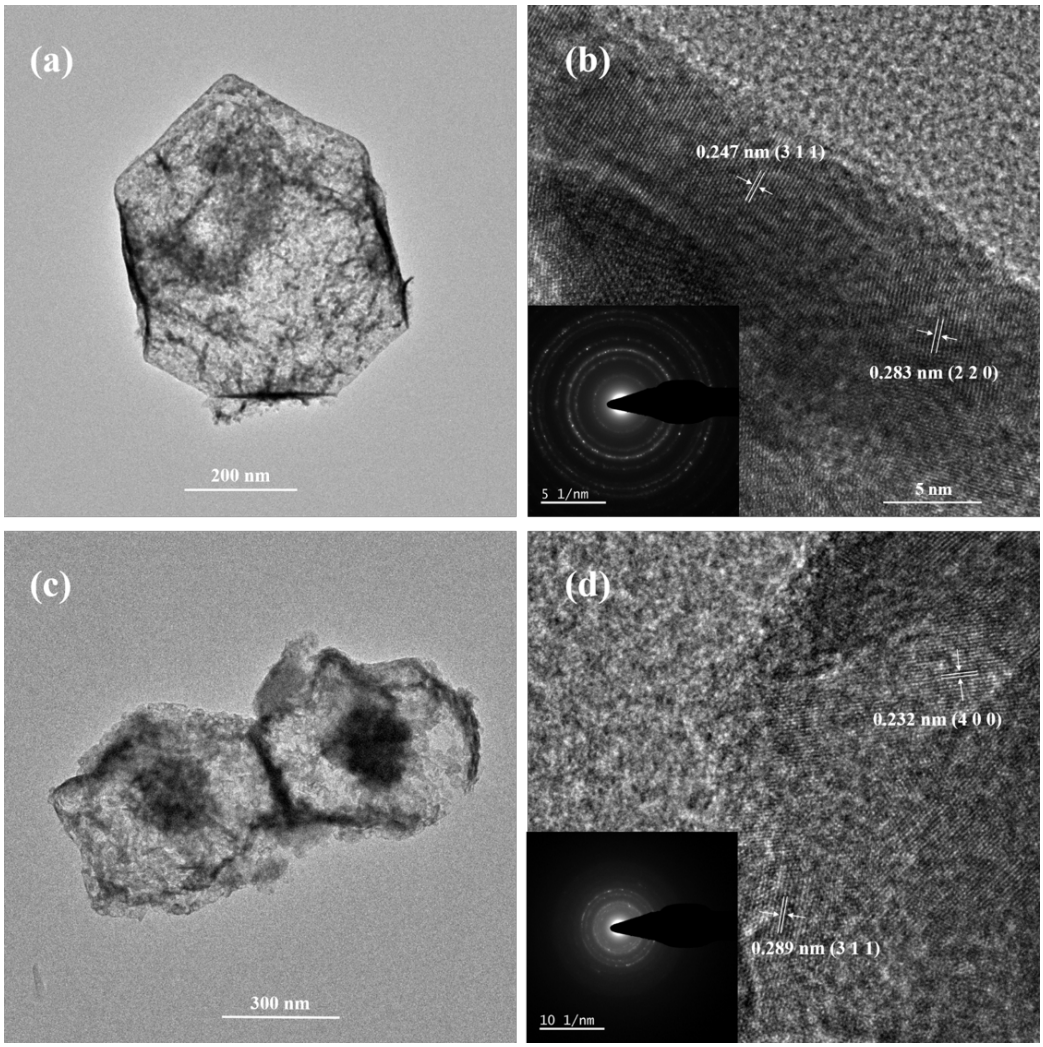

Figure 5.3. The HR-TEM images and SAED patterns of a,b) ZIF-NCO and c,d) ZIF-NCS.

To obtain further information about the microstructure of the as-synthesized ZIF-NCO and ZIF-NCS polyhedrons, TEM and HR-TEM characterizations were conducted with typical images shown in **Figure 5.3**. For the ZIF-NCO sample, the TEM image clearly demonstrates its polyhedral morphological structure with a size of 500-600 nm (**Figure 5.3a**), in well agreement with the SEM observation. The darker contrast at the edges support the earlier observation by SEM that the edges of the polyhedrons are denser. The HR-TEM in **Figure 5.3b** demonstrates that the ZIF-NCO polyhedrons were composed of nanoparticles with a size of approximately 2 nm and mesopores with diameters of 1-2 nm, which were evenly distributed in a highly homogeneous way. For the nanoparticles, lattice fringes with d-spacings of 0.247 and 0.283 nm were demonstrated from the HR-TEM image, which match well to the fringe distance of the (311) and (220) planes of the cubic spinel $NiCo_2O_4$ phase. Thus, this further confirms

the successful formation of the spinel $NiCo_2O_4$ phase in the calcined sample. The selected area electron diffraction (SAED) pattern (**Figure 5.3b, inset**) shows clear diffraction rings, demonstrating their polycrystalline characteristics. After further sulphidation, the original polyhedral particulate morphology was largely reserved, however, it was somewhat deformed, in agreement with the SEM observation. In addition, the sample demonstrated much darker contrast at the edges as well as at the center from the TEM image (**Figure 5.3c**). In combination with the SEM image (**Figure 5.1**), this is due to the higher density of the edge area for the polyhedral-structured particles. According to the HR-TEM image in **Figure 5.3d**, lattice fringes with interplanar distances of 0.232 nm and 0.289 nm were measured, which match well with the distances for the (400) and (311) planes of the hexagonal phase of $NiCo_2S_4$. This further confirms the successful conversion of $NiCo_2O_4$ to $NiCo_2S_4$ after treatment of ZIF-NCO in 0.1 M Na_2S solution. Similarly, the well-defined diffraction rings of the SAED pattern as shown in the inset of **Figure 5.3d**, suggest the polycrystalline nature of the ZIF-NCS submicron polyhedrons.

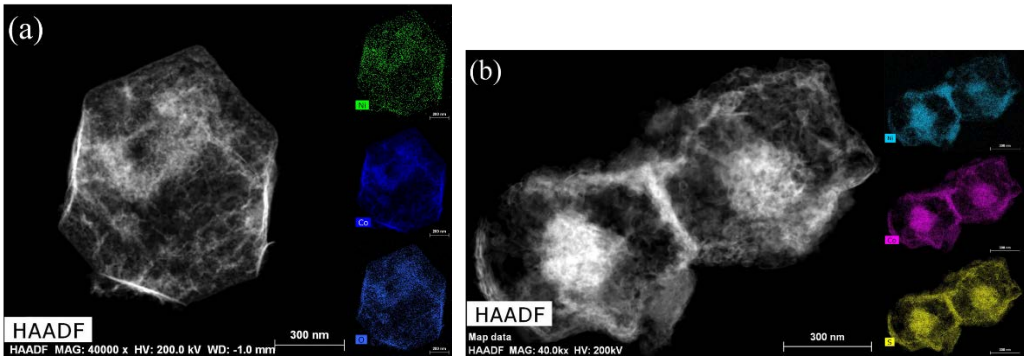

Figure 5.4. The STEM images and EDS-mapping images of a) ZIF-NCO and b) ZIF-NCS

STEM and energy-dispersive spectroscopy (EDS) mapping of ZIF-NCO and ZIF-NCS were conducted to obtain detail information about the element distributions inside the polyhedrons. As shown in **Figure 5.4**, Ni, Co and O elements were detected in the ZIF-NCO sample, and the elements showed the same distribution patterns. In addition, an EDS measurement demonstrated that the atomic ratio of the Ni:Co:O in the materials was 11.3:23.1:48.7. The above results give indirect support for the formation of $NiCo_2O_4$ in the sample. For the ZIF-NCS sample, elemental mapping demonstrated Ni, Co, and S elements distributed uniformly in the nanoparticles (**Figure 5.4b**). The EDS measurement demonstrated that the atomic ratio of Ni:Co:S in the materials was

11.7:25.9:45.1, which is very close to the stoichiometry of $NiCo_2S_4$. From the EDS results, the degree of sulpphuration is found to be more than 96 wt%.

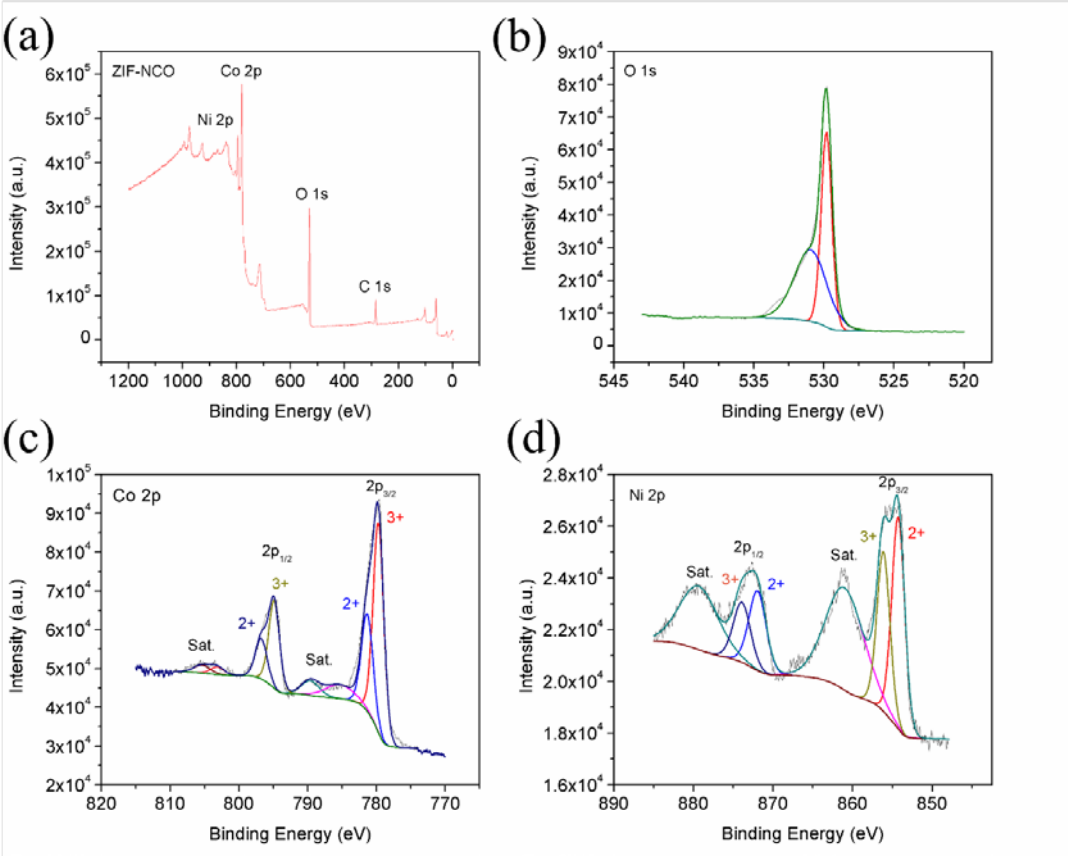

Figure 5.5 a) Survey spectra of ZIF-NCO. b) O 1s high-resolution XPS spectra of ZIF-NCO. c) Co 2p high-resolution XPS spectra of ZIF-NCO. d) Ni 2p high-resolution XPS spectra of ZIF-NCO.

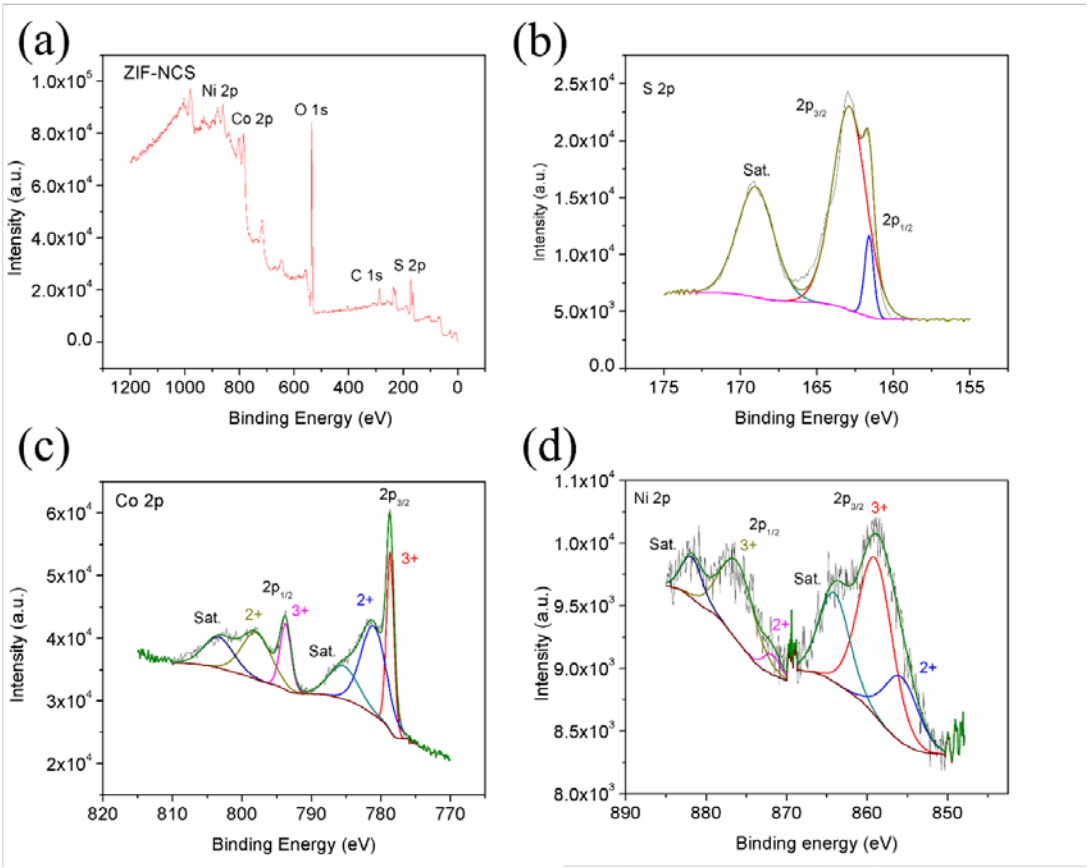

Figure 5.6 a) Survey spectra of ZIF-NCS. b) O 1s high-resolution XPS spectra of ZIF-NCS. c) Co 2p high-resolution XPS spectra of ZIF-NCS. d) Ni 2p high-resolution XPS spectra of ZIF-NCS.

X-ray photoelectron spectroscopy (XPS) was employed to further study the composition and chemical bonding states of every element in the ZIF-NCO and ZIF-NCS samples. The XPS curves of the ZIF-NCO sample are shown in **Figure 5.5**. From the survey spectrum, elements of Co, Ni and O were detected. The O 1s emission spectrum of ZIF-NCO was fitted to two main peaks. The peak at 529.9 eV is typically associated with metal-oxygen bonds, while the component at 531.1 eV came from surface oxygen ions in low coordination.[31] The Co 2p spectrum was properly divided into two spin-orbit doublets characteristics of Co^{2+} and Co^{3+} along with two shake-up satellites (identified as "Sat."). The Ni 2p spectrum was regularly divided into two spin-orbit doublets according to the characteristics of Ni^{2+} and Ni^{3+}, and two shake-up satellites peaks were fitted. The above results indicate that the chemical composition of the ZIF-NCO nanoparticles contain Co^{2+}, Co^{3+}, Ni^{2+}, and Ni^{3+}, corresponding to the results in a previous report for $NiCo_2O_4$.[32] These results show the surface properties of the polyhedral ZIF-NCO particles. After the substitution of O^{2-} in ZIF-NCO with

S^{2-}, the peaks of S, Co, and Ni elements can be clearly observed from the survey XPS curve, as shown in **Figure 5.6a**, which indicate that the ZIF-NCS sample basically consists of Ni, Co, and S elements with no other obvious impurities. Ni, Co, and S exhibited an atomic ratio of 1:2.06:4.16, which is very close to the theoretical value of the ideal $NiCo_2S_4$ phase. **Figure 5.6b–d** show the XPS core-level spectra of S, Co, and Ni with peaks fitted by Gaussian methods. The core-level spectrum of the S 2p region is displayed in **Figure 5.6b**, where binding energies at 163.7 and 162.6 eV represent S 2p1/2 and S 2p3/2, respectively. In detail, the peak at 163.7 eV is arises from metal-sulphur bonds,[33] while the peak at 162.6 eV is likely ascribed to S^{2-} in low coordination at the surface. A similar method can also be applied for fitting the Co 2p spectrum. Strong peaks at 778.7 eV for Co 2p3/2 and 797.7 eV for Co 2p1/2 are demonstrated in **Figure 5.6c**, showing the co-existence of Co^{3+} and Co^{2+}. The Ni 2p3/2 and Ni 2p1/2 emission spectra (**Figure 5.6d**) were properly divided into spin–orbit doublets and shake-up satellites (marked as "Sat."), corresponding to the characteristics of Ni^{2+} and Ni^{3+}. Through comparison of the intense fitted peaks in the spectrum, the majority of Ni element in the crystal lattice is Ni^{3+} cations.[33] All results show that the chemical composition of the as-prepared ZIF-NCS sample contains Co^{2+}, Co^{3+}, Ni^{2+}, and Ni^{3+}, agreeing with the results in the literature for $NiCo_2S_4$.[33]

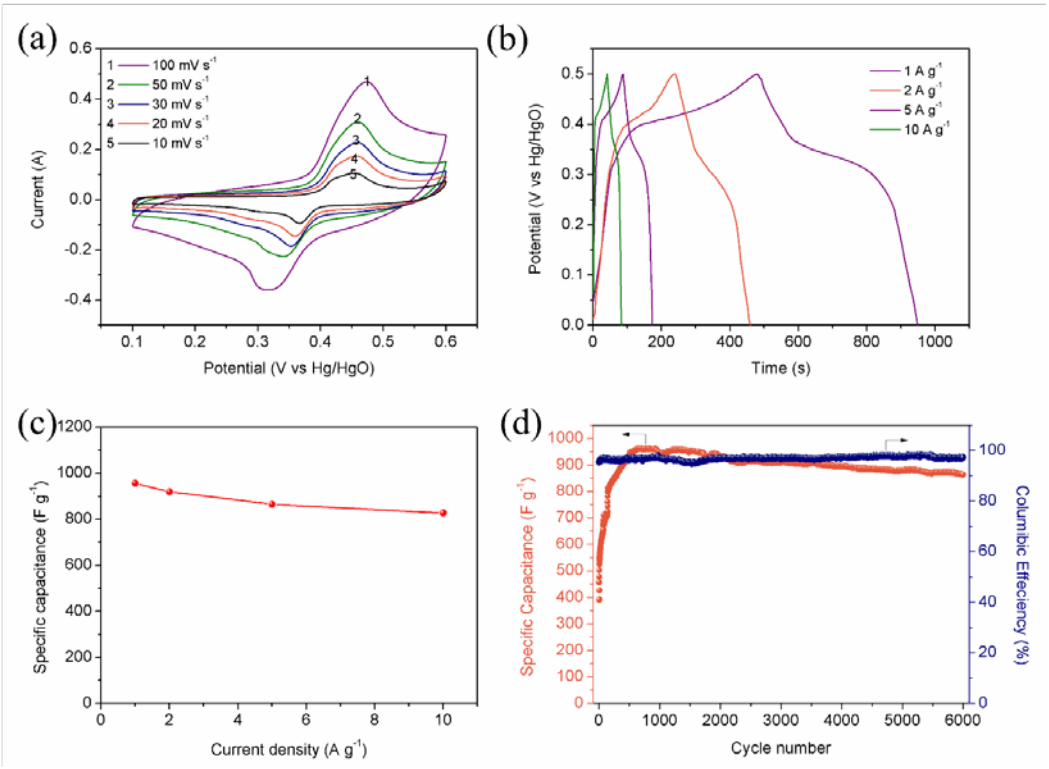

Figure 5.7. a) CV curves of ZIF-NCO at different scan rates b) Galvanostatic charge-discharge curves at different current densities for three electrodes c) Specific capacitance of ZIF-NCO at different current densities. d) Long-term cycling stability of ZIF-NCO electrode at a galvanostatic charge-discharge current density of 1 A g^{-1}.

The pseudocapacitive performance of as-prepared mesoporous ZIF-NCO and ZIF-NCS nanostructures was first studied by cyclic voltammetry (CV) in three electrode devices using the materials as working electrodes. In a 6M alkaline electrolyte solution (KOH), the typical CV curves of the ZIF-NCO electrode at different sweep rates in the range of 10 to 100 mV s^{-1} in the voltage range of 0-0.6 V are displayed in **Figure 5.7**. Similar shapes were displayed in the CV curves with a pair of distinct redox peaks within 0.0-0.6 V (vs. Hg/HgO), which is in good agreement with previous reports on a $NiCo_2O_4$ electrode in alkaline electrolyte solution,[34] confirming the pseudocapacitance behaviour of the electrode during the charge storage process. It is reasonable to assume that the capacitance is contributed primarily from the redox pseudocapacitance of the loaded $NiCo_2O_4$, since the treated Ni foam in the working electrode had a very small surface area, and therefore, its contribution to the total capacitance was negligible. More specifically, the redox peaks in the CV curves can be assigned to couples with electrochemical reactions between the Ni−O and Ni−O−O−OH and between Co−O and Co−O−O−OH over the electrode surface.[32] With an increase in scan rate from 10 to 100 mV s^{-1}, the position of the anodic peak shifts from 0.43 to 0.48 V, suggesting that a charge-transfer process is rate limiting during the electrode reactions.[35] The CV curves of the ZIF-NCO presented here demonstrate a much more uniform distribution of the enclosed redox area along the whole potential window, unlike Co_3O_4 electrodes that show a concentration on the more positive potential region.[36] Such a property may be a benefit of binary metal oxides that serve as supercapacitor electrode materials because both constituent metal ions contribute to the potential increase in feasible oxidation states/structures.

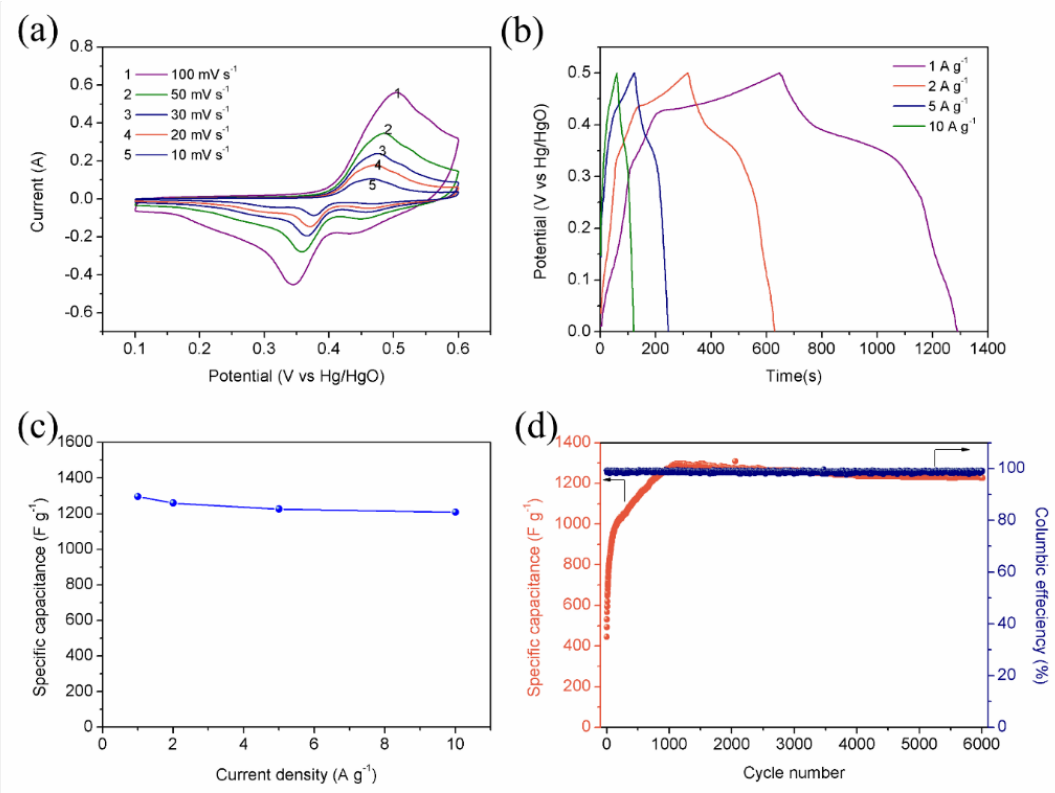

Figure 5.8 a) CV curves of ZIF-NCS at different scan rates. b) Galvanostatic charge-discharge curves at different current densities for the three electrodes. c) Specific capacitance of ZIF-NCS at different current densities. d) Long-term cycling stability of the ZIF-NCS electrode at a galvanostatic charge-discharge current density of 1 A g^{-1}.

For the mesoporous ZIF-NCS polyhedrons, as shown in **Figure 5.8a**, the CV curves show parallel shapes with the appearance of redox peaks, indicating the pseudocapacitive characteristic of the work electrode as well. The redox peaks are assigned to Ni^{2+}/Ni^{3+} and $Co^{2+}/Co^{3+}/Co^{4+}$ redox couples involving M–S/M–S–OH and M–S–OH/M–S–O. This is because the $NiCo_2S_4$ material is suitable as a supercapacitor electrode with a high pseudocapacitive performance. Due to the similar redox potentials of the two reactions, the peaks were seriously overlapped. Thus, only a pair of redox peaks appeared. This comparatively reflects the larger current responses as well as the larger integral areas of the CV curves. The comparative CV curves at all scan rates clearly show a larger pseudocapacitance for ZIF-NCS than for ZIF-NCO. The possible electrochemical redox reactions for $NiCo_2S_4$ are represented as follows:

$$NiCo_2S_4 + OH^- \leftrightarrow NiS_{4-2x}OH + 2CoS_xOH + 2e^- \quad (5.1)$$

$$CoS_xOH + OH^- \leftrightarrow CoS_xO + H_2O + e^- \quad (5.2)$$

No obvious change was observed in the shapes of CV curves while the oxidation and reduction peaks shifted towards higher and lower potentials, respectively, upon increasing the scan rates, which indicates good electrochemical reversibility and enlarged potential separation. The position of the anodic peak shifted from 0.47 to 0.51 V when the scan rate increased from 10 to 100 mV s^{-1}. For ZIF-NCS, the increment was only 0.04 V, and the increment was 0.05 V for ZIF-NCO electrode under the same conditions. This suggests that ZIF-NCS had better electrode reaction kinetics than the ZIF-NCO electrode. Such improvement in the performance may be related to higher electronic conductivity (thus, improved charge transfer), higher surface area (thus, increased active sites), and lower metal-anion bond energy (thus, enhanced redox process for the surface Co and Ni) after the substitution of O^{2-} in $NiCo_2O_4$ with S^{2-} forming $NiCo_2S_4$.

The electrochemical performance of the ZIF-NCO and ZIF-NCS electrodes were further evaluated by galvanostatic charge/discharge tests at different current densities in the range of 1 to 10 A g^{-1}. In **Figure 5.7** and **Figure 5.8**, the pseudocapacitive behaviours of the ZIF-NCO and ZIF-NCS electrodes were further established by the nonlinear charge/discharge curves. The specific capacitance was calculated in accordance with the formula shown in Equation (5.3), in which i represents the discharge current (Ag^{-1}), Δt represents the discharge time (s), ΔV represents the potential window (V), and m is the mass of the active material (mg).

$$C = i\Delta t/\Delta V m \quad (5.3)$$

The corresponding specific capacitances of ZIF-NCO were calculated to be 956, 920,865 and 828 F g^{-1} at current densities of 1, 2, 5 and 10 A g^{-1}, respectively, revealing the good rate capability of the ZIF-NCO electrode. On the other hand, the calculated specific capacitances of the ZIF-NCS electrode reached 1296, 1260, 1226 and 1208 F g^{-1} respectively at the current densities 1, 2, 5 and 10 A g^{-1}, which are among the highest values reported for self-supported bulk-phase transition metal-based electrode materials. Attractively, the capacitance retention at a current density of 10 A g^{-1} was 93.2% for ZIF-NCS. As a comparison, it was 86.6% for the ZIF-NCO electrode under the same current conditions. The reason for this is the high electrical conductivity along with the bigger specific surface area and more active sites of ZIF-NCS than ZIF-

NCO. The cycling performances of both electrodes were investigated at a current density of 1 A g^{-1}. As displayed in **Figure 5.8d,** the ZIF-NCS electrode exhibited superior cycling stability with capacitance retention of 94.5 % after the galvanic charge-discharge cycling at a current density of 1 A g^{-1} for 6000 cycles; as a comparison, the capacitance retention was 90.4 % for the ZIF-NCO electrode after the same operation. It should be mentioned that this is outstanding cycling stability because the specific capacitance was still 1108 F g^{-1} even after 6000 cycles, representing just a 5.5% loss from the maximum value. As a comparison, it was reported by Yan et al. that the bare $NiCo_2S_4$ electrode, prepared by a hydrothermal method, lost 18 % of its original capacitance after 2000 cycles.[37] The porous structure of the ZIF-NCO and ZIF-NCS provided buffer space to effectively accommodate the volume change during the Faradiac reaction over the electrode surface, which helped prevent the pulverization of the electrode materials, thus ensuring the high cycling stability. The higher pore volumes and larger pore size of the ZIF-NCS than ZIF-NCO provided a more efficient way to prevent the pulverization of the electrode, thus demonstrating better cycling performance.[37]

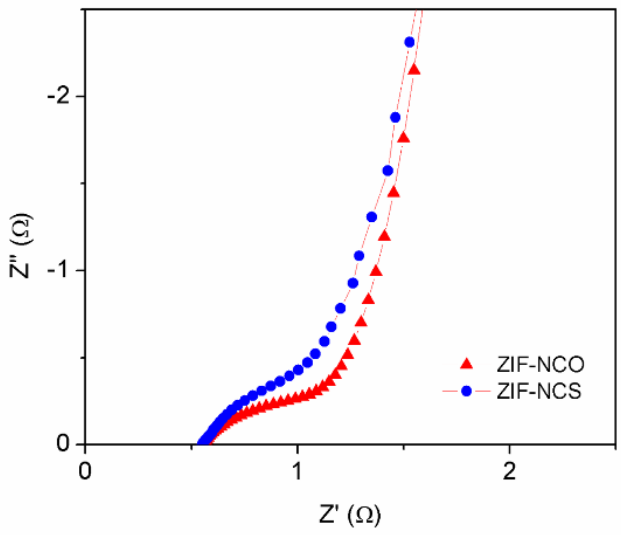

Figure 5.9 Impedances of ZIF-NCO and ZIF-NCS as electrodes of the supercapacitor.

Electrochemical impedance spectroscopy (EIS) was performed to give evidence for the superior electrochemical performance of both ZIF-NCO and ZIF-NCS electrodes. The typical Nyquist plots are represented in **Figure 5.9**. The EIS showed a suppressed semicircle when the frequency ranged from high to intermediate and a long straight

tail at the low frequency range. Typically, the intercept of the impedance arc with the real axis at the high frequency range refers to the resistance of charge transfer (Rct), while the impedance arc at the intermediate frequency range is linked to the charge-transfer process. The sloped line in the low frequency region is usually in association with the diffusion of OH^-.[38] For both electrodes, their high frequency intercepts were almost overlapped, suggesting nearly equal bulk solution resistance (Rs). For the ZIF-NCS electrode, a slightly smaller semicircle was observed than that of the ZIF-NCO electrode, indicating that a lower interfacial charge transfer resistance (Rct) was experienced with the ZIF-NCS electrode. Nevertheless, both electrodes showed very low-charge transfer resistances with calculated values of charge transfer resistances of 0.59 and 0.48 Ω respectively for the ZIF-NCO and ZIF-NCS electrodes. In addition, both ZIF-NCS and ZIF-NCO showed a similar diffusion resistance for OH^- ions according to their similar shape for the straight tails at the low frequency range.

The overall results of the above electrochemical performances suggest that both ZIF-NCO and ZIF-NCS electrodes show highly attractive electrochemical performances for energy storage through pseudocapacitance, and ZIF-NCS is even more superior. The better supercapacitive performance of the ZIF-NCS nanoparticles resulted from the following structural and composite features.[39] Normally, the replacement of O ions with S ions in the oxide can improve the conductivity, which can speed up the electron-transport rates at the material surface during the electron-storage processes. Moreover, the ZIF-NCS material that features a high surface area could increase the number of electroactive sites and facilitate the rapid diffusion of ions because it can provide ions with low-resistance pathways for the ions through the electrode material.

Table 5.1. Nickle and cobalt related oxide electrodes in asymmetric supercapacitors reported in previous literatures.[44-51]

Asymmetric supercapacitors	Energy density [Wh kg^{-1}]	Power density [W kg^{-1}]
ZIF-NCS//AC (This work)	44.8	794.5
$NiCo_2O_4$//AC[44]	17.72	25420
submicron/micron-sized $NiCo_2O_4$//AC[45]	14.7	175
Porous Ni–Co oxide//AC[46]	12	95.2
Ni_xCo_{1-x} LDH–ZTO heterostructure//AC[47]	23.7	284.2
$NiCo_2O_4$–RGO//AC[48]	23.3	324.9

Amorphous $NiWO_4$//AC[49]	25.3	200
Nano β-$NiMoO_4$–$CoMoO_4 \cdot xH_2O$//AC[50]	28/18	100/1000
CoMoO4–$NiMoO_4 \cdot xH_2O$ bundles//AC[51]	24.95/15.54	164.5/1645.4

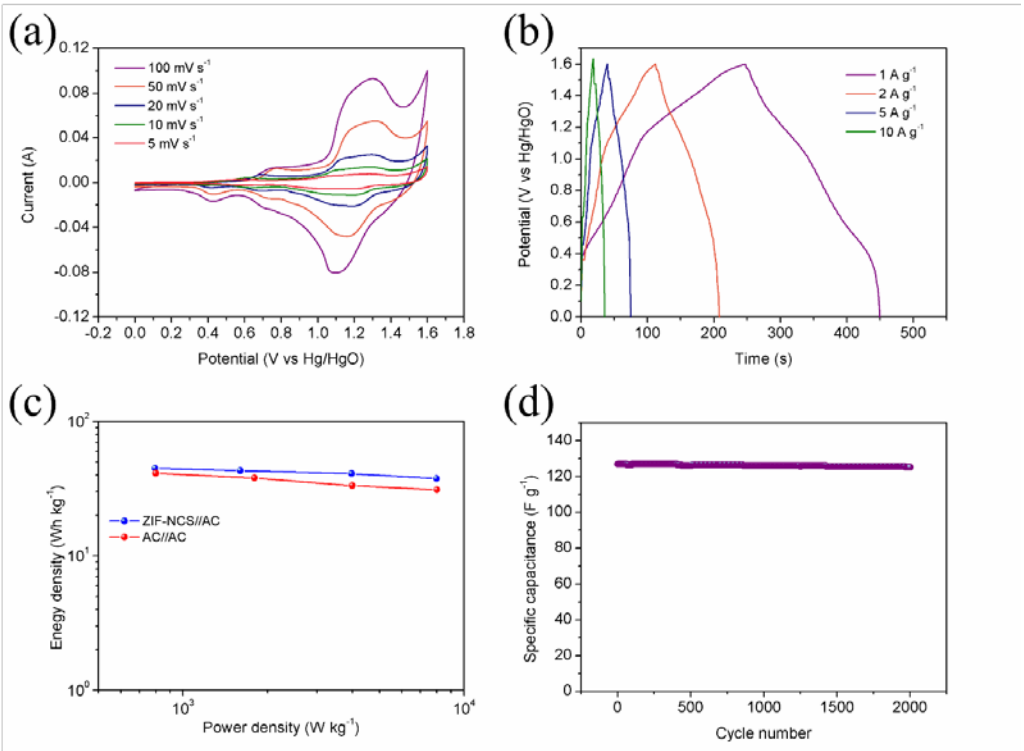

Figure 5.10. a) CV curves at different scan rates and b) galvanostatic charge/discharge curves at different current densities of the ZIF-NCS//AC asymmetrical supercapacitor. c) Ragone plots of the ZIF-NCS//AC and AC//AC device. d) Cycling performance of ZIF-NCS//AC device at a current density of 1 A g^{-1}.

To further evaluate the performance of the ZIF-derived NCS in complete supercapacitors, an asymmetric cell (ASC) using the ZIF-NCS submicron polyhedron as the positive electrode and active carbon (AC) as the negative electrode was built and tested by CV at different scan rates within the potential window of 0.0-1.6 V. According to the shape of the CV curves shown in **Figure 5.10**, both electrical double-layer capacitance and pseudocapacitance appear in the charge-storage process. The shape of the CV curves did not obviously changed with an increase in scan rate from 10 to 100 mV s^{-1}, implying good reversibility and kinetics for the electrode reactions over the ASC electrodes. The specific capacitance, on the basis of the total mass of

both electrodes, was calculated by the as-measured galvanostatic charge/discharge curves (**Figure 5.10**). Remarkably, the asymmetric supercapacitor device achieved a capability of 126.6 F g^{-1} at a current density of 1 A g^{-1}. A specific capacitance of 106.3 F g^{-1} was still maintained even at a much higher discharge current density of 10 A g^{-1}, suggesting a capacitance retention of 83.9 % by increasing in ten times of the discharge current density from 1 A g^{-1}. From the Ragone plot derived from the galvanostatic charge/discharge curves (**Figure 5.10**), the asymmetric supercapacitor demonstrated a high energy density of 44.8 Wh kg^{-1} at a power density of 794.5 W kg^{-1}. A favourable energy density of 37.7 Wh kg^{-1} was still reached even at a higher power density of 7981.1 W kg^{-1}, demonstrating the excellent rate performance of the ASC with the ZIF-NCS positive electrode. The energy density of current asymmetrical supercapacitor is much higher than that of the reported nickel cobaltite-graphene//AC asymmetrical supercapacitor (19.5 Wh kg^{-1} at about 100 W kg^{-1}) at a comparable mass loading,[40] and also much higher than many carbon-based symmetric supercapacitors with similar aqueous electrolyte.[41-43] The high energy density can be attributed to the high specific capacitance of the ZIF-NCS electrode and the large cell voltage. In addition, the current asymmetric supercapacitor with the ZIF-NCS electrode also delivered higher energy densities than many asymmetric supercapacitors with various nickel and cobalt related oxide electrodes as reported in literature, exhibiting in the **Table 5.1**.[44-51] All these attractive results further confirm the outstanding supercapacitive performance of the ZIF-NCS electrode.

5.4. Conclusions

In conclusion, porous spinel-type $NiCo_2O_4$ (ZIF-NCO) and $NiCo_2S_4$ (ZIF-NCS) were successfully prepared using NiCo-bimetallic ZIFs as solid precursors. Both samples demonstrated a three-dimensional open structure, high surface area and good crystallinity. Outstanding supercapacitive performance, rate capability, and cycling stability were achieved based on CV as well as galvanostatic charge/discharge tests, which is attributed to their special open structure (allowing easy access to the liquid electrolyte for surface Faradaic reactions, fast ionic and electronic transportation and good mechanical integrity) and high surface area (large active sites). In particular, the specific capacitance of the ZIF-NCS nanoparticles reached 1296, 1260, 1226 and 1208 F g^{-1} at current densities of 1, 2, 5 and 10 A g^{-1}, respectively, which are among the best results for self-supported NiCo-based electrodes available in literature. The ZIF-NCS

electrode also showed very good cycling stability, with a capacitance retention of 94.5 % after galvanostatic charge-discharge cycling at 1 A g^{-1} for 6000 cyclyes, which is linked to the porous structure of the nanoparticles that effectively provided buffer space for the volume change of the electrode material during cycling to suppress the pulverization of the electrode material. An asymmetrical cell consisting of the as-prepared ZIF-NCS positive electrode and an amorphous carbon negative electrode was successfully built and delivered a noticeably high energy density (44.8 Wh kg^{-1}) as well as power density (794.5 W kg^{-1}) that were higher than those of most asymmetrical supercapacitors reported in the literature. This simple method using ZIFs as a precursor for the fabrication of porous composite oxides or composite sulphides could be easily extended to the preparation of other porous metal oxides or sulphides in the application of supercapacitors. More broadly, with the adoption of suitable precursor MOFs, the obtained metal oxides and sulphides may pave new pathways for application in other possible areas, such as lithium-ion batteries, magnets, and sensors.

5.5 Reference

[1] W. Wei, X. Cui, W. Chen, D. G. Ivey, Chem. Soc. Rev. 2011, 40, 1697.

[2] L. L. Zhang, X. S. Zhao, Chem. Soc. Rev. 2009, 38, 2520.

[3] Y. Liu, J. Dinh, M. O. Tade, Z. Shao, ACS Appl. Mater. Interfaces 2016, 8, 23774.

[4] G. Wang, L. Zhang, J. Zhang, Chem. Soc. Rev. 2012, 41, 797.

[5] C. Zhong, Y. Deng, W. Hu, J. Qiao, L. Zhang, J. Zhang, Chem. Soc. Rev. 2015, 44, 7484.

[6] O. M. Yaghi, G. Li, H. Li, Nature 1995, 378, 703.

[7] O. K. Farha, A. Özgür Yazaydın, I. Eryazici, C. D. Malliakas, B. G. Hauser, M. G. Kanatzidis, S. T. Nguyen, R. Q. Snurr, J. T. Hupp, Nat. Chem. 2010, 2, 944.

[8] W. Wang, X. Xu, W. Zhou, Z. Shao, Adv. Sci. 2017, 1600371.

[9] N. L. Rosi, J. Eckert, M. Eddaoudi, D. T. Vodak, J. Kim, M. Keeffe, O. M. Yaghi, Science 2003, 300, 1127.

[10] J. R. Li, R. J. Kuppler, H. C. Zhou, Chem. Soc. Rev. 2009, 38, 1477.

[11] D. Sheberla, J. C. Bachman, J. S. Elias, C. J. Sun, Y. Shao Horn, M. Dinca, Nat Mater 2017, 16, 220.

[12] R. Wu, X. Qian, K. Zhou, J. Wei, J. Lou, P. M. Ajayan, ACS Nano 2014, 8, 6297.

[13] D. Y. Lee, S. J. Yoon, N. K. Shrestha, S. H. Lee, H. Ahn, S. H. Han, Microporous Mesoporous Mater. 2012, 153, 163.

[14] J. Yang, P. Xiong, C. Zheng, H. Qiu, M. Wei, J. Mater. Chem. A 2014, 2, 16640.

[15] X. Cao, B. Zheng, W. Shi, J. Yang, Z. Fan, Z. Luo, X. Rui, B. Chen, Q. Yan, H. Zhang, Adv. Mater. 2015, 27, 4695.

[16] R. R. Salunkhe, J. Tang, Y. Kamachi, T. Nakato, J. H. Kim, Y. Yamauchi, ACS Nano 2015, 9, 6288.

[17] P. Zhang, F. Sun, Z. Shen, D. Cao, J. Mater. Chem. A 2014, 2, 12873.

[18] J. Tang, R. R. Salunkhe, J. Liu, N. L. Torad, M. Imura, S. Furukawa, Y. Yamauchi, J. Am. Chem. Soc. 2015, 137, 1572.

[19] L. Zhang, H. B. Wu, X. W. Lou, Chem. Commun. 2012, 48, 6912.

[20] S. W. Chou, J. Y. Lin, J. Electrochem. Soc. 2013, 160, D178.

[21] L. Shen, J. Wang, G. Xu, H. Li, H. Dou, X. Zhang, Adv. Energy Mater. 2015, 5, 1400977.

[22] J. Pu, T. Wang, H. Wang, Y. Tong, C. Lu, W. Kong, Z. Wang, ChemPlusChem 2014, 79, 577.

[23] G. Zhang, X. W. Lou, Adv. Mater. 2013, 25, 976.

[24] H. Chen, J. Jiang, L. Zhang, H. Wan, T. Qi, D. Xia, Nanoscale 2013, 5, 8879.

[25] J. Xiao, L. Wan, S. Yang, F. Xiao, S. Wang, Nano Lett. 2014, 14, 831.

[26] H. Chen, J. Jiang, L. Zhang, D. Xia, Y. Zhao, D. Guo, T. Qi, H. Wan, J. Power Sources 2014, 254, 249.

[27] L. Yu, L. Zhang, H. B. Wu, X. W. Lou, Angew. Chem. Int. Ed 2014, 126, 3785.

[28] J. Pu, F. Cui, S. Chu, T. Wang, E. Sheng, Z. Wang, ACS Sustainable Chem. Eng. 2014, 2, 809.

[29] B. Y. Xia, Y. Yan, N. Li, H. B. Wu, X. W. Lou, X. Wang, Nat. Energy 2016, 1, 15006.

[30] J. Zhang, H. Hu, Z. Li, X. W. Lou, Angew. Chem. Int. Ed. 2016, 55, 3982.

[31] M. C. Biesinger, B. P. Payne, A. P. Grosvenor, L. W. M. Lau, A. R. Gerson, R. S. C. Smart, Appl. Surf. Sci. 2011, 257, 2717.

[32] Y. Lei, J. Li, Y. Wang, L. Gu, Y. Chang, H. Yuan, D. Xiao, ACS Appl. Mater. Interfaces 2014, 6, 1773.

[33] S. Y. Khoo, J. Miao, H. B. Yang, Z. He, K. C. Leong, B. Liu, T. T. Y. Tan, Adv. Mater. Interfaces 2015, 2, 1500384.

[34] Y. Zhu, X. Ji, Z. Wu, W. Song, H. Hou, Z. Wu, X. He, Q. Chen, C. E. Banks, J. Power Sources 2014, 267, 888.

[35] W. Xiong, Y. Gao, X. Wu, X. Hu, D. Lan, Y. Chen, X. Pu, Y. Zeng, J. Su, Z. Zhu, ACS Appl. Mater. Interfaces 2014, 6, 19416.

[36] T. Wei, C. Chen, H. Chien, S. Lu, C. Hu, Adv. Mater. 2010, 22, 347.

[37] S. Peng, L. Li, C. Li, H. Tan, R. Cai, H. Yu, S. Mhaisalkar, M. Srinivasan, S. Ramakrishna, Q. Yan, Chem. Commun. 2013, 49, 10178.

[38] S. Raj, S. K. Srivastava, P. Kar, P. Roy, RSC Adv. 2016, 6, 95760.

[39] H. Jiang, J. Ma, C. Li, Chem. Commun. 2012, 48, 4465.

[40] H. Wang, C. M. B. Holt, Z. Li, X. Tan, B. S. Amirkhiz, Z. Xu, B. C. Olsen, T. Stephenson, D. Mitlin, Nano Res. 2012, 5, 605.

[41] Z. Lei, Z. Liu, H. Wang, X. Sun, L. Lu, X. S. Zhao, J. Mater. Chem. A 2013, 1, 2313.

[42] L. Niu, Z. Li, W. Hong, J. Sun, Z. Wang, L. Ma, J. Wang, S. Yang, Electrochim. Acta 2013, 108, 666.

[43] Z. Algharaibeh, P. G. Pickup, Electrochem. Commun. 2011, 13, 147.

[44] C. T. Hsu, C. C. Hu, J. Power Sources 2013, 242, 662.

[45] R. Ding, L. Qi, M. Jia, H. Wang, Electrochim. Acta 2013, 107, 494.

[46] C. Tang, Z. Tang, H. Gong, J. Electrochem. Soc. 2012, 159, A651.

[47] X. Wang, A. Sumboja, M. Lin, J. Yan, P. S. Lee, Nanoscale 2012, 4, 7266.

[48] X. Wang, W. S. Liu, X. Lu, P. S. Lee, J. Mater. Chem. A 2012, 22, 23114.

[49] L. Niu, Z. Li, Y. Xu, J. Sun, W. Hong, X. Liu, J. Wang, S. Yang, ACS Appl. Mater. Interfaces 2013, 5, 8044.

[50] B. Senthilkumar, D. Meyrick, Y. S. Lee, R. K. Selvan, RSC Adv. 2013, 3, 16542.

[51] M. C. Liu, L. B. Kong, C. Lu, X. J. Ma, X. M. Li, Y. C. Luo, L. Kang, J. Mater. Chem. A 2013, 1, 1380.

Chapter 6 Hierarchically porous bio-carbon microspheres derived from natural date pulp as efficient and stable oxygen-reduction electrocatalysts

Abstract

In this chapter, hierarchically porous bio-carbon microspheres are fabricated and used as highly active and stable electrocatalysts for oxygen reduction reaction (ORR) under both alkaline and acidic conditions. Renewable natural date pulp is used as the carbon precursor, and a facile hydrothermal carbonization method with *in situ* formed cobalt as a template is employed for the synthesis of such spherical bio-carbons. Remarkably, the catalysts yield competitive catalytic activity (a small Tafel slope of 53 mV dec^{-1}) and superb durability and methanol tolerance compared to the benchmark Pt/C catalyst in an alkaline electrolyte. Even under harsh acidic conditions, the catalysts still deliver a satisfactory catalytic performance and excellent stability, indicating their extensive applicability. This attractive performance can mainly be attributed to high number of surface defects and the hierarchically porous structure that effectively boost the mass and charge transfer and provide abundant active sites for oxygen reduction. *In situ* formed cobalt nanoparticles are critical to the creation of the abundant mesopores, high specific surface area, and catalytically active defect sites over the carbon material. A small amount of encapsulated cobalt further enhances the ORR activity of the carbon material.

6.1 Introduction

The impending global energy crisis and environmental concerns associated with the excessive use of fossil fuels have prompted us to explore highly sustainable alternative energy sources as well as highly efficient eco-friendly energy conversion and storage technologies. Fuel cells are electrochemical energy conversion devices with energy conversion efficiencies two times greater than those of conventional fire powered plants.[1] The combination of fuel cells and hydrogen energy may provide a sustainable and green energy system for the future. Metal-air batteries are highly attractive electrochemical energy storage devices that may fill the gap between the renewable energy (e.g., wind and solar power) and the state-of-the-art energy infrastructure, and possibly also be considered as the main power source for electrified transportation.[2-5] Such electrochemical devices normally involve an oxygen reduction reaction (ORR) over their positive electrode; unfortunately, the sluggish ORR kinetics at room temperature significantly limit their efficiency and performance, and thus have become a major obstacle towards their practical applications.[6, 7] The noble metal platinum (Pt) has traditionally been considered the most efficient ORR electrocatalyst in fuel cells; however, it suffers from prohibitive cost, low natural abundance, and poor durability.[8-10] In recent years, intense effort has been devoted to searching for efficient alternative catalysts.[11-15] Among the various candidates, carbon materials have attracted tremendous attention due to their essential properties such as excellent electronic conductivity, good resistance to acidic and basic environments, unique surface properties, high thermal and chemical stability, easy accessibility, and low cost.[16, 17] Nevertheless, to date, the electrochemical performances of most reported carbon materials are still slightly worse than that of the most advanced Pt-based catalyst. To further boost the ORR activity of the carbon materials to satisfy the requirements for implementation in practical devices, strategies that involve surface functionalization by doping carbon materials with heteroatoms and/or the construction of hierarchically porous morphological structures have been widely explored.[18-25] Recently, it has also been demonstrated that the introduction of surface defects could significantly increase the electrochemical activity of carbon materials.[26-28]

Pyrolysis of organic precursors is widely used for the preparation of functional carbon materials for various applications.[29-33] By tailoring the composition of starting organic precursor, catalyst and pyrolysis parameters, carbon materials with different

properties can be synthesized. Traditionally, simple organic substances with well-defined compositions, such as citric acid, glucose and fructose, have been extensively used as precursors to synthesize the carbon materials.[34-36] Biomass is a highly promising class of precursor for preparing carbon materials due to its renewability and cost effectiveness.[37-40] The conversion of biomass to functional carbon materials carries with it significant environmental benefits including reducing greenhouse gas emission. In addition, most biomass materials also contain N, S and P in certain amounts. During the pyrolysis for carbon formation, the simultaneous doping of such elements into the carbon lattice structure may also occur, which further tailors the properties of the carbon materials. Date is an edible sweet fruit, which is widely cultivated and naturalized in many tropical and subtropical regions worldwide. The sugar content of ripe dates is up to 80%. Therefore, date is very suitable as the source for the low-cost development of carbon catalysts.

Herein, we report on the successful preparation of hierarchically porous bio-carbon microspheres (PBCS) from natural date pulp and their use as an exceedingly active and stable ORR electrocatalyst under both basic and acidic conditions with activities comparable to the benchmark Pt/C catalyst while having much better operational stability. The importance of cobalt during the synthesis in creating active sites for the ORR is demonstrated. As a general method, it may also be suitable for the preparation of functional bio-carbon materials from other biomass, thus providing a new way to develop carbon materials with more varied applications.

6.2 Experimental section

Materials synthesis: The carbonaceous precursor was prepared via a simple one-pot hydrothermal synthesis. Date pulp (10 g, purchased from a local supermarket in Perth, Australia) and $Co(NO_3)_2 \cdot 6H_2O$ (1 g, Sigma-Aldrich) were ground in ultrapure water using a ball mill (Pulverisette 6, Fritsch, Germany) at 400 rpm for 6 h. Then, the obtained suspension was decanted into a Teflon-lined stainless steel autoclave, and reacted at 150 °C for 12 h. The resulting black carbonaceous hydrogel monolith was heated under N_2 at 600 °C for 6 h to form the spherical bio-carbons with embedded metallic Co nanoparticles (Co-BCS). The Co-BCS was immersed in 0.5 M H_2SO_4 for 12 h to dissolve the metallic Co. The PBCS was then successfully prepared after filtration, washing with water, and drying. For comparison, bio-carbon spheres (BCS)

were also synthesized by the same procedure as that of Co-BCS except only the date pulp was used as the raw material.

Materials characterization: The X-ray diffraction (XRD) patterns were collected on a Bruker D8 Advance with Cu Kα radiation (λ = 0.15418 nm). The scanning electron microscopy (SEM) images were obtained on a Zeiss 1555 VP-FESEM. High-angle annular dark-field scanning transmission electron microscopy (HAADF-STEM) and energy dispersive X-ray (EDX) element mappings were taken using an FEI Titan G^2 80-200 TEM/STEM equipped with an EDX analyser. N_2 adsorption & desorption isotherms were obtained on a Micromeritics TriStar II instrument. The specific surface area (SSA) and the pore size distribution were acquired using Barrett-Emmett-Teller (BET) and Barrett-Joyner-Halenda (BJH) models based on the adsorption and desorption data, respectively. Raman spectra were recorded on an ISA dispersive Raman spectrometer. The X-ray photoelectron spectroscopy (XPS) measurements were performed on a Kratos Axis Ultra DLD spectrometer with a monochromatic Al Kα radiation source (1486.6 eV). The concentration of cobalt in PBCS was determined using an inductively coupled plasma-atomic emission spectrometer (ICP-OES, Optima 8300, PerkinElmer).

Electrochemical measurements: A three-electrode setup connected to a CHI 760E electrochemical workstation was used to conduct the electrochemical assessments. A glassy carbon rotating disk electrode (RDE, diameter of 0.5 cm, Pine Research Instrumentation, USA), a Pt wire and an Ag/AgCl (4 M KCl) electrode were employed as the working, counter and reference electrodes, respectively. The catalyst ink was formed by dispersing 10 mg of catalyst (BCS, Co-BCS, PBCS or commercial 20 wt% Pt/C from Alfa Aesar) in 1 mL of absolute ethanol with 100 μL of 5 wt% Nafion solution (Sigma-Aldrich) under sonication. A 10 μL aliquot of ink (or 5 μL of Pt/C ink) was dropped onto the surface of the working electrode, leading to a catalyst loading of ~ 0.464 mg cm^{-2} (~ 46 μg_{Pt} cm^{-2} for the Pt/C). The electrolyte was O_2-saturated 0.1 M KOH or 0.5 M H_2SO_4 solution. All measured potentials versus Ag/AgCl (4 M KCl) were calibrated to a reversible hydrogen electrode (RHE): $E_{RHE} = E_{Ag/AgCl} + 0.059pH + E^o_{Ag/AgCl}$ ($E^o_{Ag/AgCl}$ = 0.21 V at 20 °C). The electron transfer number of ORR was obtained from the Koutecky-Levich equation.[12]

6.3 Results and discussion

6.3.1Preparation and characterization of catalysts

To prepare PBCS, the first step was hydrothermal carbonization of the date pulp together with cobalt nitrate at 150 °C for 12 h (**Scheme 1**). The intermediate product was then pyrolyzed at 600 °C under flowing N_2 for 6 h to obtain the Co-BCS. The Co-BCS was further subjected to etching with 0.5 M H_2SO_4 solution to remove the accessible Co nanoparticles and simultaneously recover the cobalt. This resulted in the formation of hierarchically porous bio-carbon microspheres (PBCS).

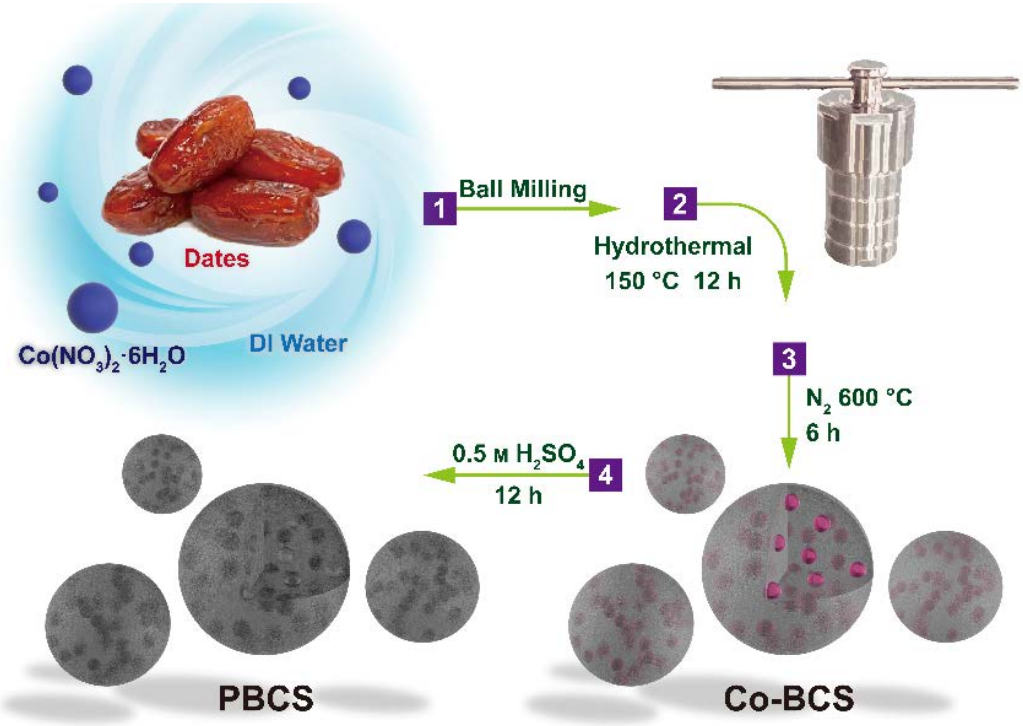

Scheme 1. Illustration of the fabrication of the PBCS.

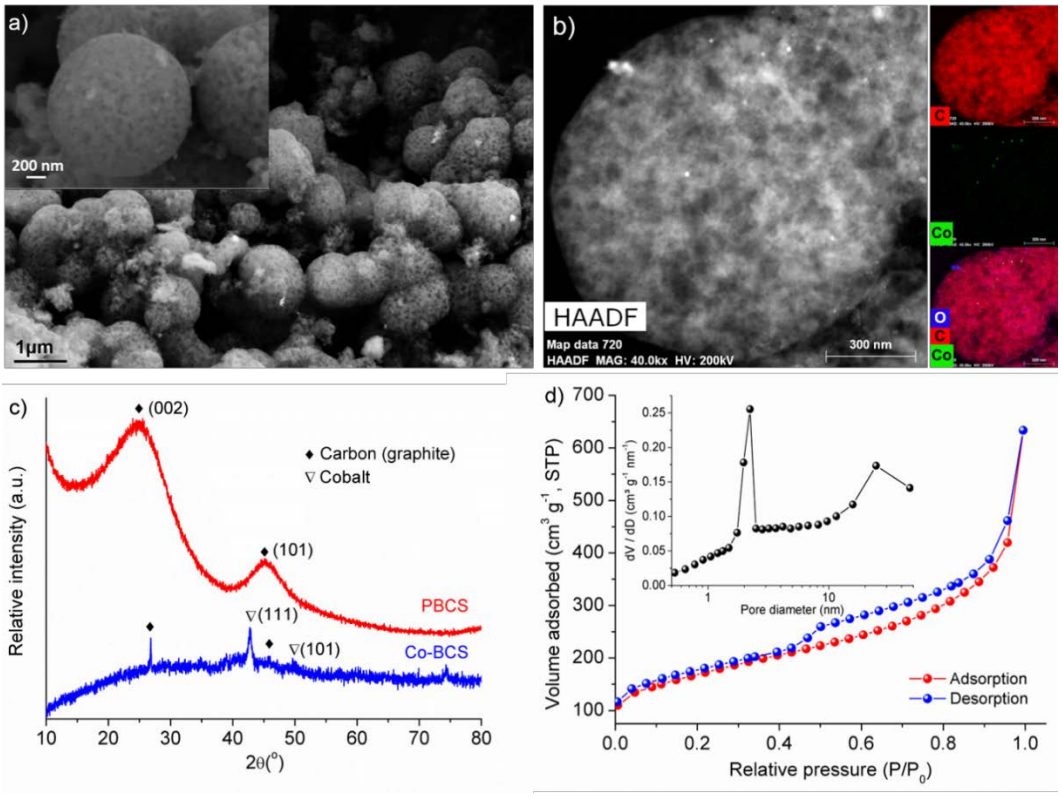

Figure 6.1 a) SEM images, b) STEM images and EDX elemental distribution of PBCS. c) XRD patterns of Co-BCS and PBCS. d) N_2 adsorption/desorption isotherm patterns of PBCS. Inset: the corresponding pore-size distribution curve generated from the adsorption data.

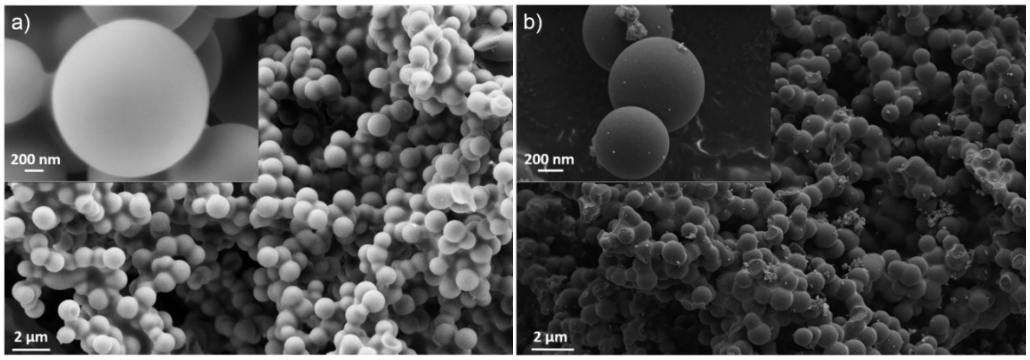

Figure 6.2 SEM images of a) BCS and b) Co-BCS.

The SEM image confirmed the spherical shape of the as-prepared PBCS showing an average diameter of ~1 μm (**Figure 6.1a**). Many fine pores can be observed on the rough surface of the microspheres with the diameter of approximately 100 nm, while the BCS shows a smooth surface without any observable pores (**Figure 6.2**). The porous microstructure of PBCS was further confirmed by the HAADF-STEM (**Figure 6.1b**). Such porous structures with abundant inner spaces can greatly facilitate the

diffusion of electrolytes into the interior of the PBCS microspheres resulting in a reduced diffusion resistance.[22, 41] Moreover, these structures may also provide more active sites for the redox reaction. These characteristics should be beneficial for ORR. The EDX elemental mappings of the PBCS microspheres clearly identified carbon as the main component and showed it had a uniform distribution. Interestingly, a trace amount of Co was also detected by EDX; this may be the residual cobalt that was trapped inside of the carbon matrix and could therefore not be removed by the acid treatment. The XRD pattern of the PBCS displays a pair of wide peaks at 2θ of approximately 24.8° and 45.0° corresponding to the (002) and (101) planes of graphite, respectively (**Figure 6.1c**). This demonstrates complete carbonization and formation of graphitic-like carbon with a good crystalline structure, which is crucial for high electrical conductivity. Unlike in the XRD pattern of Co-BCS, no peaks indicative of metallic Co were observed for the PBCS. This could be attributed to the negligible quantity of Co that was present being below the detection limit of XRD. The N_2 adsorption/desorption isotherms of PBCS exhibit typical type-IV isotherms based on a typical hysteresis loop, suggesting the presence of a mesoporous structure in the PBCS (**Figure 6.1d**). Correspondingly, two peaks at 2.2 and 24.6 nm were observed in the pore-size distribution curve. In combination with the macropores (~100 nm) observed in the microscopy images, this confirms the hierarchically porous nature of the PBCS. It has been reported that mesoporosity and/or macroporosity can facilitate the transfer of ORR-related species and thus enhance the ORR efficiency.[22, 42-44] Furthermore, a high BET-SSA of 564.8 m^2 g^{-1} is obtained for PBCS, which is beneficial for the availability of more active sites for ORR.[45, 46] Conversely, the BCS and Co-BCS samples show lower BET-SSA values of only 64.7 and 48.0 m^2 g^{-1}, respectively, with minimal porosity (**Figure 6.3**).

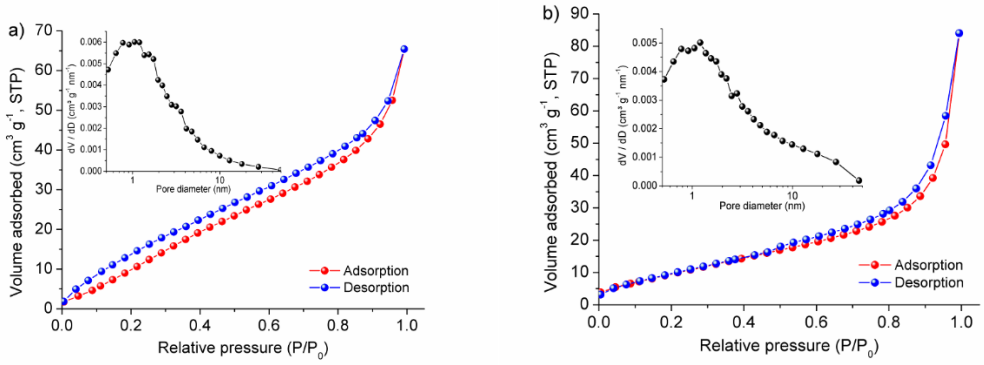

Figure 6.3 N_2 adsorption/desorption isotherm patterns of a) BCS and b) Co-BCS. Inset: the corresponding pore-size distribution curve derived from the adsorption branch.

6.3.2 Electrochemical performance of catalysts for the ORR

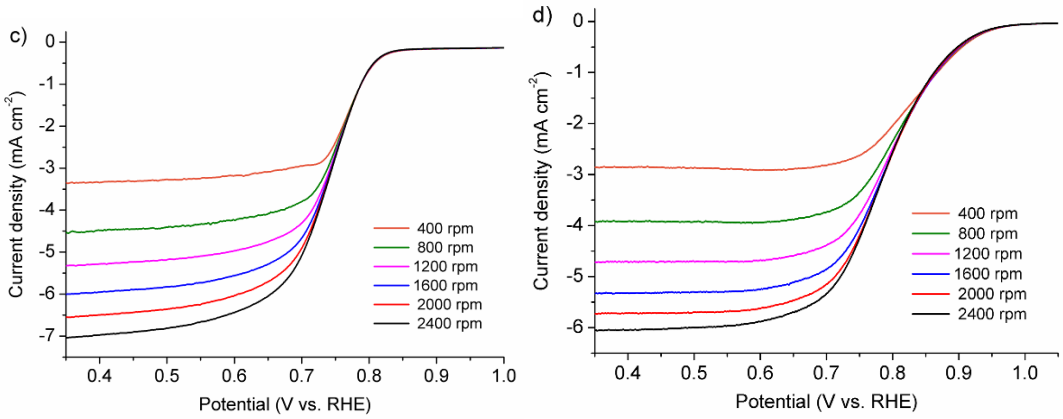

Figure 6.4 Linear sweep voltammogram (LSV) curves of a) BCS, b) Co-BCS, c) PBCS and d) commercial 20 wt% Pt/C on a rotating disk electrode (RDE) at different rotation rates in an O_2-saturated 0.1 M KOH solution at a scan rate of 5 mV s^{-1}.

The ORR activity of the as-prepared PBCS electrode was first tested in an O_2-saturated alkaline solution. For comparison, the performances of the Co-BCS and BCS samples were also investigated. Cyclic voltammetry (CV) curves (**Figure 6.5a**) reveal a distinct single oxygen reduction peak for the PBCS electrode at 0.66 V, which is substantially better than the BCS (0.51 V) and Co-BCS (0.52 V) electrodes. The maximum cathodic current density of PBCS was also much higher than that observed for the other two carbon-based catalysts. This demonstrates that the electrocatalytic activity of PBCS for the ORR is far better than that of Co-BCS and BCS. The ORR activity of the PBCS electrocatalyst was further tested by collecting linear sweep voltammetry (LSV) curves on a RDE at 1600 rpm. As shown in **Figure 6.5b**, Co-BCS presented ORR activity modestly better than that of BCS with respect to both limiting current density (J_L) and onset potential. Strikingly, the limiting current density of PBCS (-5.92 mA cm^{-2}) was much larger than that of the BCS (-1.35 mA cm^{-2}) and Co-BCS (-2.77 mA cm^{-2}) catalysts. In addition, under a practical fuel cell operating potential of ~ 0.7 V, the ORR current densities of PBCS and Pt/C catalysts are very close to each other. It should be noted that the electrochemical properties of Pt/C in our work are comparable to the results reported in the literature.[19, 21, 47-49] The presence of a wide current plateau for the PBCS electrode at a potential of < 0.65 V suggests a diffusion-controlled

process, much like what is reported for the Pt/C catalyst, implying an efficient four electrons process for the ORR over the PBCS electrocatalyst. All the aforementioned results demonstrate the outstanding ORR electrocatalytic performance of the as-prepared PBCS.

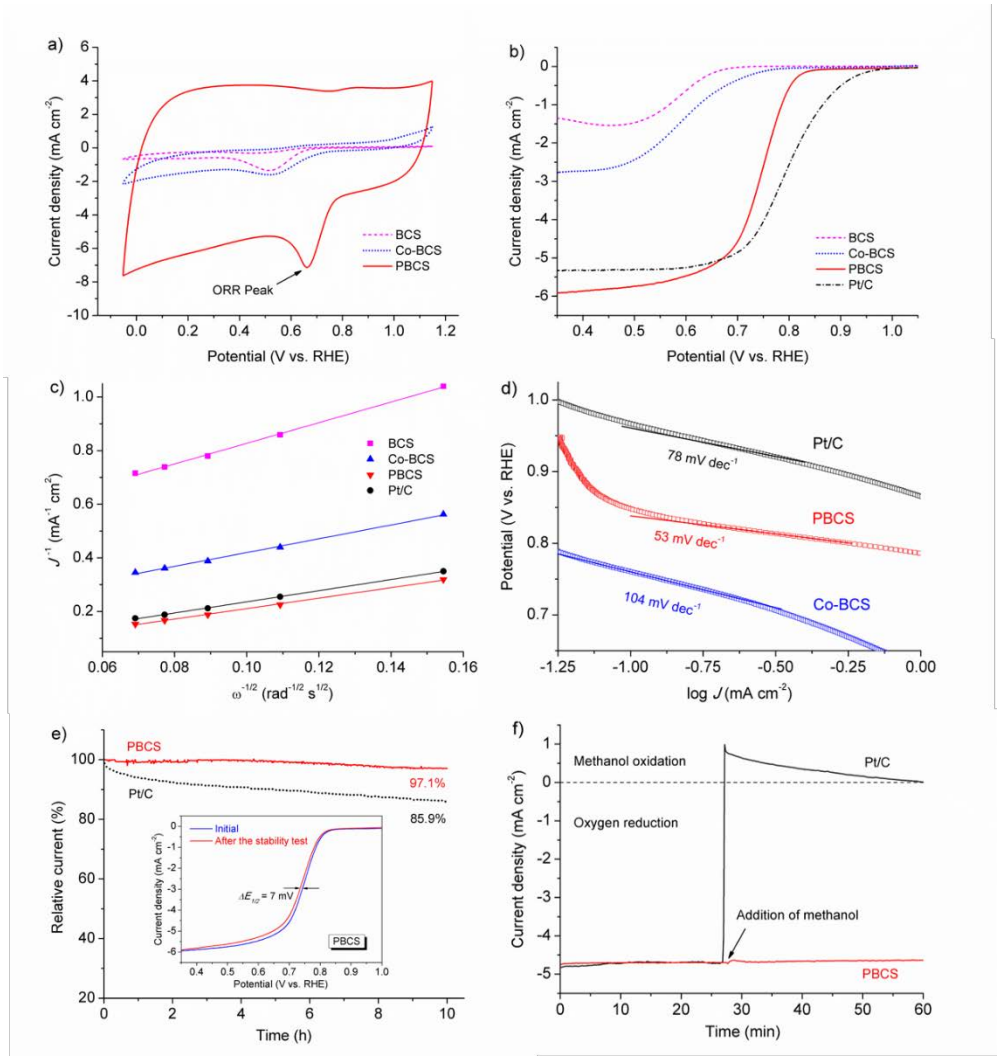

Figure 6.5. All the tests were conducted in O_2-saturated 0.1 M KOH. a) CV curves of the BCS, Co-BCS and PBCS at 100 mV s^{-1}. b) LSV curves of BCS, Co-BCS, PBCS and Pt/C at 5 mV s^{-1} on RDE at 1600 rpm. c) K-L plots of the catalysts at 0.35 V derived from Figure 6.4. d) Tafel plots of Co-BCS, PBCS and Pt/C based on the LSV curves in b). e) Chronoamperometric responses of PBCS and Pt/C at 0.55 V on RDE at 1600 rpm. Inset: LSVs of PBCS before and after the 10 h continuous polarization. f) Chronoamperometric responses of PBCS and Pt/C at 0.55 V on RDE at 1600 rpm in the electrolyte before (0-27 min) and after (27-60 min) the addition of 1 M methanol.

To gain deep insight into the electrocatalytic action and reaction kinetics of the as-prepared catalysts, we carried out Koutecky-Levich (K-L) analysis by collecting LSV curves at various rotation rates (**Figure 6.4**). The K-L plots for all the catalysts show good linearity (**Figure 6.5c**), indicating the ORR on these catalysts followed first order kinetics.[50] The fitting lines for the PBCS and Pt/C electrodes are almost parallel, and the electron transfer number per O_2 molecule was calculated to be ~4.0, signifying a 4-electron transfer ORR pathway over the as-prepared PBCS catalyst. It is relatively well established that the ORR on ordinary carbon materials is typically not a four-electron-transfer process.[28, 51] This finding further confirms the superior performance of PBCS for the ORR. Tafel plots of catalysts were prepared and are shown in **Figure 6.5d**. A lower Tafel slope suggests a better catalytic activity for ORR.[52] The Tafel slope for PBCS was 53 mV dec^{-1}, even lower than that of the popular Pt/C catalyst (78 mV dec^{-1}), and the PBCS slope falls into the lowest range of Tafel slopes observed for carbon-based electrocatalysts.[18, 31, 50, 53, 54] It is good evidence of the superb catalytic activity of PBCS for the ORR.

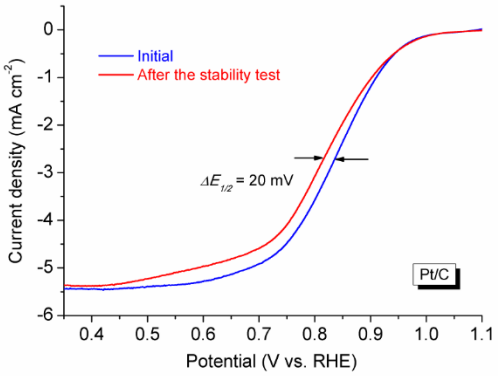

Figure 6.6 LSV curves of commercial 20 wt% Pt/C on an RDE (1600 rpm) in an O_2-saturated 0.1 M KOH solution at a scan rate of 5 mV s^{-1} before and after a continuous polarization period of 10 h.

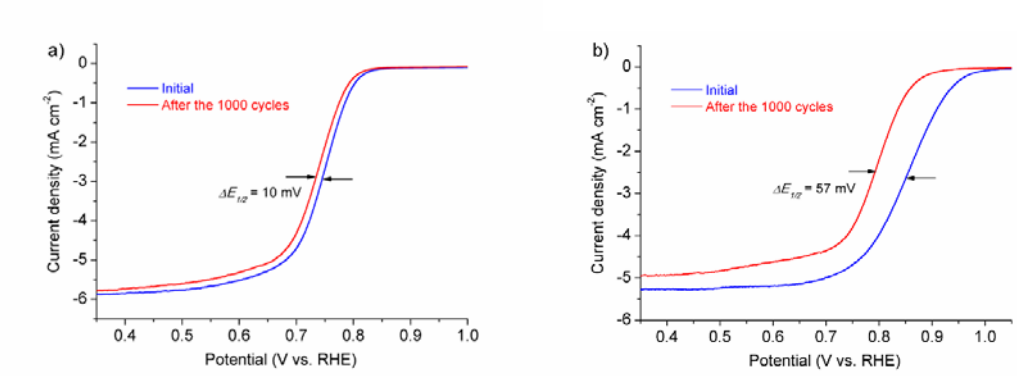

Figure 6.7 LSV curves of a) PBCS and b) commercial 20 wt% Pt/C on an RDE (1600 rpm) in an O_2-saturated 0.1 M KOH solution at a scan rate of 5 mV s^{-1} before and after the potential cycling stability test. The potential cycling was performed in the O_2-saturated 0.1 M KOH solution at a scan rate of 100 mV s^{-1} between 1.15 and 0.35 V vs. RHE for 1000 cycles.

In addition to cost and activity, stability is another important concern for the practical application of ORR electrocatalysts in real devices. The commercial Pt/C catalyst is reported to possess poor stability under certain operating conditions. In particular, Pt nanoparticles loaded onto carbon supports will readily aggregate, and in some instances even escape from the carbon support altogether causing a reduction in the number of active sites during the long-term operation.[19, 55, 56] The long-term stabilities of the PBCS and commercial Pt/C catalysts were comparatively assessed by monitoring their chronoamperometric responses at 0.55 V. As shown in **Figure 6.5e**, as expected, the current for the benchmark Pt/C catalyst continuously decreased over the whole test period, and only 85.9% of the initial current was retained after a 10 h test. In contrast, the PBCS was highly stable, with only a small current attenuation of 2.9% following the same 10 h testing duration. The LSV curves of the PBCS catalyst before and after the stability test (inset in **Figure 6.5e**) also demonstrated the favourable stability as seen in the very slight change in $E_{1/2}$ (7 mV), while a 20 mV drop in $E_{1/2}$ was found for the Pt/C catalyst over the course of the 10 h testing period (**Figure 6.6**). The cycle stability is another important performance metric to evaluate the practicality of an electrocatalyst. As shown in **Figure 6.7**, there was an inappreciable change in terms of $E_{1/2}$ (10 mV) for the PBCS catalyst after 1000 continuous potential cycles; however, a 57% loss of $E_{1/2}$ was observed for the Pt/C electrode. This further verifies the superior stability of the PBCS catalyst in alkaline conditions.

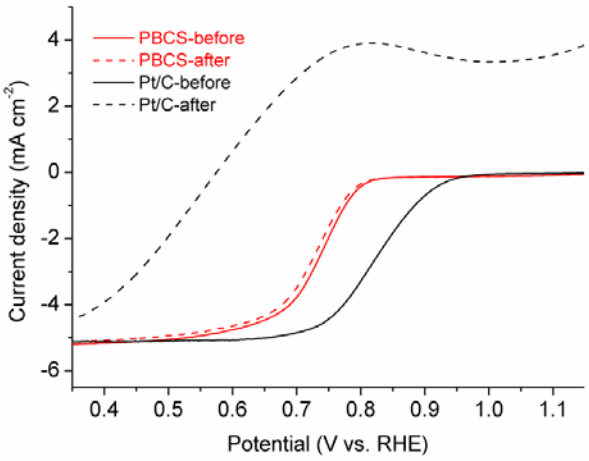

Figure 6.8 LSV curves of PBCS and commercial 20 wt% Pt/C on an RDE (1600 rpm) in an O_2-saturated 0.1 M KOH electrolyte at a scan rate of 5 mV s^{-1} before and after the addition of 1 M methanol.

Methanol crossover from the anode to the cathode is a well-known shortcoming for Pt-based electrocatalysts in direct methanol fuel cells.[57] To analyse this issue, we tested the methanol tolerance of the PSC catalyst (**Figure 6.5f**). Remarkably, the PBCS catalyst shows a stable cathodic ORR current after the introduction of methanol, suggesting the ORR activity of the PBCS catalyst is almost unaffected. Conversely, a dramatic current conversion from the cathodic current to the anodic current was observed once the methanol was added to the Pt/C electrode, indicating a rapid degradation of ORR activity due to methanol poisoning. LSV curves of both catalysts before and after the addition of methanol further validated that the PBCS catalyst had a much more robust methanol tolerance than that of traditional Pt/C catalyst (**Figure 6.8**).

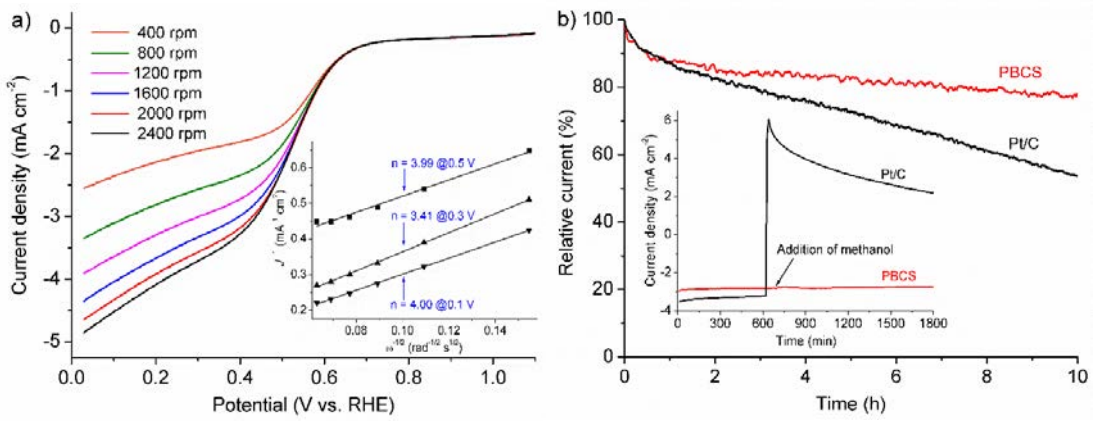

Figure 6.9. All the tests were carried out in O_2-saturated 0.5 M H_2SO_4. a) LSV curves of PBCS on RDE with various rotation rates. Inset: corresponding K-L plots at different potentials. b) Chronoamperometric responses of PBCS and Pt/C at 0.33 V on RDE at 1600 rpm. Inset: chronoamperometric responses of PBCS and Pt/C at 0.33 V on RDE at 1600 rpm in the electrolyte before (0-650 s) and after (650-1800 s) the addition of 1 M methanol.

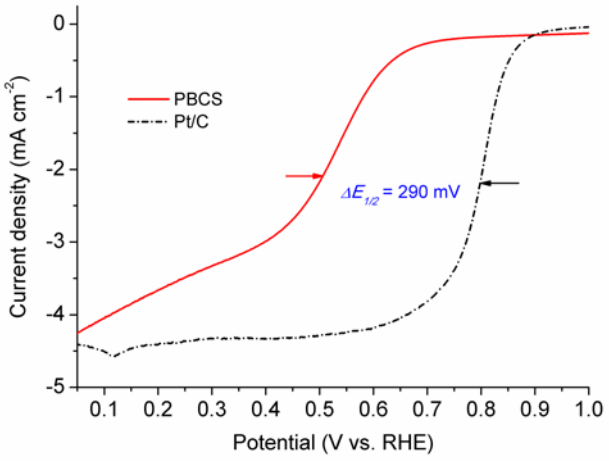

Fig. 6.10 LSV curves of PBCS and commercial 20 wt% Pt/C on an RDE (1600 rpm) in an O_2-saturated 0.5 M H_2SO_4 electrolyte at a scan rate of 5 mV s^{-1}.

Typically, ORR under acidic conditions is more difficult than it is in a basic electrolyte. The PBCS catalyst was further explored as a catalyst for ORR in an acidic medium, in a similar manner to its behaviour in alkaline conditions. The K-L plots (**Figure 6.9a**) exhibited good linearity over the entire potential range. The electron transfer number for ORR on PBCS was calculated to be ~4.0 from the slopes of K-L plots, hinting that the reaction is a $4e^-$ process in acidic conditions as well. Although the PBCS is not as good as Pt/C in terms of the onset potential and maximum current density (**Figure 6.10**), it still possesses great potential and competitiveness considering it is free of precious metals. Modification by doping with heteroatom(s) may further enhance the ORR activity of PBCS in acidic solutions. More importantly, the PBCS exhibited a greater stability and a more powerful resistance to methanol poisoning compared to the Pt/C catalyst (**Figure 6.9b**).

6.3.3 Mechanistic study for the enhanced performance of the PBCS

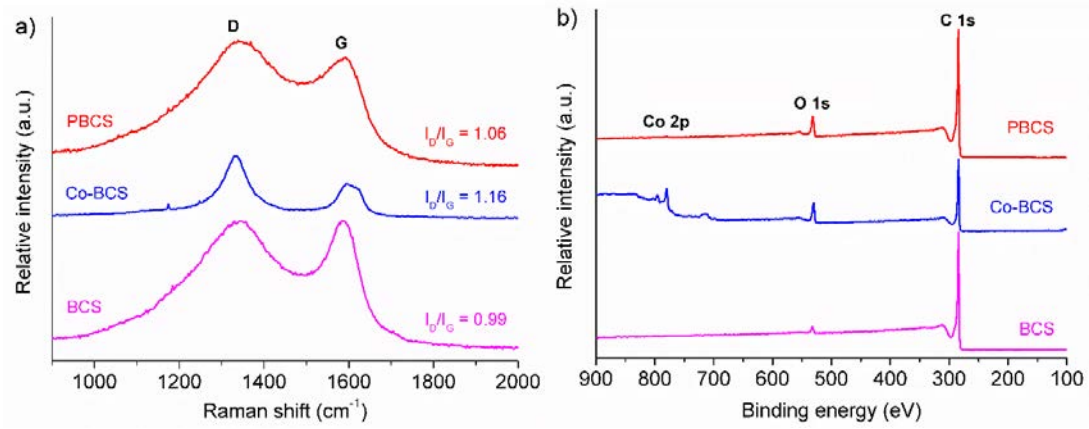

Figure 6.11 a) Raman spectra and b) XPS survey spectra of BCS, Co-BCS and PBCS.

An in-depth understanding of the superior ORR performance of PBCS will provide a solid foundation for future development and design of outstanding carbon-based electrocatalysts. It is generally accepted that pure ordinary carbon materials have relatively poor ORR activities, and carbon does not follow a 4-electron ORR pathway.[28, 51] As mentioned previously, several methods can be used to improve the activity of carbon materials for ORR. One is to incorporate other heteroatom(s) (such as N, S, B, and P) into the carbon lattice to alter the electronic structure of carbon thereby creating active sites for the ORR.[18-23, 25] It has been demonstrated that dopant nitrogen atoms can motivate neighbouring carbon atoms and promote oxygen adsorption and dissociation processes, both of which play dominate roles in ORR.[16, 23] It has been reported that date pulp contains only approximately 0.34% nitrogen ,[58] indicating that it is unlikely nitrogen-doped carbon will be generated from date pulp. The absence of nitrogen in the PBCS was also confirmed by the subsequent XPS analysis survey spectra (**Figure 6.11b**). This suggests that changes in the electronic structure due to nitrogen-doping are not the most likely origin of the high ORR performance of the PBCS.

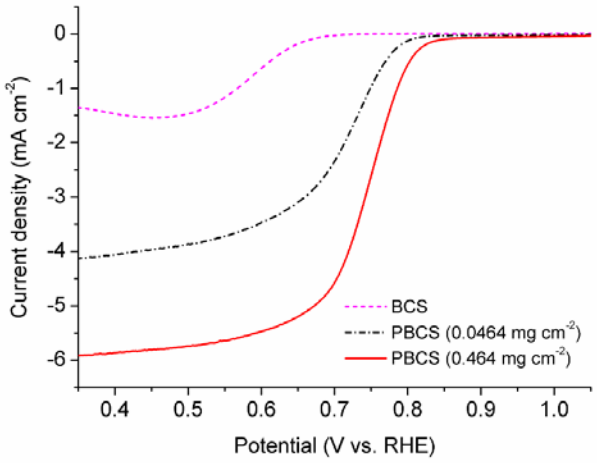

Figure 6.12 LSV curves of BCS and PBCS with different catalyst loadings in O_2-saturated 0.1 M KOH at a scan rate of 5 mV s^{-1} and a rotation speed of 1600 rpm.

For the BCS sample, which was prepared in the same manner as PBCS only without the presence of cobalt nitrate during the synthesis, it just showed a low ORR activity. However, a substantial increase in the activity was observed once cobalt was applied as the in situ template during the formation of PBCS (**Figure 6.5**). The fact that the PBCS possess much better electrochemical activity than the BCS highlights the role and contributing mechanisms of cobalt nanoparticles. As stated previously, the hierarchically porous structure will facilitate the penetration of the liquid electrolyte, resulting in vastly enhanced charge transfer. As a consequence, an improved catalytic activity for the ORR can be expected.[59] The BCS and Co-BCS showed BET-SSA values of 64.7 and 48.0 m^2 g^{-1}, respectively, and both of them showed the negligible pore volume (0.04 and 0.11 cm^3 g^{-1}, respectively). During the dissolution of cobalt from Co-BCS in the formation of PBCS, the BET-SSR significantly increased to 564.8 m^2 g^{-1} accompanying with a production of large pore volume (3.31 cm^3 g^{-1}). Clearly, the increased SSA should contribute to a certain degree to the enhanced catalytic activity in ORR, which will promote the increased number of active sites. To demonstrate whether the improved performance is solely due to the increase in active sites from the increased SSA, the ORR activity of PBCS was then tested with one tenth of the catalyst loading previously used. Although the catalytic activity of the PBCS with much lower catalyst loading (~0.0464 mg cm^{-2}) for ORR is moderately reduced compared to that of the normal catalyst loading (~0.464 mg cm^{-2}), it is still significantly better than that of BCS (**Figure 6.12**). This suggests an additional

reason(s) should contribute to the superior performance of the PBCS catalyst in addition to its high BET-SSA.

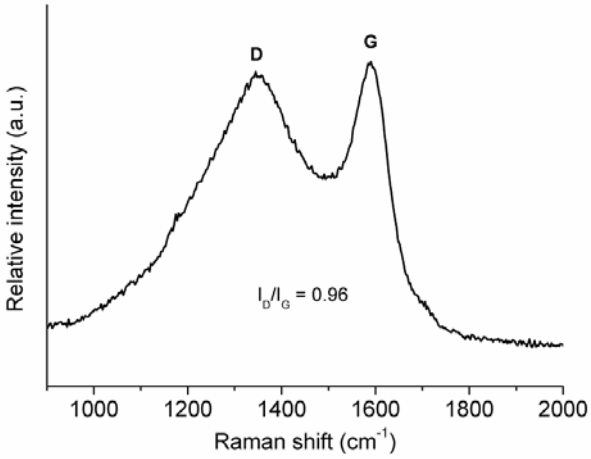

Figure 6.13 Raman spectrum of BCS after acid etching.

Raman spectra (**Figure 6.11a**) of all the samples displayed two characteristic peaks at 1350 (D band) and 1590 cm^{-1} (G band), which are typically assigned to the disordered/amorphous carbon or defect carbon and the graphitic carbon, respectively. The peak intensity ratio of the D and G bands (i.e., I_D/I_G) generally reflects the extent of disorder or defect degree in the carbon materials.[15, 17, 18, 21] The I_D/I_G ratios of 0.99, 1.16 and 1.06 were found for the BCS, Co-BCS and PBCS, respectively. Compared to the BCS, the I_D/I_G ratios of Co-BCS and PBCS were noticeably higher, implying the introduction of Co particles altered the structure of BCS and caused a high quantity of structural defects. Given that the acid etching could induce the loss of some amorphous carbon that may partially contribute to the decrease of I_D/I_G ratio of carbon material, the BCS sample was also subjected to the acid etching process for the same time as was used in preparing the PBCS. The I_D/I_G ratio was calculated to be 0.96 for the BCS after acid etching (**Figure 6.13**), demonstrating that the slightly smaller I_D/I_G ratio for the PBCS relative to that of the Co-BCS is likely due to the removal of some isolated amorphous carbon during the acid etching process. Typically, the presence of a small amount of transition metals in an organic precursor would promote graphitization during pyrolysis.[50, 59, 60] It is interesting that the I_D/I_G values for Co-BCS and PBCS are larger than that of BCS, indicating the larger amount of cobalt led to an increase in defects. It is generally accepted that amorphous carbon and graphitic carbon have poor activities in ORR;[23, 52] however, it has been reported that vacancy defects in the

dopant-free carbon are highly effective for the ORR due to unsaturation in the electronic structures of the active carbon atoms around the vacancy.[28] It is likely that the PBCS contain plenty of defects in the carbon structure, such defects were definitely inherited from the Co-BCS sample. The much poorer activity of Co-BSC relative to that of PBSC implies such defects are masked by the metallic cobalt. Once the cobalt was removed by acid etching, these defects were exposed to the liquid electrolyte and available for the catalytic reaction.

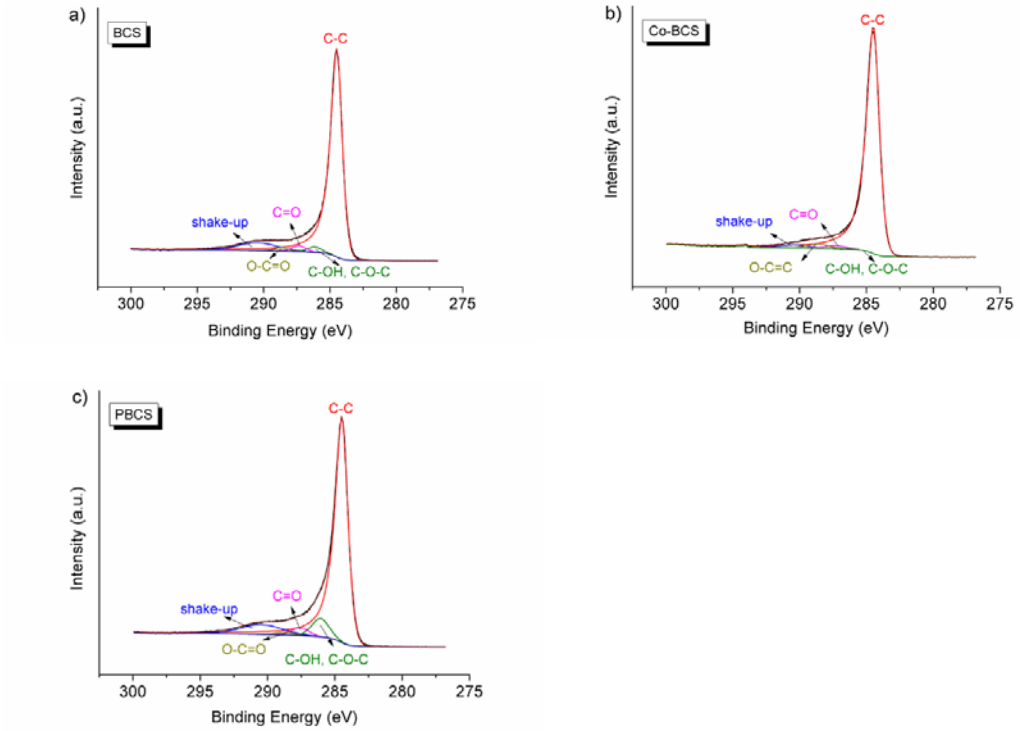

Figure. 6.14 High resolution C 1s XPS spectra of a) BCS, b) Co-BCS and c) PBCS.

Table 6.1 The relative concentration (at.%) of carbon, oxygen and cobalt from the XPS survey spectra of BCS, Co-BCS and PBCS.

Samples	C	O	Co
BCS	97.6	2.4	/
Co-BCS	85.0	10.1	4.9
PBCS	93.2	6.7	0.1

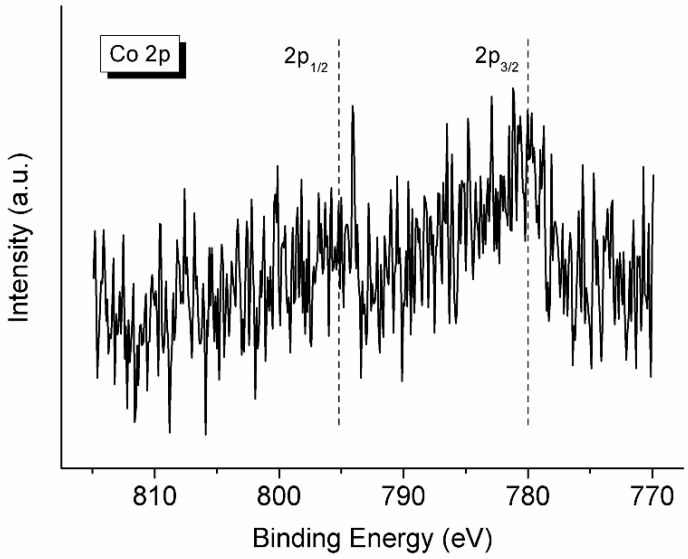

Figure. 6.15 High resolution Co 2p XPS spectrum of PBCS.

Further analyses of the as-obtained catalysts with XPS show that the relative atomic concentration of oxygen in both Co-BCS and PBCS is higher than that of BCS (**Figure 6.11b and Table 6.1**), suggesting a stronger O_2 adsorption on Co-BCS and PBCS. Since the ORR involves the adsorption of O_2 on the catalyst surface, a higher O_2 adsorption ability is beneficial for ORR.[61] A detailed analysis of the C 1s XPS spectra can be found in **Figure 6.14**, which further confirms that PBCS possessed more oxygen functional groups (summarised in **Table 6.2**) that provide extra chemical binding interactions with reactants during the ORR. Such oxygen functional groups on the surface of the PBCS are likely an indication of abundant exposed defects over the carbon. These defects are electron-deficient and prone to interact with oxygen or water from the surrounding atmosphere. In addition to C and O, the XPS survey and high-resolution Co 2p spectra of PBCS (**Figure 6.15**) reveal the presence of a trace amount of Co on the surface of the particles, in good agreement with previous EDX results. The Co content of PBCS was found to be 0.96 wt.% (equivalent to 0.20 at.%) based on the ICP-OES measurement. This is slightly larger than the value of 0.1 at.% obtained from the XPS analysis. We attribute this to the shallower probing depth of XPS. It has been demonstrated that trace levels of transition metal residues in the carbon matrix could enhance the electrocatalytic activity for the ORR owing to the electronic interaction between the metal nanoparticles and carbon support.[59, 62, 63] This may alter the electronic structure of the carbon materials and affect the catalytic activity for the ORR, which may provide additional enhancements for the activity of

PBCS. However, our material, the PBCS, shows a much better ORR performance than that of Co nanoparticles embedded in carbon materials that have been reported in the literature;[64, 65] PBCS even present a similar performance to cobalt particles modified heteroatom-doped carbons,[8, 43, 66] implying the effect of a small amount of residual metal is not the sole contributor to the superior ORR performance of the PBCS.

Table 6.2. The relative concentration (at.%) of species from the high-resolution C 1s XPS spectra of BCS, Co-BCS and PBCS.

Samples	C-C	C-OH, C-O-C	C=O	O-C=O
BCS	92.1	3.0	3.1	1.8
Co-BCS	95.3	0.0	1.9	2.8
PBCS	84.9	9.6	4.0	1.5

To this end, we explain the creation of this particular morphology of hierarchically porous carbon microspheres, the formation of rich surface defects, and the presence of a small amount of entrapped cobalt as follows. The date pulp is comprised mainly of sugar which contains a large amount of oxygen-containing groups. Such groups are rich in free electrons while cobalt ions contain vacant orbitals. The formation of a homogenous sugar-cobalt complex was realized through the strong interactions between free electrons of oxygenated groups in the sugar and the vacant orbitals of cobalt ions in the reactant system. Under the hydrothermal conditions, the sugar is progressively dehydrated to form a carbon precursor-cobalt composite. To minimize the surface energy, the composite preferentially grows in a microspherical shape. After calcination in an inert atmosphere at 600 °C, the pyrolysis of the precursor occurred and resulted in the formation of a carbon-cobalt composite. Due to the homogeneous mixing of cobalt and sugar in the hydrothermal synthesis stage, the cobalt was distributed with high homogeneity inside the carbon framework. The removal of the main portion of the cobalt from the composite through acidic etching subsequently created highly porous carbon microspheres. A small amount of cobalt was likely to be fully encapsulated by the carbon and was therefore retained as residual metal even after the acid etching process. Due to the formation of the sugar-cobalt complex during the hydrothermal process, the as-formed carbon and cobalt nanoparticles in the carbon-cobalt composite were in intimate contact. In other words, a certain kind of chemical interaction between carbon and cobalt was created at their interface. We proposed that the leaching of cobalt would expose a highly unsaturated carbon surface and introduce

abundant surface defects, which would then significantly promote the ORR in both basic and acidic media.

6.4 Conclusion

In summary, we have synthesized porous bio-carbon microspheres that exhibited the best ORR activity in alkaline solution among all reported heteroatom (N, B, P, S, etc.) dopant-free carbon materials. The ORR performance originates from the porous structure of the carbon surface, which greatly increased the concentration of active sites and benefited the mass and charge transport. This, coupled with the high specific surface area, the large number of vacancy defects and the trace quantity of remaining cobalt residue results in the superior ORR activity of the PBCS. Importantly, the resultant PBCS catalyst exhibited an outstanding stability and a robust tolerance to methanol crossover effects, beating the benchmark Pt/C catalyst in both alkaline and acidic conditions, making it a promising ORR catalyst to replace cathode in lithium air batteries and fuel cells.

6.5 Reference

[1] F.C. Handbook, Inc., Albuquerque, NM, DOE/NETL-2004/1206, (2004).

[2] L. Li, A. Manthiram, Advanced Energy Materials, 6 (2016) 201502054.

[3] P.-C. Li, C.-C. Hu, T.-H. You, P.-Y. Chen, Carbon, 111 (2017) 813-821.

[4] F. Cheng, J. Chen, Chemical Society Reviews, 41 (2012) 2172-2192.

[5] P.G. Bruce, S.A. Freunberger, L.J. Hardwick, J.-M. Tarascon, Nature Materials, 11 (2011) 19.

[6] E. Gileadi, Electrode kinetics for chemists, chemical engineers, and materials scientists, Capstone, 1993.

[7] E.J. Coleman, A.C. Co, ACS Catalysis, 5 (2015) 7299-7311.

[8] Z.-S. Wu, L. Chen, J. Liu, K. Parvez, H. Liang, J. Shu, H. Sachdev, R. Graf, X. Feng, K. Müllen, Advanced Materials, 26 (2014) 1450-1455.

[9] R. Bashyam, P. Zelenay, Nature, 443 (2006) 63.

[10] H.A. Gasteiger, N.M. Marković, Science, 324 (2009) 48.

[11] Z. Yang, X. Zhou, Z. Jin, Z. Liu, H. Nie, X.a. Chen, S. Huang, Advanced Materials, 26 (2014) 3156-3161.

[12] C. Su, T. Yang, W. Zhou, W. Wang, X. Xu, Z. Shao, Journal of Materials Chemistry A, 4 (2016) 4516-4524.

[13] Y. Zheng, Y. Jiao, Y. Zhu, Q. Cai, A. Vasileff, L.H. Li, Y. Han, Y. Chen, S.-Z. Qiao, Journal of the American Chemical Society, 139 (2017) 3336-3339.
[14] J. Suntivich, H.A. Gasteiger, N. Yabuuchi, H. Nakanishi, J.B. Goodenough, Y. Shao-Horn, Nature Chemistry, 3 (2011) 546.
[15] Y. Li, W. Zhou, H. Wang, L. Xie, Y. Liang, F. Wei, J.-C. Idrobo, S.J. Pennycook, H. Dai, Nature Nanotechnology, 7 (2012) 394.
[16] L. Dai, Y. Xue, L. Qu, H.-J. Choi, J.-B. Baek, Chemical Reviews, 115 (2015) 4823-4892.
[17] P. Zhang, F. Sun, Z. Xiang, Z. Shen, J. Yun, D. Cao, Energy & Environmental Science, 7 (2014) 442-450.
[18] A.M. El-Sawy, I.M. Mosa, D. Su, C.J. Guild, S. Khalid, R. Joesten, J.F. Rusling, S.L. Suib, Advanced Energy Materials, 6 (2016) 201501966.
[19] J. Wei, Y. Hu, Y. Liang, B. Kong, J. Zhang, J. Song, Q. Bao, G.P. Simon, S.P. Jiang, H. Wang, Advanced Functional Materials, 25 (2015) 5768-5777.
[20] J. Yang, H. Sun, H. Liang, H. Ji, L. Song, C. Gao, H. Xu, Advanced Materials, 28 (2016) 4606-4613.
[21] Y. Zheng, Y. Jiao, L. Ge, M. Jaroniec, S.Z. Qiao, Angewandte Chemie, 125 (2013) 3192-3198.
[22] X. Zheng, X. Cao, J. Wu, J. Tian, C. Jin, R. Yang, Carbon, 107 (2016) 907-916.
[23] D.-W. Wang, D. Su, Energy & Environmental Science, 7 (2014) 576-591.
[24] I. Hijazi, T. Bourgeteau, R. Cornut, A. Morozan, A. Filoramo, J. Leroy, V. Derycke, B. Jousselme, S. Campidelli, Journal of the American Chemical Society, 136 (2014) 6348-6354.
[25] H.-W. Liang, X. Zhuang, S. Brüller, X. Feng, K. Müllen, Nature Communications, 5 (2014) 4973.
[26] Y. Jia, L. Zhang, A. Du, G. Gao, J. Chen, X. Yan, C.L. Brown, X. Yao, Advanced Materials, 28 (2016) 9532-9538.
[27] X. Yan, Y. Jia, J. Chen, Z. Zhu, X. Yao, Advanced Materials, 28 (2016) 8771-8778.
[28] H. Zhao, C. Sun, Z. Jin, D.-W. Wang, X. Yan, Z. Chen, G. Zhu, X. Yao, Journal of Materials Chemistry A, 3 (2015) 11736-11739.
[29] M.C. Ortega-Liebana, N.X. Chung, R. Limpens, L. Gomez, J.L. Hueso, J. Santamaria, T. Gregorkiewicz, Carbon, 117 (2017) 437-446.

[30] M.-M. Titirici, R.J. White, N. Brun, V.L. Budarin, D.S. Su, F. del Monte, J.H. Clark, M.J. MacLachlan, Chemical Society Reviews, 44 (2015) 250-290.
[31] Z. Zhang, X. Gao, M. Dou, J. Ji, F. Wang, Journal of Materials Chemistry A, 5 (2017) 1526-1532.
[32] A. Aijaz, N. Fujiwara, Q. Xu, Journal of the American Chemical Society, 136 (2014) 6790-6793.
[33] F. Zheng, Y. Yang, Q. Chen, Nature Communications, 5 (2014) 5261.
[34] X. Zhai, P. Zhang, C. Liu, T. Bai, W. Li, L. Dai, W. Liu, Chemical Communications, 48 (2012) 7955-7957.
[35] J.A. Maciá-Agulló, M. Sevilla, M.A. Diez, A.B. Fuertes, ChemSusChem, 3 (2010) 1352-1354.
[36] X.-X. Lin, B. Tan, L. Peng, Z.-F. Wu, Z.-L. Xie, Journal of Materials Chemistry A, 4 (2016) 4497-4505.
[37] H. Wu, J. Geng, H. Ge, Z. Guo, Y. Wang, G. Zheng, Advanced Energy Materials, 6 (2016) 201600794.
[38] L. Zhao, L.-Z. Fan, M.-Q. Zhou, H. Guan, S. Qiao, M. Antonietti, M.-M. Titirici, Advanced Materials, 22 (2010) 5202-5206.
[39] J. Wei, Y. Liang, Y. Hu, B. Kong, G.P. Simon, J. Zhang, S.P. Jiang, H. Wang, Angewandte Chemie, 128 (2016) 1377-1381.
[40] S. De, A.M. Balu, J.C. van der Waal, R. Luque, ChemCatChem, 7 (2015) 1608-1629.
[41] H. Yu, L. Shang, T. Bian, R. Shi, G.I.N. Waterhouse, Y. Zhao, C. Zhou, L.-Z. Wu, C.-H. Tung, T. Zhang, Advanced Materials, 28 (2016) 5080-5086.
[42] M. Xiao, J. Zhu, L. Feng, C. Liu, W. Xing, Advanced Materials, 27 (2015) 2521-2527.
[43] J. Yu, G. Chen, J. Sunarso, Y. Zhu, R. Ran, Z. Zhu, W. Zhou, Z. Shao, Advanced Science, 3 (2016) 201600060.
[44] W. Wei, H. Liang, K. Parvez, X. Zhuang, X. Feng, K. Müllen, Angewandte Chemie, 126 (2014) 1596-1600.
[45] Z.-Y. Wu, X.-X. Xu, B.-C. Hu, H.-W. Liang, Y. Lin, L.-F. Chen, S.-H. Yu, Angewandte Chemie, 127 (2015) 8297-8301.
[46] Z.-L. Wang, D. Xu, H.-X. Zhong, J. Wang, F.-L. Meng, X.-B. Zhang, Science Advances, 1 (2015).

[47] G.A. Ferrero, K. Preuss, A. Marinovic, A.B. Jorge, N. Mansor, D.J.L. Brett, A.B. Fuertes, M. Sevilla, M.-M. Titirici, ACS Nano, 10 (2016) 5922-5932.
[48] Y. Zhu, W. Zhou, Y. Chen, J. Yu, X. Xu, C. Su, M.O. Tadé, Z. Shao, Chemistry of Materials, 27 (2015) 3048-3054.
[49] J. Zhang, Z. Zhao, Z. Xia, L. Dai, Nature Nanotechnology, 10 (2015) 444.
[50] Y. Hou, T. Huang, Z. Wen, S. Mao, S. Cui, J. Chen, Advanced Energy Materials, 4 (2014) 201400337.
[51] S. Wang, D. Yu, L. Dai, Journal of the American Chemical Society, 133 (2011) 5182-5185.
[52] J. Zhang, PEM fuel cell electrocatalysts and catalyst layers: fundamentals and applications, Springer Science & Business Media, 2008.
[53] W. Tian, H. Zhang, H. Sun, A. Suvorova, M. Saunders, M. Tade, S. Wang, Advanced Functional Materials, 26 (2016) 8651-8661.
[54] L. Ge, Y. Yang, L. Wang, W. Zhou, R. De Marco, Z. Chen, J. Zou, Z. Zhu, Carbon, 82 (2015) 417-424.
[55] J.C. Meier, I. Katsounaros, C. Galeano, H.J. Bongard, A.A. Topalov, A. Kostka, A. Karschin, F. Schuth, K.J.J. Mayrhofer, Energy & Environmental Science, 5 (2012) 9319-9330.
[56] M.K. Debe, Nature, 486 (2012) 43.
[57] V. Neburchilov, J. Martin, H. Wang, J. Zhang, Journal of Power Sources, 169 (2007) 221-238.
[58] N. Kacem-Chaouche, L. Dehimat, Z. Meraihi, J. Destain, K. Kahlat, P. Thonart, Agriculture and Biology Journal of North America, (2013).
[59] B.Y. Xia, Y. Yan, N. Li, H.B. Wu, X.W. Lou, X. Wang, Nature Energy, 1 (2016) 15006.
[60] P. Su, H. Xiao, J. Zhao, Y. Yao, Z. Shao, C. Li, Q. Yang, Chemical Science, 4 (2013) 2941-2946.
[61] L. Qu, Y. Liu, J.-B. Baek, L. Dai, ACS Nano, 4 (2010) 1321-1326.
[62] L. Wang, A. Ambrosi, M. Pumera, Angewandte Chemie International Edition, 52 (2013) 13818-13821.
[63] J. Masa, A. Zhao, W. Xia, Z. Sun, B. Mei, M. Muhler, W. Schuhmann, Electrochemistry Communications, 34 (2013) 113-116.
[64] J. Ryu, N. Jung, D.-H. Lim, D.Y. Shin, S.H. Park, H.C. Ham, J.H. Jang, H.-J. Kim, S.J. Yoo, Chemical Communications, 50 (2014) 15940-15943.

[65] W. Xia, R. Zou, L. An, D. Xia, S. Guo, Energy & Environmental Science, 8 (2015) 568-576.
[66] G. Wu, K.L. More, C.M. Johnston, P. Zelenay, Science, 332 (2011) 443.

Chapter 7 Conclusions and Recommendations

7.1 Conclusions

Lithium batteries and supercapacitors have emerged as alternative energy storage devices for improving the development of new and green energy. Typically, the mechanism of the lithium batteries is based on the reversible movement of Li ion between the intercalation compound at the anode and the cathode side. However, the fast electron storage of supercapacitors, including both the electrochemical double layer capacitors (EDLC) and the transition metal oxides pseudo-capacitive devices, functions according to the fast and reversible surface and near-surface reaction. To address this, a new type of supercapacitor which utilizes the cation (e.g. Li^+) charge storage was developed, reaching a better energy density and mitigating the weakness compared to lithium ion batteries. Except for the improvement of capacitance, another advantage of intercalation type supercapacitors lies in that their performance is not theoretically limited by surface reactions or structures, but instead determined by the bulk crystalline structure of the electrode. Oxygen reduction reaction (ORR) mechanism and the design principles of highly active ORR catalysts are critical to improve the discharge performance, which directly affects the deliverable gravimetric energy and power of Li-air batteries. In this thesis, novel perovskite oxide electrode materials and spinal oxide nanosized electrode materials are developed to be used as the electrode in pseudocapacitor. In addition, bio-carbon microspheres from natural date pulp and their use as an exceedingly active and stable ORR electrocatalyst under both basic and acidic conditions are also reported. The following general conclusions have been derived from these studies.

7.1.1 Design of perovskite oxides as anion-intercalation-type electrodes for supercapacitors: cation leaching effect

- $SrCoO_{3-\delta}$, $Ba_{0.5}Sr_{0.5}Co_{0.8}Fe_{0.2}O_{3-\delta}$, and Co_3O_4 as electrodes are studied in supercapacitors with aqueous alkaline electrolyte.
- The poor stability of $Ba_{0.5}Sr_{0.5}Co_{0.8}Fe_{0.2}O_{3-\delta}$ electrode in pseudocapacitor resulted from the significant leaching of Ba^{2+} and Sr^{2+} in alkaline solution during cycling, which destroyed the perovskite structure seriously.
- The effect of interaction between the electrode materials with the alkaline solution was focused on the structure and specific surface area of the

electrode material, and ultimately the electrochemical performance is emphasized.

- $SrCoO_{3-\delta}$ is a promising electrode candidate for practical use in supercapacitors. Stabilizing its oxygen-vacancy-disordered cubic phase through doping strategy by using a dopant other than Ba^{2+} could be a useful way to further improve the electrode performance of $SrCoO_{3-\delta}$ in the future.

7.1.2 Highly defective layered double perovskite oxide for efficient energy storage via reversible pseudocapacitive oxygen-anion intercalation

- Perovskite electrode materials in supercapacitor are characterized by high oxygen vacancy concentrations, and do not require high surface areas to achieve a high energy storage capacity as a result of the bulk intercalation mechanism.
- Reduced $PrBaMn_2O_{6-\delta}$, with a layered double perovskite structure, exhibits ultrahigh capacitance and functions as an excellent oxygen anion-intercalation-type electrode material for supercapacitors.
- As demonstrated by the experimental results and DFT calculations, the introduction of a higher oxygen vacancy concentration into the $PrBaMn_2O_{6-\delta}$ lattice after reduction results in improved electrochemical properties, especially the intercalation pseudocapacitive charge storage.

7.1.3 Molecular design of mesoporous $NiCo_2O_4$ and $NiCo_2S_4$ with sub-micrometer-polyhedron architectures for efficient pseudocapacitive energy storage

- Spinel-type $NiCo_2O_4$ and $NiCo_2S_4$ polyhedron architectures with sizes of 500–600 nm and rich mesopores with diameters of 1–2 nm are prepared facilely by the molecular design of Ni and Co into polyhedron-shaped zeolitic imidazolate frameworks as solid precursors.
- Both as-prepared NCO and NCS nanostructures exhibit excellent pseudocapacitance and stability as electrodes in supercapacitors.
- The specific capacitance of the ZIF–NCS nanoparticles reached 1296, 1260, 1226 and 1208 F g^{-1} at current densities of 1, 2, 5, and 10 A g^{-1}, respectively, which are among the best results for self-supported NiCo-based electrodes available in literature.

- This simple method using ZIFs as a precursor for the fabrication of porous composite oxides or composite sulphides could be easily extended to the preparation of other porous metal oxides or sulphides in the application of supercapacitors.

7.1.4 Hierarchically porous bio-carbon microspheres derived from natural date pulp as efficient and stable oxygen-reduction electrocatalysts

- Hierarchically porous bio-carbon microspheres are fabricated and used as highly active and stable electrocatalysts for oxygen reduction reaction under both alkaline and acidic conditions.
- The ORR performance originates from the porous structure of the carbon surface, which greatly increased the concentration of active sites and benefited the mass and charge transport.
- The catalysts yield competitive catalytic activity (a small Tafel slope of 53 mV dec^{-1}) and superb durability and methanol tolerance compared to the benchmark Pt/C catalyst in an alkaline electrolyte.

7.2 Recommendations

Despite the progress achieved in this thesis, future work is still required to design, fabricate, and undertake numerical study of normal pseudocapacitor oxygen ion intercalation type supercapacitors with a) improved electrode materials with high oxygen-vacancy concentration; b) increased specific capacitance and stable performance for long-term operation; c) high electron storage ability under fast current density charging conditions; d) reduced leaching effect on the stability of crystal structure of electrode materials. The perovskite oxide electrodes and alkaline electrolytes are adopted, and innovative oxygen ion intercalation type supercapacitors will be developed. Under alkaline electrolytes, oxygen vacancies are filled through intercalation of an electrolyte oxygen ion and diffusion of O^{2-} along octahedral edges through the crystal concomitant with the oxidation of cations in perovskite structures. This energy storage mechanism of anion intercalation supercapacitor not only occurs via the surface redox reaction for electron storage, but also by the bulk reaction. In addition, So far, the most stable catalysts in ORR are those made with a pre-existing carbon support to host the catalytic sites. Their performance still needs to be improved

to reach that of Pt catalysts, and their production cost needs to be drastically decreased to a very small fraction of the Pt catalyst production cost

Appendix: Permission of Reproduction from the Copyright Owner

ELSEVIER LICENSE
TERMS AND CONDITIONS

Nov 19, 2017

This Agreement between Mr. YU LIU ("You") and Elsevier ("Elsevier") consists of your license details and the terms and conditions provided by Elsevier and Copyright Clearance Center.

License Number	4232820203851
License date	Nov 19, 2017
Licensed Content Publisher	Elsevier
Licensed Content Publication	Journal of Power Sources
Licensed Content Title	Carbon properties and their role in supercapacitors
Licensed Content Author	A.G. Pandolfo,A.F. Hollenkamp
Licensed Content Date	Jun 19, 2006
Licensed Content Volume	157
Licensed Content Issue	1
Licensed Content Pages	17
Start Page	11
End Page	27
Type of Use	reuse in a thesis/dissertation
Portion	figures/tables/illustrations
Number of figures/tables/illustrations	1
Format	both print and electronic
Are you the author of this Elsevier article?	No
Will you be translating?	No
Original figure numbers	Figure 1.
Title of your thesis/dissertation	The development of the novel electrode materials for supercapacitors and lithium based batteries
Expected completion date	Jan 2018
Estimated size (number of pages)	200
Requestor Location	Mr. YU LIU Room 3113 B500 Curtin University, Bently Perth, WA 6102 Australia Attn: Mr. YU LIU
Total	0.00 AUD

Terms and Conditions

INTRODUCTION

1. The publisher for this copyrighted material is Elsevier. By clicking "accept" in connection with completing this licensing transaction, you agree that the following terms and conditions apply to this transaction (along with the Billing and Payment terms and conditions established by Copyright Clearance Center, Inc. ("CCC"), at the time that you opened your Rightslink account and that are available at any time at http://myaccount.copyright.com).

Title: Pseudocapacitive oxide materials for high-rate electrochemical energy storage
Author: Veronica Augustyn,Patrice Simon,Bruce Dunn
Publication: Energy & Environmental Science
Publisher: Royal Society of Chemistry
Date: Mar 13, 2014

Order Completed

Thank you for your order.

This Agreement between Mr. YU LIU ("You") and Royal Society of Chemistry ("Royal Society of Chemistry") consists of your license details and the terms and conditions provided by Royal Society of Chemistry and Copyright Clearance Center.

Your confirmation email will contain your order number for future reference.

printable details

License Number	4236770077909
License date	Nov 26, 2017
Licensed Content Publisher	Royal Society of Chemistry
Licensed Content Publication	Energy & Environmental Science
Licensed Content Title	Pseudocapacitive oxide materials for high-rate electrochemical energy storage
Licensed Content Author	Veronica Augustyn,Patrice Simon,Bruce Dunn
Licensed Content Date	Mar 13, 2014
Licensed Content Volume	7
Licensed Content Issue	5
Type of Use	Thesis/Dissertation
Requestor type	academic/educational
Portion	figures/tables/images
Number of figures/tables/images	2
Distribution quantity	10
Format	print and electronic
Will you be translating?	no
Order reference number	
Title of the thesis/dissertation	The development of the novel electrode materials for supercapacitors and lithium based batteries
Expected completion date	Jan 2018
Estimated size	200
Requestor Location	Mr. YU LIU Room 3113 B500 Curtin University, Bently Perth, WA 6102 Australia Attn: Mr. YU LIU
Billing Type	Invoice
Billing address	Mr. YU LIU Room 3113 B500 Curtin University, Bently

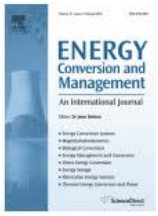

Title:	A review on electrochemical double-layer capacitors
Author:	Pawan Sharma,T.S. Bhatti
Publication:	Energy Conversion and Management
Publisher:	Elsevier
Date:	December 2010

Order Completed

Thank you for your order.

This Agreement between Mr. YU LIU ("You") and Elsevier ("Elsevier") consists of your license details and the terms and conditions provided by Elsevier and Copyright Clearance Center.

Your confirmation email will contain your order number for future reference.

printable details

License Number	4236770355139
License date	Nov 26, 2017
Licensed Content Publisher	Elsevier
Licensed Content Publication	Energy Conversion and Management
Licensed Content Title	A review on electrochemical double-layer capacitors
Licensed Content Author	Pawan Sharma,T.S. Bhatti
Licensed Content Date	Dec 1, 2010
Licensed Content Volume	51
Licensed Content Issue	12
Licensed Content Pages	12
Type of Use	reuse in a thesis/dissertation
Portion	figures/tables/illustrations
Number of figures/tables/illustrations	1
Format	both print and electronic
Are you the author of this Elsevier article?	No
Will you be translating?	No
Original figure numbers	Fig. 3
Title of your thesis/dissertation	The development of the novel electrode materials for supercapacitors and lithium based batteries
Expected completion date	Jan 2018
Estimated size (number of pages)	200
Requestor Location	Mr. YU LIU Room 3113 B500 Curtin University, Bently Perth, WA 6102 Australia Attn: Mr. YU LIU
Total	0.00 AUD

ORDER MORE CLOSE WINDOW

Copyright Clearance Center

Confirmation Number: 11683287
Order Date: 11/26/2017

Customer Information

Customer: YU LIU
Account Number: 3001219679
Organization: YU LIU
Email: yu.liu13@postgrad.curtin.edu.au
Phone: +61 92665602
Payment Method: Invoice

This is not an invoice

Order Details

Nanotechnology

Billing Status: **N/A**

Order detail ID: 70802894
ISSN: 0957-4484
Publication Type: Journal
Volume:
Issue:
Start page:
Publisher: IOP Publishing

Permission Status: Granted
Permission type: Republish or display content
Type of use: Thesis/Dissertation
Order License Id: 4236771052897

Requestor type	Academic institution
Format	Print, Electronic
Portion	chart/graph/table/figure
Number of charts/graphs/tables/figures	1
The requesting person/organization	YU LIU/Curtin university
Title or numeric reference of the portion(s)	Figure 3
Title of the article or chapter the portion is from	N/A
Editor of portion(s)	N/A
Author of portion(s)	N/A
Volume of serial or monograph	N/A
Page range of portion	200
Publication date of portion	2018
Rights for	Main product and any product related to main product
Duration of use	Life of current and all future editions
Creation of copies for the disabled	no
With minor editing privileges	no
For distribution to	Worldwide
In the following language(s)	Original language of publication
With incidental promotional use	no
Lifetime unit quantity of new product	Up to 9,999

Title:	Facilely synthesized porous NiCo2O4 flowerlike nanostructure for high-rate supercapacitors
Author:	Haichao Chen,Jianjun Jiang,Li Zhang,Tong Qi,Dandan Xia,Houzhao Wan
Publication:	Journal of Power Sources
Publisher:	Elsevier
Date:	15 February 2014

Order Completed

Thank you for your order.

This Agreement between Mr. YU LIU ("You") and Elsevier ("Elsevier") consists of your license details and the terms and conditions provided by Elsevier and Copyright Clearance Center.

Your confirmation email will contain your order number for future reference.

printable details

License Number	4236771322055
License date	Nov 26, 2017
Licensed Content Publisher	Elsevier
Licensed Content Publication	Journal of Power Sources
Licensed Content Title	Facilely synthesized porous NiCo2O4 flowerlike nanostructure for high-rate supercapacitors
Licensed Content Author	Haichao Chen,Jianjun Jiang,Li Zhang,Tong Qi,Dandan Xia,Houzhao Wan
Licensed Content Date	Feb 15, 2014
Licensed Content Volume	248
Licensed Content Issue	n/a
Licensed Content Pages	9
Type of Use	reuse in a thesis/dissertation
Portion	figures/tables/illustrations
Number of figures/tables/illustrations	1
Format	both print and electronic
Are you the author of this Elsevier article?	No
Will you be translating?	No
Original figure numbers	Figure 4
Title of your thesis/dissertation	The development of the novel electrode materials for supercapacitors and lithium based batteries
Expected completion date	Jan 2018
Estimated size (number of pages)	200
Requestor Location	Mr. YU LIU Room 3113 B500 Curtin University, Bently Perth, WA 6102 Australia Attn: Mr. YU LIU
Total	0.00 AUD

ORDER MORE CLOSE WINDOW

Order Completed

Thank you for your order.

This Agreement between Mr. YU LIU ("You") and Nature Publishing Group ("Nature Publishing Group") consists of your license details and the terms and conditions provided by Nature Publishing Group and Copyright Clearance Center.

Your confirmation email will contain your order number for future reference.

printable details

License Number	4236780022016
License date	Nov 26, 2017
Licensed Content Publisher	Nature Publishing Group
Licensed Content Publication	Nature Materials
Licensed Content Title	The light and shade of perovskite solar cells
Licensed Content Author	Michael Grätzel
Licensed Content Date	Aug 21, 2014
Licensed Content Volume	13
Licensed Content Issue	9
Type of Use	reuse in a dissertation / thesis
Requestor type	academic/educational
Format	print and electronic
Portion	figures/tables/illustrations
Number of figures/tables/illustrations	1
High-res required	no
Figures	Figure 1
Author of this NPG article	no
Your reference number	
Title of your thesis / dissertation	The development of the novel electrode materials for supercapacitors and lithium based batteries
Expected completion date	Jan 2018
Estimated size (number of pages)	200
Requestor Location	Mr. YU LIU Room 3113 B500 Curtin University, Bently Perth, WA 6102 Australia Attn: Mr. YU LIU
Billing Type	Invoice
Billing address	Mr. YU LIU Room 3113 B500 Curtin University, Bently Perth, Australia 6102 Attn: Mr. YU LIU
Total	0.00 AUD

ORDER MORE CLOSE WINDOW

Title:	A 2 B′B″O6 perovskites: A review
Author:	Sami Vasala,Maarit Karppinen
Publication:	Progress in Solid State Chemistry
Publisher:	Elsevier
Date:	May 2015

Order Completed

Thank you for your order.

This Agreement between Mr. YU LIU ("You") and Elsevier ("Elsevier") consists of your license details and the terms and conditions provided by Elsevier and Copyright Clearance Center.

Your confirmation email will contain your order number for future reference.

printable details

License Number	4236780155888
License date	Nov 26, 2017
Licensed Content Publisher	Elsevier
Licensed Content Publication	Progress in Solid State Chemistry
Licensed Content Title	A 2 B′B″O6 perovskites: A review
Licensed Content Author	Sami Vasala,Maarit Karppinen
Licensed Content Date	May 1, 2015
Licensed Content Volume	43
Licensed Content Issue	1-2
Licensed Content Pages	36
Type of Use	reuse in a thesis/dissertation
Portion	figures/tables/illustrations
Number of figures/tables/illustrations	1
Format	both print and electronic
Are you the author of this Elsevier article?	No
Will you be translating?	No
Original figure numbers	figure 1
Title of your thesis/dissertation	The development of the novel electrode materials for supercapacitors and lithium based batteries
Expected completion date	Jan 2018
Estimated size (number of pages)	200
Requestor Location	Mr. YU LIU Room 3113 B500 Curtin University, Bently Perth, WA 6102 Australia Attn: Mr. YU LIU
Total	0.00 AUD

ORDER MORE CLOSE WINDOW

Order Completed

Thank you for your order.

This Agreement between Mr. YU LIU ("You") and Nature Publishing Group ("Nature Publishing Group") consists of your license details and the terms and conditions provided by Nature Publishing Group and Copyright Clearance Center.

Your confirmation email will contain your order number for future reference.

printable details

License Number	4236780343118
License date	Nov 26, 2017
Licensed Content Publisher	Nature Publishing Group
Licensed Content Publication	Nature Materials
Licensed Content Title	Anion charge storage through oxygen intercalation in LaMnO3 perovskite pseudocapacitor electrodes
Licensed Content Author	J. Tyler Mefford, William G. Hardin, Sheng Dai, Keith P. Johnston, Keith J. Stevenson
Licensed Content Date	Jun 1, 2014
Licensed Content Volume	13
Licensed Content Issue	7
Type of Use	reuse in a dissertation / thesis
Requestor type	academic/educational
Format	print and electronic
Portion	figures/tables/illustrations
Number of figures/tables/illustrations	1
High-res required	no
Figures	FIGURE 5
Author of this NPG article	no
Your reference number	
Title of your thesis / dissertation	The development of the novel electrode materials for supercapacitors and lithium based batteries
Expected completion date	Jan 2018
Estimated size (number of pages)	200
Requestor Location	Mr. YU LIU Room 3113 B500 Curtin University, Bently Perth, WA 6102 Australia Attn: Mr. YU LIU
Billing Type	Invoice
Billing address	Mr. YU LIU Room 3113 B500 Curtin University, Bently

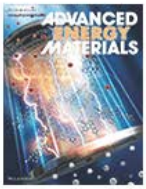

Title: Highly Defective Layered Double Perovskite Oxide for Efficient Energy Storage via Reversible Pseudocapacitive Oxygen-Anion Intercalation

Author: Yu Liu,Zhenbin Wang,Jean-Pierre Marcel Veder,Zhenye Xu,Yijun Zhong,Wei Zhou,Moses O. Tade,Shaobin Wang,Zongping Shao

Publication: Advanced Energy Materials

Publisher: John Wiley and Sons

Date: Jan 2, 2018

Order Completed

Thank you for your order.

This Agreement between Mr. YU LIU ("You") and John Wiley and Sons ("John Wiley and Sons") consists of your license details and the terms and conditions provided by John Wiley and Sons and Copyright Clearance Center.

Your confirmation email will contain your order number for future reference.

printable details

License Number	4273970082040
License date	Jan 21, 2018
Licensed Content Publisher	John Wiley and Sons
Licensed Content Publication	Advanced Energy Materials
Licensed Content Title	Highly Defective Layered Double Perovskite Oxide for Efficient Energy Storage via Reversible Pseudocapacitive Oxygen-Anion Intercalation
Licensed Content Author	Yu Liu,Zhenbin Wang,Jean-Pierre Marcel Veder,Zhenye Xu,Yijun Zhong,Wei Zhou,Moses O Tade,Shaobin Wang,Zongping Shao
Licensed Content Date	Jan 2, 2018
Licensed Content Pages	1
Type of use	Dissertation/Thesis
Requestor type	Author of this Wiley article
Format	Print and electronic
Portion	Full article
Will you be translating?	No
Title of your thesis / dissertation	The development of the novel electrode materials for supercapacitors and lithium based batteries
Expected completion date	Jan 2018
Expected size (number of pages)	200
Requestor Location	Mr. YU LIU Room 3113 B500 Curtin University, Bently Perth, WA 6102 Australia Attn: Mr. YU LIU
Publisher Tax ID	EU826007151
Total	0.00 AUD

Would you like to purchase the full text of this article? If so, please continue on to the content ordering system located here: Purchase PDF

Title:	Molecular Design of Mesoporous NiCo2O4 and NiCo2S4 with Sub-Micrometer-Polyhedron Architectures for Efficient Pseudocapacitive Energy Storage
Author:	Yu Liu,Zhenbin Wang,Yijun Zhong,Moses Tade,Wei Zhou,Zongping Shao
Publication:	Advanced Functional Materials
Publisher:	John Wiley and Sons
Date:	May 16, 2017

Order Completed

Thank you for your order.

This Agreement between Mr. YU LIU ("You") and John Wiley and Sons ("John Wiley and Sons") consists of your license details and the terms and conditions provided by John Wiley and Sons and Copyright Clearance Center.

Your confirmation email will contain your order number for future reference.

printable details

License Number	4236780953787
License date	Nov 26, 2017
Licensed Content Publisher	John Wiley and Sons
Licensed Content Publication	Advanced Functional Materials
Licensed Content Title	Molecular Design of Mesoporous NiCo2O4 and NiCo2S4 with Sub-Micrometer-Polyhedron Architectures for Efficient Pseudocapacitive Energy Storage
Licensed Content Author	Yu Liu,Zhenbin Wang,Yijun Zhong,Moses Tade,Wei Zhou,Zongping Shao
Licensed Content Date	May 16, 2017
Licensed Content Pages	1
Type of use	Dissertation/Thesis
Requestor type	Author of this Wiley article
Format	Print and electronic
Portion	Full article
Will you be translating?	No
Title of your thesis / dissertation	The development of the novel electrode materials for supercapacitors and lithium based batteries
Expected completion date	Jan 2018
Expected size (number of pages)	200
Requestor Location	Mr. YU LIU Room 3113 B500 Curtin University, Bently Perth, WA 6102 Australia Attn: Mr. YU LIU
Publisher Tax ID	EU826007151
Billing Type	Invoice
Billing address	Mr. YU LIU Room 3113 B500 Curtin University, Bently